FAST HISTORY MATCHING OF TIME-LAPSE SEISMIC AND PRODUCTION DATA FOR HIGH RESOLUTION MODELS

A Dissertation

by

EDUARDO ANTONIO JIMENEZ ARISMENDI

Submitted to the Office of Graduate Studies of
Texas A&M University
in partial fulfillment of the requirements for the degree of

DOCTOR OF PHILOSOPHY

May 2008

Major Subject: Petroleum Engineering

FAST HISTORY MATCHING OF TIME-LAPSE SEISMIC AND PRODUCTION DATA FOR HIGH RESOLUTION MODELS

A Dissertation

by

EDUARDO ANTONIO JIMENEZ ARISMENDI

Submitted to the Office of Graduate Studies of
Texas A&M University
in partial fulfillment of the requirements for the degree of

DOCTOR OF PHILOSOPHY

Approved by:

Chair of Committee,	Akhil Datta-Gupta
Committee Members,	W. John Lee
	Daulat Mamora
	Yalchin Efendiev
Head of Department,	Stephen A. Holditch

May 2008

Major Subject: Petroleum Engineering

ABSTRACT

Fast History Matching of Time-Lapse Seismic and Production Data for High Resolution Models. (May 2008)

Eduardo Antonio Jimenez Arismendi, B.S., Universidad Industrial de Santander, Colombia; M.S., Texas A&M University

Chair of Advisory Committee: Dr. Akhil Datta-Gupta

Integrated reservoir modeling has become an important part of day-to-day decision analysis in oil and gas management practices. A very attractive and promising technology is the use of time-lapse or 4D seismic as an essential component in subsurface modeling. Today, 4D seismic is enabling oil companies to optimize production and increase recovery through monitoring fluid movements throughout the reservoir. 4D seismic advances are also being driven by an increased need by the petroleum engineering community to become more quantitative and accurate in our ability to monitor reservoir processes. Qualitative interpretations of time-lapse anomalies are being replaced by quantitative inversions of 4D seismic data to produce accurate maps of fluid saturations, pore pressure, temperature, among others.

Within all steps involved in this subsurface modeling process, the most demanding one is integrating the geologic model with dynamic field data, including 4D-seismic when available. The validation of the geologic model with observed dynamic data is accomplished through a “history matching” (HM) process typically carried out with well-based measurements. Due to low resolution of production data, the validation process is severely limited in its reservoir areal coverage, compromising the quality of the model and any subsequent predictive exercise. This research will aim to provide a novel history matching approach that can use information from high-resolution seismic data to supplement the areally sparse production data. The proposed approach will utilize streamline-derived sensitivities as means of relating the forward model performance with the prior geologic model. The essential ideas underlying this approach are similar to those used for high-frequency approximations in seismic wave propagation. In both cases, this

leads to solutions that are defined along “streamlines” (fluid flow), or “rays” (seismic wave propagation). Synthetic and field data examples will be used extensively to demonstrate the value and contribution of this work.

Our results show that the problem of non-uniqueness in this complex history matching problem is greatly reduced when constraints in the form of saturation maps from spatially closely sampled seismic data are included. Further on, our methodology can be used to quickly identify discrepancies between static and dynamic modeling. Reducing this gap will ensure robust and reliable models leading to accurate predictions and ultimately an optimum hydrocarbon extraction.

DEDICATION

To my beloved wife and her endless patience.

ACKNOWLEDGMENTS

I feel extremely privileged to have had the opportunity to pursue a Ph.D. at Texas A&M University, I am deeply indebted to Dr. Akhil Datta-Gupta for his invaluable help during these great five years. I would like to thank Dr. John Lee, Dr. Daulat Mamora, Dr. Hans Juvkam-Wold and Dr. Yalchin Efendiev for considering being part of my advisory committee.

I'd like to thank Detlef Hohl and the QRM team in Shell E&P for their encouragement and support during my summer internships at Houston and Rijswijk. I acknowledge their helpful comments and suggestions in shaping this research.

I'd like to acknowledge Mike King with BP America Inc. for his thoughtful and challenging ideas that made great amount of this research possible. I'd also like to acknowledge my friend, Adedayo Oyerinde, for the endless and supportive deliberations since we both started our graduate studies.

Finally, I would like to thank my friends: Jong-Uk, Ahmed, Elkin, Deepak, Rahul, Xianlin, Ichiro, Hao, Sarwesh, Prannay and all my fellow Aggies that made this doctorate an enjoyable journey.

Thank you very much.

TABLE OF CONTENTS

Page

Page

LIST OF FIGURES

FIGURE Page

FIGURE Page

FIGURE Page

FIGURE Page

FIGURE Page

FIGURE Page

FIGURE Page

FIGURE Page

CHAPTER I

INTRODUCTION AND STUDY OBJECTIVES

Geological models derived exclusively from static data often fail to reproduce the production history and reservoir displacement development observed during the life of a commercial hydrocarbon accumulation. Integrating reservoir dynamic responses is a vital step to developing an understanding reliable reservoir performance models. Available information on reservoir description can be broadly grouped into two major types: static and dynamic. Static data are time-invariant measurements of reservoir properties, such as cores, well logs, and 3-D seismic data. Dynamic data are the time dependent measurements of flow responses such as pressure, flow rate, fractional flow and, with the use of 4-D seismic, time-lapse saturation and pressure. The process is referred to as "history matching" and is usually the most tedious and time-consuming aspect of a reservoir simulation study.

Conventionally, history matching is performed via parameter multiplier trial/error procedures. Such trial-and-error procedures involve considerable subjective judgment and personal bias, and very often endanger the realism and reliability of the geologic model. Another downside is that not all available dynamic data are included in calibrating the geologic model(s) leading to loss of forecast performance.

An alternative to traditional manual history match are dynamic data integration methods. Integration of dynamic data generally leads to an inverse problem and requires an iterative procedure to minimize a misfit function. If the misfit function is developed solely from the data observed at the wells, the solutions will be non-unique and potentially unstable. This is aggravated when integrating only production data and excluding time-lapse seismic information. This class of inverse problem is known as 'ill-posed', and must be regularized by constraining the solution to independent prior

---

This dissertation follows the style of *SPE Journal.*

information. One of the main goals of this research will be to reduce the non-uniqueness of well-based measurement integration by including additional constraints available in high-resolution seismic data. The proposed methodology will follow streamline-based inversion techniques as they offer unique advantages in history matching and are suitable for high resolution models.

1.1. Data Integration

In recent years, several techniques have been developed for integrating dynamic data into reservoir models[1-12]. Current best practice in dynamic data integration follows a hierarchical workflow to account for uncertainties at various scales. The starting point is screening a geologic model to identify the impact of large-scale features. This assessment is carried out running flow simulations through a set of different realizations. The realizations represent uncertainties in global parameters including fluid contacts, reservoir structure, and boundary support among others. The screening provides a set of realizations that will undergo a more rigorous history match. This history match will involve adjusting local parameters such as permeability, porosity or facies distribution. This step involves localized changes and is typically the most time-consuming aspect of the workflow.

Traditionally, dynamic data integration attempts to honor observed production data, such as bottomhole pressure, water/oil ratio and gas/oil ratio. The amount of production data is small and spatially sparse compared to the model parameters, leading to poorly constrained estimates. It would clearly be beneficial to make use of some type of “space-dense” information that would improve the resolution of the parameter estimates in zones far away from well locations. Among all usual data, seismic data is the most promising candidate to improve the spatial coverage. In addition, advances in automatic history matching have begun to allow researchers to consider the integration of time-lapse seismic data jointly with production data[13-21]. Nevertheless, results to date are often marred by deficiencies in providing a well-founded and efficient approach to properly integrate production and seismic data.

Recently, streamline-based methods have shown significant potential for integrating dynamic data into reservoir models[22-38]. Streamline-based automatic history matching utilizes streamline-derived sensitivities to update geologic models based on production data. The sensitivities quantify the influence of reservoir properties on the production data. These sensitivities provide the fundamental relationships that allow us to invert the production data, measured at the wells, into modified reservoir properties between the wells. This procedure for the integration of production data can be applied using either finite difference or streamline simulation[33-36]. If we are using streamline simulation, then the streamlines already exist and these are used for the calculation of sensitivities. If we are using finite difference simulation, then the intercell fluxes (or velocities) are extracted from the finite difference calculation, and used to generate the streamlines.

The main objective of this research is to develop an efficient history matching approach that can use information from high-resolution seismic data to supplement the aerially sparse production data. The inversion methodology will rest in partial derivatives extracted from streamline trajectories that will be used to relate the production and seismic responses with the reservoir model parameters.

1.2. Objectives

We'll now outline the stages of this research and the specific objectives associated to each phase.

1.2.1. Rigorous Streamline Tracing

Before attempting any inverse modeling we should ensure that an accurate and stable forward model is available. Since the proposed inversion scheme rests on streamlines, regardless of the structural complexities present in the reservoir, the forward model should generate appropriate trajectories. The forward model can be either a finite-

difference (FD) or streamline simulator (SLS). We'll utilize finite-difference simulation for its versatility and resourcefulness in modeling complex physical processes, and we'll take advantage of the unique reservoir insight obtained when generating streamlines. Specifically streamlines will be constructed based on numerical velocity fields generated by the finite-difference simulator. We'll follow state of the art formulations[38-50] and a new tracing algorithm will be developed to properly trace streamlines in the presence of complex structural features. We'll introduce a new streamline tracing strategy, which provides a consistent representation for streamlines and velocities near faults and non-standard connections. The approach will be based on a local (boundary layer) refinement construction that will be used to honor the fluxes at each face, without impacting the representation of flow within cells. We'll present detailed synthetic and field-scale examples to illustrate the benefits and advantages of the proposed tracing algorithm.

1.2.2. Production Data Integration

Streamline models have unique features that make them particularly well-suited for production data integration into high resolution geologic models. The unique information available in streamline trajectories, the time of flight and the streamline-derived sensitivities, allow for targeted changes in the geologic model to match production history. We'll interface the new tracing algorithm with an inversion scheme to integrate and reconcile geologic models to dynamic data in the form of well water cut measurements. We'll follow an integration approach based on streamline-derived sensitivities and the concept of "generalized travel time" inversion[32-36] to minimize the discrepancies between observed data and simulated responses. We'll present several synthetic and field applications to demonstrate how the method can be utilized to quickly identify the discrepancy between geologic models and field production data. We'll show results where the time and effort needed for detailed history matching is minimized using either finite-difference and streamline models.

1.2.3. Time-lapse Seismic Integration

In the proposed approach, the seismic data are not used directly but in the form of fluid saturation maps derived either by traditional interpretation or by seismic inversion. These maps provide a separate set of constraints in addition to areally sparse production data. An elegant and efficient gradient-based multi-parameter optimization can be performed because the derivatives of both the production data and the fluid saturations with respect to the model parameters are calculated analytically as 1-D integrals along streamlines. The sensitivity computations will require a single flow simulation leading to substantial savings in computing time. The essential ideas underlying this approach are similar to those used for high-frequency approximations in seismic wave propagation[38]. In both cases, this leads to solutions that are defined along streamlines (fluid flow), or rays (seismic wave propagation).

1.2.4. Software Prototype

The primary deliverable of this work will be a software prototype implementing the newly developed tracing and inversion techniques. The developed tool works in an object-oriented architecture where multiple attributes including petrophysical, well-based, and reservoir objects are stored in a dynamic hierarchical platform. The code functionality is expressed by variables and methods implemented within each object, fitting the requirements needed to represent all developed concepts. The application will be ready to interface with commonly used commercial simulators and will lead to significant savings in time and man power. The value of this tool is in close agreement with the industry's necessity of improving asset lifecycle value via fast and integrated reservoir modeling techniques.

CHAPTER II

RIGOROUS STREAMLINE TRACING IN COMPLEX RESERVOIR GEOMETRIES*

Full field flow simulators utilize a variety of cell geometries ranging from simple rectangles to complex corner point systems. One of the benefits of corner-point cells is the ease with which we may represent faulted reservoirs. Each face of a cell may be juxtaposed to two or more cells, depending on the fault throw and the lateral displacements of adjacent cells. Conventional finite-difference approaches routinely include the flux between these cells as "non-neighbor" connections. Other examples of non-neighbor or non-standard connections occur at the boundary of local grid refinement (LGR) or local grid coarsening (LGC) regions where two computational grids come into juxtaposition. In each of these instances, the velocity across the non-standard faces of a cell will be unevenly distributed according to the non-neighbor fluxes. In contrast, the standard streamline velocity interpolation model (Pollock's scheme) used within a cell assumes that the flux be evenly distributed on each cell face, inconsistent with the non-neighbor connection fluxes. Streamlines traced with such an approach do not have sufficient degrees of freedom to be consistent with the finite-difference fluxes, and consequently will not follow a physical flow path.

In this chapter we'll present a strategy that provides a consistent representation for streamlines and velocities near faults and non-neighbor connections. Our approach is based on a simple local (boundary layer) refinement construction that can be used to honor the fluxes at each face, without impacting the representation of flow within the cell

* Part of this chapter is reprinted with permission from "Spatial Error and Convergence in Streamline Simulation" by Jimenez, E., Sabir, K., Datta-Gupta, A., and King, M., 2005. paper SPE 92873 presented at the 2005 SPE Reservoir Simulation Symposium, The Woodlands, TX, 31 January – February 2. Copyright 2005 by the Society of Petroleum Engineers.

or on any other cell face. The local refinement construction is the simplest extension to three dimensions for faulted reservoir cells which provides consistency with the finite-difference flux calculation. Several examples will be presented for a single pair of cells juxtaposed across a fault and at LGR boundaries to illustrate the difficulties in conventional tracing algorithms and the benefits of our approach. This treatment is contrasted with the usual approach and the implications for reservoir scale fluid flow tracing by streamlines is examined.

2.1. Streamline Tracing and Time of Flight Calculation

A key underlying concept in streamline simulation is to isolate the effects of geologic heterogeneity from the details of the physics of fluid transport calculations. Mathematically, this is accomplished by utilizing the streamline time of flight as a spatial coordinate variable[39-43]. The time of flight is simply the travel time of a neutral tracer along the streamlines and can be defined as,

$$\tau(x, y, z) = \int \frac{\phi \, ds}{|\vec{u}|} \tag{2.1}$$

We can rewrite **Eq. 2.1** in a differential form as follows

$$\vec{u} \cdot \nabla \tau = \phi \tag{2.2}$$

After Bear[52], the velocity field for a general three-dimensional medium can be expressed in terms of bi-streamfunctions ψ and χ as follows,

$$\vec{u} = \nabla \psi \times \nabla \chi \tag{2.3}$$

A streamline is defined by the intersection of a constant value for ψ with a constant value for χ. In two-dimensional applications, we use the simplified functional

forms, $\psi = \psi(x, y)$, $\chi = z$, leading to the more familiar expressions $u_x = \partial\psi/\partial y$, $u_y = -\partial\psi/\partial x$, where ψ is recognized to be the streamfunction.

Streamline techniques are based upon a coordinate transformation from the physical space to the time of flight coordinate where all the streamlines can be treated as straight lines of varying lengths. This coordinate transformation is greatly facilitated by the fact that the Jacobian of the coordinate transformation assumes an extraordinarily simple form when using **Eq. 2.2** and **Eq. 2.3**:

$$\left\| \frac{\partial(\tau, \psi, \chi)}{\partial(x, y, z)} \right\| = \nabla\tau \cdot (\nabla\psi \times \nabla\chi) = \nabla\tau \cdot \vec{u} = \phi \tag{2.4}$$

Starting from this expression, we have the following relationship between the physical space and the time of flight coordinates following the flow direction,

$$\phi \, dx \, dy \, dz = d\tau \, d\psi \, d\chi \tag{2.5}$$

It is now easy to see that the coordinate transformation also preserves the pore volume, which is an essential feature to preserve the material balance. Spatial gradients along streamlines become a very simple form in the time of flight coordinates. Using the (τ, ψ, χ coordinates, the gradient operator can be expressed as:

$$\nabla = (\nabla\tau)\frac{\partial}{\partial\tau} + (\nabla\psi)\frac{\partial}{\partial\psi} + (\nabla\chi)\frac{\partial}{\partial\chi} \tag{2.6}$$

Because $\vec{u}$ is orthogonal to both $\nabla\psi$ and $\nabla\chi$,

$$\vec{u} \bullet \nabla = \phi \frac{\partial}{\partial\tau} \tag{2.7}$$

The major advantage of the τ coordinate becomes evident when we consider the conservation equation for the water phase in two-phase incompressible flow, away from sources and sinks,

$$\phi \frac{\partial S_w}{\partial t} + \nabla \bullet (F_w \vec{u}) = 0 \tag{2.8}$$

This expression can be expanded and transformed using the τ coordinate,

$$\frac{\partial S_w}{\partial t} + \frac{\partial F_w}{\partial \tau} = 0 \tag{2.9}$$

After this coordinate transformation, we have decomposed the three dimensional fluid flow into a series of one dimensional (in τ) evolution equation for S_w along streamlines. This equation is just as valid in one, two and three dimensions, and for homogeneous and heterogeneous media. The τ transformation includes all of these effects. All that is required for implementation is the velocity field and the calculation of the line integral in **Eq. 2.1**. It now becomes critical to have a solid and sound technique to compute τ given a particular reservoir geometry. The details involved in its calculation will be discussed in the following sections.

2.1.1. Cartesian Geometries

To compute time of flight, essentially all streamline codes follow a construction due to Pollock[45], in which the transit time from an initial point in space is built up one cell at a time and there is a single velocity per cell face. The basic idea is to utilize a sub-grid block velocity model that follows from the assumption that each component of the velocity varies linearly between the values on the appropriate pair of cell faces, **Eq. 2.10**. This velocity model can be implemented using the numerical solutions for fluid velocities (fluxes) at the block faces.

$$\begin{aligned} u_x &= u_{x1} + c_x\left(x - x_1\right) \\ u_y &= u_{y1} + c_y\left(y - y_1\right) \\ u_z &= u_{z1} + c_z\left(z - z_1\right) \end{aligned} \tag{2.10}$$

The streamline trajectories and time of flight within the gridblock can be computed by a direct integration of the cell velocities, **Eq. 2.11**.

$$\frac{d\tau}{\phi} = \frac{dx}{u_x} = \frac{dy}{u_y} = \frac{dz}{u_z} \tag{2.11}$$

The time of flight can be integrated explicitly, and independently, for each direction. The integral solution in the *x*-direction starting from location x_0 is presented in **Eq. 2.12**.

$$\frac{\Delta\tau_{xi}}{\phi} = \int_{x_0}^{x_i} \frac{dx}{u_{x0} + c_x(x - x_0)} = \frac{1}{c_x}\ln\left(\frac{u_{xi}}{u_{xo}}\right) \tag{2.12}$$

The index *i=1,2* indicates the grid block faces in the *x*- direction. Identical constructions will arise when integrating in the *y*- and *z*-direction. Thus, the actual cell time of flight for the particle will be given by the minimum over allowable edges,

$$\Delta\tau = Min\ Positive\left(\Delta\tau_{x1}, \Delta\tau_{x2}, \Delta\tau_{y1}, \Delta\tau_{y2}, \Delta\tau_{z1}, \Delta\tau_{z2}\right) \tag{2.13}$$

Knowing the particle time of flight, its exit coordinates can now be obtained by simply rearranging **Eq.2.12**.

$$x = x_0 + u_{xo}\left(\frac{e^{c_x \Delta\tau/\phi} - 1}{c_x}\right) \tag{2.14}$$

2.1.2. Corner Point Geometries

Various generalizations of Pollock's approach are available to handle grid-associated complexities; the most basic is the extension of Pollock's velocity interpolation algorithm to corner point cells. We follow a construction due to Cordes and Kinzelbach[46] (CK) in which the corner point cell is transformed back to a unit cube. In this unit cube Pollock's algorithm is applied, although there are some additional complexities introduced by the transformation[48-51]. Let's return to Pollock's algorithm in three dimensions and rephrase the results in a way to ease the transition to corner point cells. We can re-write the equations in dimensionless variables using the fractional distances through all three coordinate directions, **Eq. 2.15**

$$\alpha = x/DX \quad \beta = y/DY \quad \gamma = z/DZ \tag{2.15}$$

We will also convert the directional Darcy velocities into volumetric fluxes using the cross-sectional areas, **Eq. 2.16**. These fluxes each vary linearly across the cell such that a simple linear interpolation can be applied to compute the principal velocity components at points within a cell.

$$\begin{aligned} Q_x &= u_x \cdot DY \cdot DZ \\ Q_y &= u_y \cdot DX \cdot DZ \\ Q_z &= u_z \cdot DX \cdot DY \end{aligned} \tag{2.16}$$

The same set of equations used to apply Pollock's algorithm can be re-written using the rate of change in the particle's velocity components as it moves through the cell, **Eq. 2.17**.

$$\frac{d\tau}{\phi \cdot DX \cdot DY \cdot DZ} = \frac{d\alpha}{Q_x(\alpha)} = \frac{d\beta}{Q_y(\beta)} = \frac{d\gamma}{Q_z(\gamma)} \tag{2.17}$$

Note that these set of equations are identical to **Eq.2.11**. We have simply expressed the equation in terms of dimensionless distances and volumetric fluxes. Cordes and Kinzelbach provided a simple and elegant generalization of **Eq. 2.17** for computing trajectories and the time of flight in corner point cells, based on two assumptions:

- Linearly interpolate volumetric flux, instead of velocity
- Use the Jacobian instead of cell volume to relate flux and velocity

$$\frac{d\tau}{\phi \cdot J(\alpha,\beta,\gamma)} = \frac{d\alpha}{Q_1(\alpha)} = \frac{d\beta}{Q_3(\beta)} = \frac{d\gamma}{Q_3(\gamma)} \tag{2.18}$$

Note that the above equation has the same form as **Eq. 2.17** except that the cell volume has been replaced by the Jacobian. For a corner point cell in three dimensions, we now posit the following velocity model, analogous to the equations for rectangular cells.

$$\begin{aligned} \phi\frac{d\alpha}{d\tau} &= \frac{Q_1(\alpha)}{J(\alpha,\beta,\gamma)} \\ \phi\frac{d\beta}{d\tau} &= \frac{Q_2(\beta)}{J(\alpha,\beta,\gamma)} \\ \phi\frac{d\gamma}{d\tau} &= \frac{Q_3(\gamma)}{J(\alpha,\beta,\gamma)} \end{aligned} \tag{2.19}$$

The volumetric fluxes will be linearly interpolated between the respective face fluxes.

$$\begin{aligned} &Q_j(\alpha_j) = a_j + c_j \cdot \alpha_j \quad j = 1,2,3 \\ &a_j = Q_{j1} \quad c_j = Q_{j2} - Q_{j1} \quad j = 1,2,3 \end{aligned} \tag{2.20}$$

We have used the simplifying notation, $\{Q_j \mid j = 1,2,3\} = \{Q_x, Q_y, Q_z\}$ and $\{\alpha_j \mid j = 1,2,3\} = \{\alpha,\beta,\gamma\}$. In principle, we can now integrate **Eq. 2.18** to compute the time of flight and trajectories. Unfortunately, these trajectories are much more difficult to

integrate than for rectangular cells, as all three parameters are coupled through the Jacobian. The process of integration can be long and cumbersome.

The tracing implemented in this study rests on a simpler development for time of flight computations in corner point cells[50,51]. The CK method is simplified with the introduction of a time-like parameter *T* that increases along the trajectory. This parameter is called the pseudo-time of flight

$$dT = \frac{1}{\phi}\frac{d\tau}{J(\alpha,\beta,\gamma)} = \frac{d\alpha}{Q_1(\alpha)} = \frac{d\beta}{Q_2(\beta)} = \frac{d\gamma}{Q_3(\gamma)} \tag{2.21}$$

Similar to Pollock's algorithm, these sets of equations can be integrated explicitly, and independently, for each direction. Instead of working with velocity, the volumetric flux is used and is replaced by its linear interpolant in each direction. The integral solution in the α-direction is

$$\int_0^{T_E} dT = \int_{\alpha_0}^{\alpha} \frac{d\alpha}{Q_1(\alpha)} = \int_{\alpha_0}^{\alpha} \frac{d\alpha}{a_1 + c_1 \cdot \alpha} = \frac{1}{c_1}\ln\left[\frac{a_1 + \alpha \cdot c_1}{a_1 + \alpha_0 \cdot c_1}\right] \tag{2.22}$$

Identical constructions will arise when integrating in the β- and γ-directions. The actual cell pseudo-time of flight for the particle will be given by the minimum over allowable edges,

$$\Delta T = Min\ Positive\left(\Delta T_{x1}, \Delta T_{x2}, \Delta T_{y1}, \Delta T_{y2}, \Delta T_{z1}, \Delta T_{z2}\right) \tag{2.23}$$

Once the pseudo-time of flight T is known, the exit coordinate of the particle is easily calculated using the general solution of **Eq. 2.22** in all three directions and solving for each unit coordinate.

$$\alpha_e = \alpha_0 + \left(a_1 + \alpha_0 c_1\right)\left(\frac{e^{c_1 T} - 1}{c_1}\right) \tag{2.24}$$

Knowing the unit space coordinates (α, β, γ) in **Eq.2.24**, we use tri-linear interpolation to transform the unit coordinates to the physical space (x, y, z)[53]. The tri-linear interpolant in *x*-direction is defined in **Eq. 2.25**. The same relationship will be used for both *y*- and *z*-direction.

$$\begin{aligned} x = {} & p_{1,x}\alpha + p_{2,x}\beta + p_{3,x}\gamma + p_{4,x}\alpha\beta + \\ & p_{5,x}\beta\gamma + p_{6,x}\alpha\gamma + p_{7,x}\alpha\beta\gamma + p_{8,x} \end{aligned} \tag{2.25}$$

Where,

$$\begin{aligned} & p_{1,x} = x_2 - x_1 \qquad p_{2,x} = x_4 - x_1 \qquad p_{3,x} = x_5 - x_1 \\ & p_{4,x} = x_1 + x_3 - x_2 - x_4 \quad p_{5,x} = x_1 + x_8 - x_4 - x_5 \quad p_{6,x} = x_1 + x_6 - x_2 - x_5 \\ & p_{7,x} = x_2 + x_4 + x_5 + x_7 - x_1 - x_3 - x_6 - x_8 \qquad p_{8,x} = x_1 \end{aligned} \tag{2.26}$$

These set of coordinate points follows the convention presented in **Fig. 2.1**

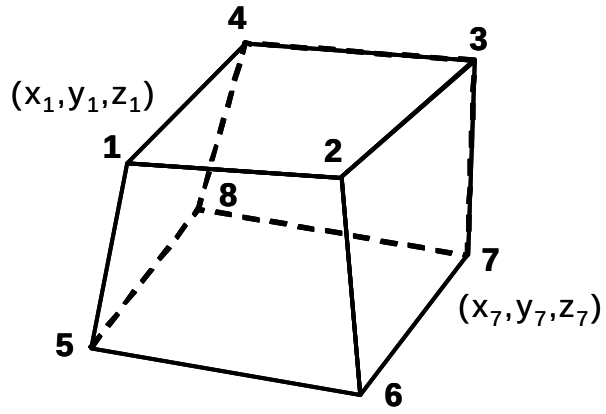

Fig. 2.1 Coordinate convention in a corner point cell.

Streamlines are representations of the velocity and not necessarily particle trajectories. In this instance, *T* is a more convenient parameter for determining these

trajectories, than τ. To within constant scaling factors, the equations for $\alpha(T)$, $\beta(T)$, $\gamma(T)$ are now identical to Pollock's equations[45] in a three dimensional rectangular cell. After obtaining their solution, we can determine τ from the remaining integral:

$$\tau = \phi \int_0^T J(\alpha(T), \beta(T), \gamma(T)) dT \tag{2.27}$$

In the above integral, α, β, and γ are all known functions of T. Each parameter will depend upon T through constructions of the form $\left(e^{cT} - 1\right)/c$, and the Jacobian is a polynomial in α, β, and γ. The resulting integrand is a sum of exponentials and constants, which can be integrated analytically.

The implemented formulation recognizes the importance of taking into account the variation in the Jacobian within the cell to accurately reflect the velocity variations along a trajectory; hence a rigorous tracing is performed within highly non-orthogonal cells. Some commercial streamline simulators use an incorrect scaling by replacing the Jacobian by the constant cell volume in physical space[47,48]. Such approach leads to correct trajectories but incorrect time of flight estimations.

2.2. Trajectory Calculation in Faulted Cells

In both the Pollock's approach, and in its extension by CK, the boundary conditions for the cell are very simple: total flux is specified on each of the six faces, and distributed uniformly across the faces. What about reservoirs with faults, where the flux from one face of a cell may be unevenly divided among a number of adjacent contiguous cells?

Uniform flux and linear velocity are no longer good approximations. What must we do to reasonably trace streamlines when we have non-neighbor flux contributions to a cell? To resolve this question we must look beyond a single cell and instead address the question of flux continuity from cell to cell. This turns out to be a primary requirement

for streamline modeling. Without flux continuity no quantitative streamline model is possible, as the trajectories traced out by the streamlines will then have no relationship to a physical flow path.

2.2.1. Standard Pollock's Interpolation

Consider the simple case of two-faulted cells in an impermeable background, as shown in **Fig. 2.2**. Here, 100% of the flux enters *Cell A* at face *1-2*. It flows to *Cell B* through the non-standard connection of face *4-5*, and exits *Cell B* at face *7-8*. Pollock's model assumes that the velocity is uniformly distributed on all face. This is an excellent representation for face *1-2* and face *7-8*, but it neither correctly characterizes face *4-6* nor face *3-5*. What are the implications of this inconsistency in flux representations? What modeling strategies can we put in place to handle the contradictions?

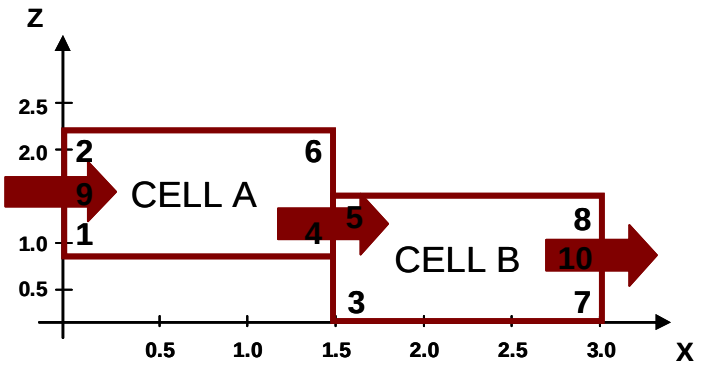

Fig. 2.2– Two-faulted cells sealed at the top and bottom. Flow is from left to right.

Let us utilize the streamfunction to gain additional insight. Between nodes *1* and *2*, the streamfunction varies from 0 to 100% of the flux. Such variation will happen as well between nodes *7* and *8* and between nodes *4* and *5*. Nodes *2*, *5* and *8* lie on one streamline as must nodes *1*, *4* and *7*. Any physical representation of flux, or choice of velocity model in the cells must honor these constraints. **Fig. 2.3(a)** shows one such construction.

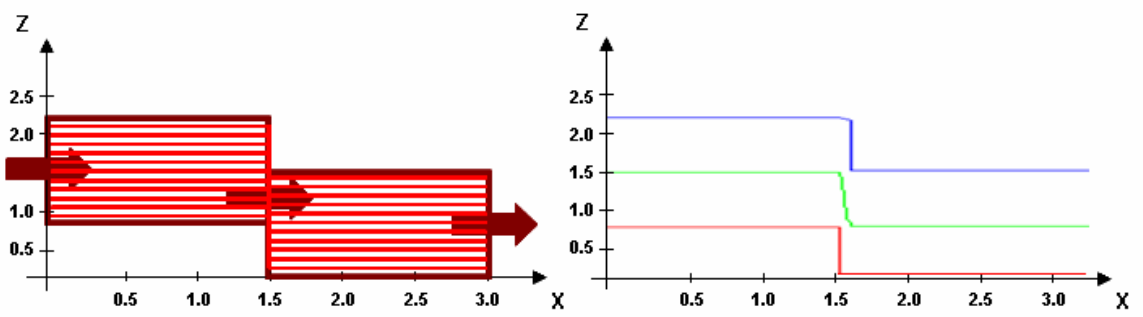

(a) *(b)*

Fig. 2.3– (a) Contours of streamfunction for two-faulted cells sealed at the top and bottom. Flow is from left to right. (b) Three contours selected to demonstrate the streamline slippage at cell faces.

If we calculate the streamfunction within each cell, based on the assumption that the total flux on each face is uniformly distributed on the face, then the contours of the streamfunction will be parallel and evenly spaced. However, as shown in **Fig. 2.3(b),** the continuous contours of the streamfunction must then slip at the cell face to compensate for the incorrect assumption of uniform flux on the cell face. Uniform flux within a cell, plus slip between cells, together provide a physically consistent representation of flow with non-standard connections.

Let us try to trace the streamlines using the usual implementation of the Pollock's algorithm, **Fig. 2.4**. There is no means of representing the discontinuity in flux at the cell faces at the fault. Within Pollock's velocity model, the flux will be distributed uniformly across each cell face and streamlines flow from left to right with no vertical deviation. We are not able to honor the detailed flux continuity between the two cells.

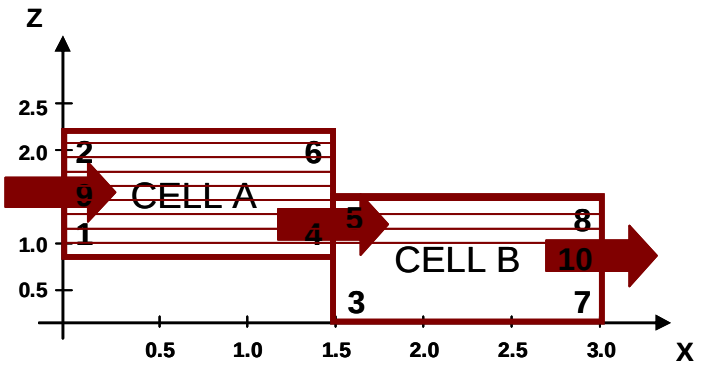

Fig. 2.4– Pollock's algorithm applied to two-faulted cells sealed at the top and bottom. Flow is from left to right.

Consider the time of flight trajectories from the leftmost face of *Cell A*. For lines that originate between nodes *2* and *9*, they will exit *Cell A* between nodes *6* and *5*. They will step to the next cell to the right, which is impermeable, and they will stop. Lines that start between nodes *9* and *1* will trace to exits between nodes *5* and *4*, and will eventually trace to exit points between nodes *8* and *10*, near the top of *Cell B*. Finally, no streamlines trace across *Cell B* from nodes *3* and *4* to nodes *7* and *10*.

Let us repeat the faulted cell construction, this time with three-faulted cells, **Fig. 2.5(a)**. We will again consider the simple picture of flow from left to right, and we will again seal all the vertical faces of this model including the face between *Cell B* and *Cell C*. Contouring of the streamfunction again exhibits vertical slippage at the fault plane, **Fig. 2.5(b)**. The amount of slippage depends upon the magnitude of the fault throw, and on the ratio of the flux between *Cell B* and *Cell C*. Again, if we were tracing a velocity model instead of contouring the streamfunction, we would have incorrectly traced the trajectory beyond the exit from the first cell.

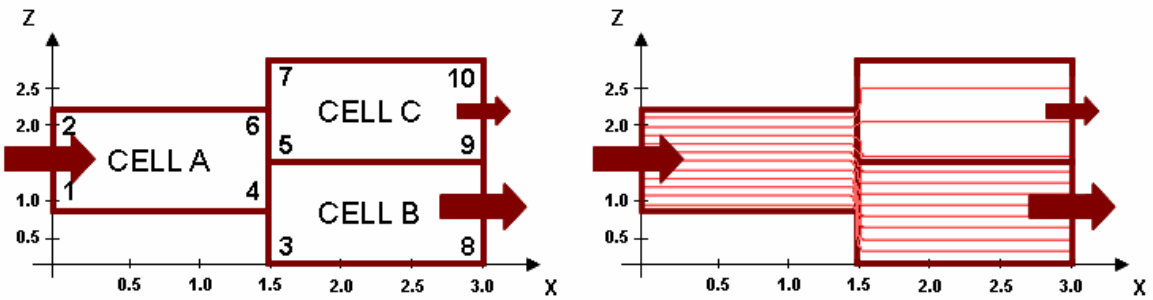

(a) *(b)*

Fig. 2.5– (a) Three- faulted cells sealed at the top and bottom. Flow is from left to right (b) Contours of streamfunction for three faulted cells sealed at the top and bottom. Flow is from left to right.

This use of the streamfunction has provided us with a physical representation of flow between faulted cells, but, as these two examples show, once the fault juxtaposition of flow becomes complicated, then a streamfunction-based slip algorithm is difficult to implement. In addition, it provides no easy generalization to three dimensions.

Fig. 2.6 shows a more complicated faulted system. We'll consider flow from left (injector) to right (producer). Again, there is no means of representing the discontinuity in flux at the cell faces at the fault; the flux will be distributed uniformly across each cell face. Let's review the fault displacement at the bottom layer and consider a conventional and an altered Pollock's treatment used by commercial simulators.

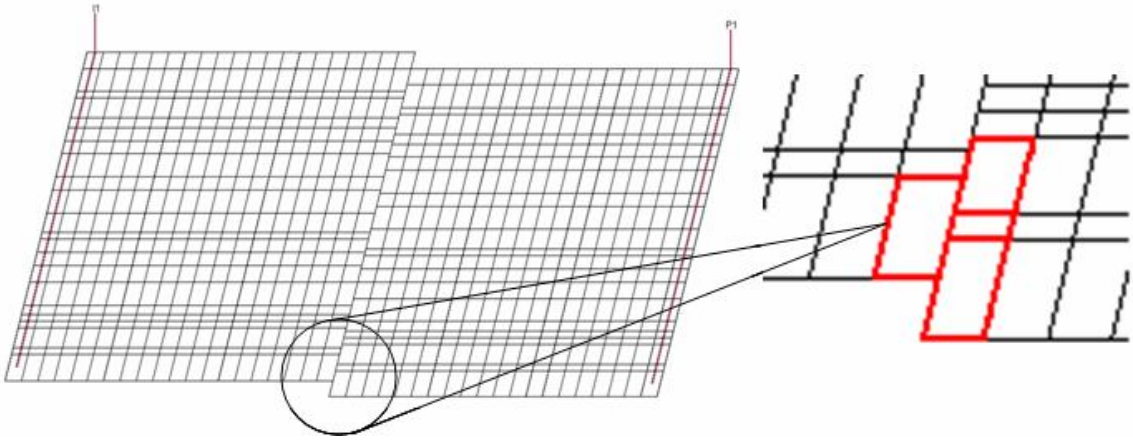

Fig. 2.6– Faulted grid used to illustrate streamline trajectory tracing.

Fig 2.7(a) shows the streamlines generated using the conventional Pollock's algorithm, and as we showed previously the streamlines reaching the face with zero flux are stopping. **Fig. 2.7(b)** shows an altered Pollock's approach in which a slip in the streamlines trajectories is created by translating the streamline coordinates to the connecting gridblock with the largest transmissibility. All of these trajectories are in error. Both algorithms lack a rigorous slip construction at the fault faces and as a result, the trajectories are physically incorrect and the sweep efficiencies and stagnation regions will be incorrectly represented as the streamlines are not following the flux across the non-standard connection.

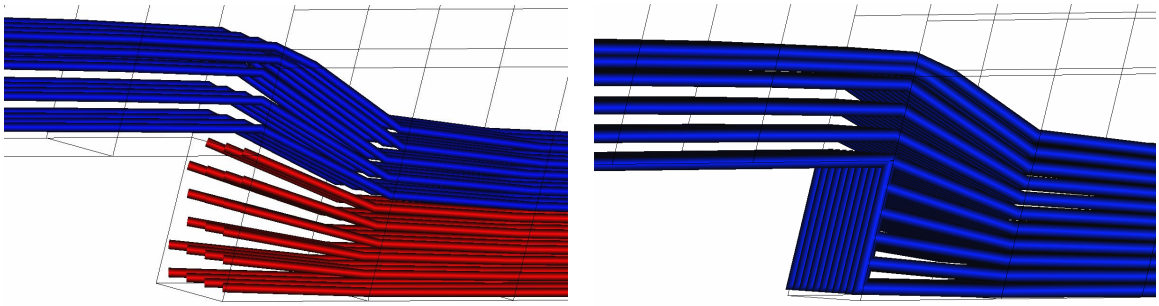

(a) *(b)*

Fig. 2.7– (a) Streamlines generated using conventional Pollock's algorithm (Streamlines stopping at face with zero flux). (b) Streamlines generated using conventional Pollock's algorithm (Streamlines stopping at face with zero flux slips to the next pay cell).

Pollock's velocity model based on uniform distribution of the total flux is failing because it has too little spatial resolution, or equivalently, too few degrees of freedom. Flux is not continuous at cell faces, and streamlines are exiting and entering cells inconsistent with the detailed flux distribution on the cell faces. Large scale, these streamline trajectories do not represent the underlying flow field. This is a leading order error for streamline tracing and for streamline simulation. What are the possible solutions? We can either add more degrees of freedom to the velocity model, or we can refine the original cells until an adequate representation is achieved. We'll follow the later approach in the form of two refinement levels which will be discussed in the following sections.

2.2.2. Global Cell Refinements

A direct solution to the lack of degrees of freedom in the velocity model is by imposing a global cell refinement. It is extremely simple in two-dimensional cross-sections, and provides guidance on the more complex implementation in three dimensions. In addition, it allows us to re-use the Pollock solution, whose properties we already know.

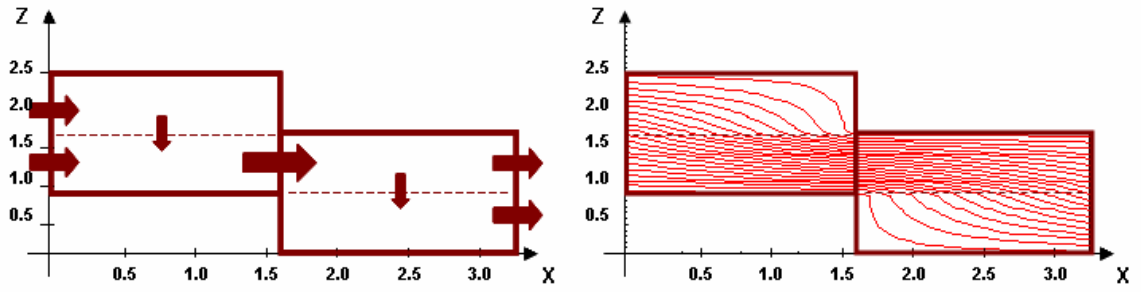

(a) *(b)*

Fig. 2.8– (a) Two-faulted cells global grid refinement. (b) Streamlines for two faulted cells using Pollock's algorithm after global cell refinement.

In **Fig. 2.8(a)** we've split each of the two cells vertically. We can now resolve the flux variations across the fault plane. The split on the opposite face is chosen to provide a rectangular cell. The value of the streamfunction at this point on the opposite face is known since the flux is distributed uniformly on an unfaulted cell face. These higher resolution streamlines honor the fluxes on all faces, and provide an interpolated solution to the flow pattern that is completely consistent with the finite-difference fluxes. The generated streamlines are presented in **Fig. 2.8(b)**. When we work in corner point cells, we refine with fixed α, β or γ intervals. Here, for rectangular cells, we split at a specific value of Z. Depending upon the juxtaposition of adjacent faulted cells, more than one split in Z may be necessary. In three dimensions we may refine in more than one coordinate simultaneously, depending upon the division of the cell face into multiple overlap areas.

How well does this work in more complex cell geometries? In **Figs. 2.9(a)** and **2.9(b)** we show the pattern of refinement used for the three-faulted cell model. Clearly, it can be seen that the generated trajectories looks realistic and consistent with the finite-difference fluxes.

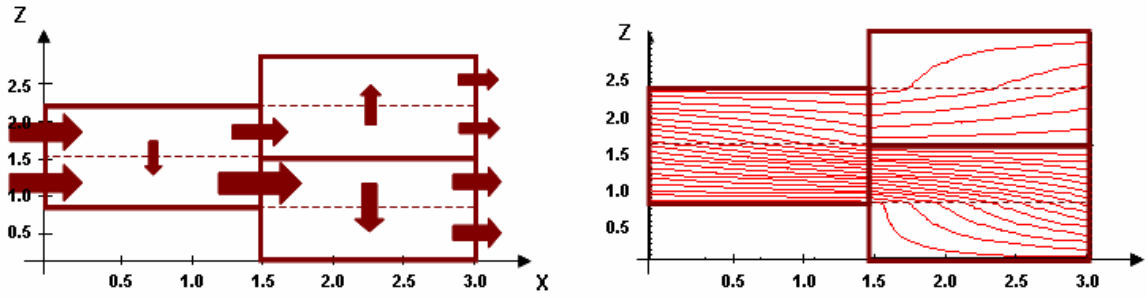

(a) *(b)*

Fig. 2.9 – (a) Three-faulted cells global grid refinement. (b) Streamlines for three-faulted cells using Pollock's algorithm after global cell refinement.

In **Fig. 2.10** we extend the treatment to the global construction for the faulted system presented in **Fig. 2.6**.

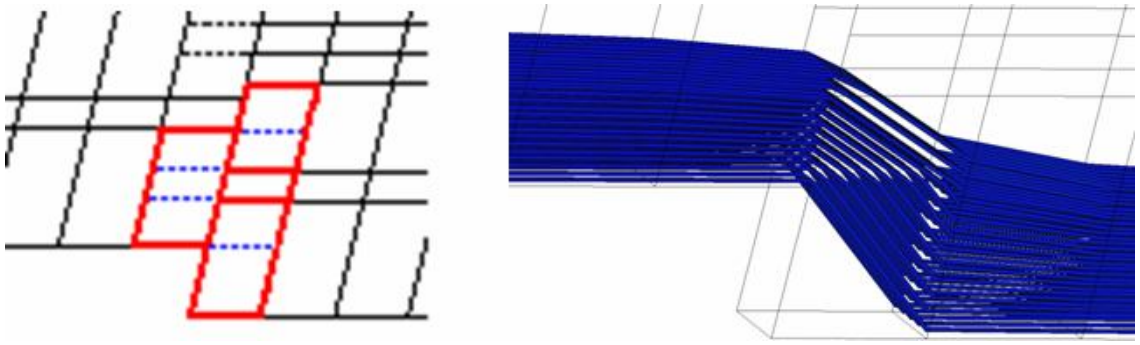

(a) *(b)*

Fig. 2.10– (a) Faulted system global grid refinement. (b) Streamlines for faulted system using Pollock's algorithm after global cell refinement.

In all cases all grid-blocks along the non-neighbor connections must be refined. The flux is still distributed uniformly on the external faces, but it now honors the continuity of internal flux. The resulting model with the refined cells can be used without

difficulty for streamline tracing using Pollock's algorithm. The improved streamline representation can be clearly seen.

So far we have shown the importance of having a consistent representation for flux continuity at cell faces. This requirement is critical to ensure that pathlines trace correctly from cell to cell. It is as important as volume conservation, $\nabla \bullet \vec{u} = 0$, which constrains the shapes of streamlines within cells. This requirement has always been satisfied within the Pollock model because the velocity is uniform on a face. For faulted cells, we no longer have uniform normal velocity. Instead the velocity must vary depending upon the adjacent cells and fluxes.

In principle a global cell refinement approach is simple to apply, even in complex geometries, and allows us to take maximum advantage of the Pollock's solution. Before going further in the discussion, let's review the overall steps of this construction by focusing on a single cell, (*Cell A* **Fig. 2.11**), here expressed in the language of a corner point cell, and generalized to N_f faults. As in these figures, the right-most face of *Cell A* ($\alpha=1$) is faulted, and the flux on the left-most face ($\alpha=0$) is uniform.

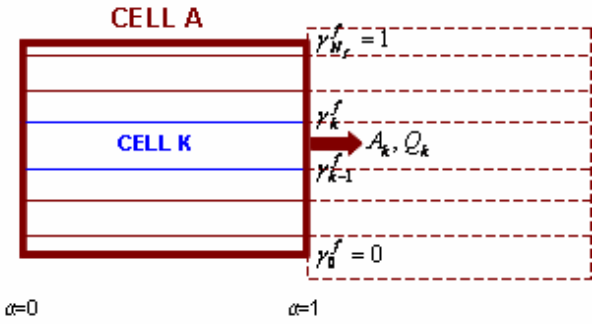

Fig. 2.11– Single cell ('Cell A') faulted cell construction; entire cell is replaced by a global grid.

The overall construction replaces *Cell A* with a vertically refined grid, which is unfaulted, and hence will automatically honor flux continuity across each individual fault connection. In addition, because the grid consists of unfaulted cells, we can utilize the

generalized Pollock construction for corner point cells to trace trajectories across the refined grid.

Generating streamlines for this faulted system will include the following steps:

Step 1: Replace the faulted cell *Cell A* with a refined grid of N_f cells, with corner nodes determined by the overlap with the adjacent cells. For instance, in the (α, γ) coordinates of *Cell A*, a single cell, let's say *Cell k*, would extend the width of *Cell A*, $0 \le \alpha \le 1$, and a vertical interval of $\gamma_{k-1}^f \le \gamma \le \gamma_k^f$.

Step 2: Reconstruct the fluxes across each of these refined cells. Laterally, on the $\alpha=1$ face, the fluxes and the cross-sectional areas are known for each refined cell, as this information is calculated from the simulator's non-neighbor transmissibility construction. These same areas are used to refine the flux, Q_o, that enters *Cell A* at $\alpha=0$. Specifically flux $Q_k = Q_0 \cdot \left(A_k \Big/ \sum_{\ell=1}^{N_f} A_\ell \right)$, enters *Cell k* at $\alpha=0$. The vertical fluxes are recovered simply by subtraction. If the total fluid is compressible, then the sum of the fluxes from a cell does not vanish, but is given by $c\ V_k$, where c is determined from the sum of the fluxes from *Cell A*, and the volume of *Cell A*.

Step 3: Represent the entry point of a trajectory in *Cell A* onto the refined grid. Let's say that we have a trajectory that enters from the left at an initial location ($\alpha_0=0$, γ_0). From the value of γ_0 we know which refined cell we're in, and so we can determine its local coordinate. For instance, if we are in *Cell k*, then we have $(\alpha_0, \gamma_0)_k = \left(\alpha_0, \dfrac{\gamma_0 - \gamma_{k-1}^f}{\gamma_k^f - \gamma_{k-1}^f} \right)$, where $\alpha_0=0$.

Step 4: Trace the trajectory on the refined grid. Working in terms of the refined (α, γ) coordinates and the cell fluxes, there is no need to translate from these (α, γ) to the

physical geometry of the refined cell except within the Jacobian when computing the integral, **Eq. 2.18**.

Step 5: This step is the reverse of ***Step 3***, in which we now translate from the final refined coordinates, let's say in layer ℓ, $(\alpha,\gamma)_\ell$, back to the *Cell A* coordinates: $\alpha = (\alpha)_\ell$, $\gamma = (1-(\gamma)_\ell)\cdot\gamma^f_{\ell-1} + (\gamma)_\ell \cdot \gamma^f_\ell$. The exit point and the computed fluxes within the cells, are consistent with the construction of **Fig. 2.8** and **Fig. 2.9**. In those figures, the refinement occurs in two cells (**Fig. 2.8**) or three cells (**Fig. 2.9**), but each cell can be described as above. In practice, the refined grid of *Cell A* is combined with the refined grid of the cells on the right side of the fault, and the refined trajectory is traced across two columns of the original model in a single calculation.

Of the five steps of this construction, the most difficult to extend to three dimensions is ***Step 1***. If only a single face of *Cell A* is faulted, then ***Step 1*** is not particularly difficult. The coordinate nodes (β_f,γ_f) where *Cell A* intersects with the adjacent cells were determined during the construction of the non-neighbor transmissibilities. Four of these coordinate pairs may be used to trace out a quadrilateral on the $\alpha=1$ face of *Cell A*. The boundaries of the quadrilateral must be chosen to match the overlap areas of the adjacent cells on the face of *Cell A*. The refined grid cells would then be given by these selected ranges in (β,γ), and would extend from $\alpha=0$ to $\alpha=1$. If the $\alpha=0$ face of *Cell A* was also faulted, then the book-keeping becomes more complicated, but we can still build up a set of refined cells from the (β_f,γ_f) coordinate nodes on both faces. However, there is no obvious way to generalize this construction if the $\beta=0$ or the $\beta=1$ face of *Cell A* are also faulted.

2.2.3. Local Boundary Layer

The vertical refinement described in the previous section was a means of introducing extra degrees of freedom into the velocity model. The resulting streamline traces from cell to cell were consistent with the fluxes for each cell pair. Unfortunately,

this specific construction is difficult to implement in three dimensions because of the overlap geometries that arise on each face of a faulted cell, and because of the potential need to extend the refinement across the cell from multiple fault faces. We will describe a simpler local (boundary layer) vertical refinement construction that can be used to honor the fluxes at each face, without impacting the representation of flow within the cell or on any other cell face.

To resolve this geometric conundrum, we will now describe a simpler local refinement, to use just at the faulted face of *Cell A*. Instead of the streamlines of **Fig. 2.8** and **Fig. 2.9**, we will now obtain the streamlines of **Fig. 2.3** and **Fig. 2.5**. Both constructions equally match the non-neighbor fluxes at the faulted cell faces, but now the streamlines will exhibit local slippage instead of being changed globally in *Cell A*. This local geometric construction is pictured in **Fig. 2.12**, in contrast to the global refinement of **Fig. 2.11**. We will review the five steps, and show how they differ in this case.

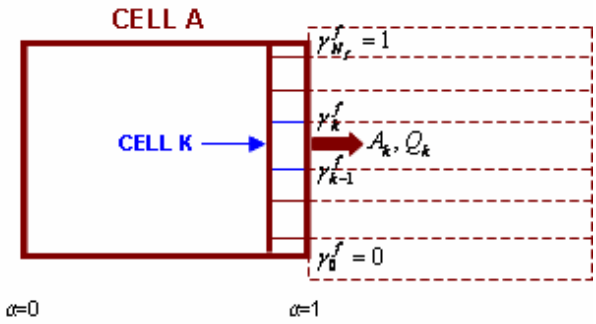

Fig. 2.12– Single cell ('Cell A') faulted cell construction; entire cell is replaced by a local boundary layer.

Step 1 – Grid Refinement: Vertically, the new refinement has not changed. However, laterally, the refined cells only extend a small distance back into *Cell A*. Specifically, at the *Cell A* location $\alpha=1-\varepsilon$, we enter the locally refined *Cell k*, let's say, at location $(\alpha_0)_k=0$. We will work in the limit of $\varepsilon\rightarrow 0$, and so the exit from *Cell A* is at $(\alpha)_A=0$. In this 'boundary layer' limit ($\varepsilon\rightarrow 0$) the construction can be readily extended to three dimensions, with arbitrary degrees of complex faulting, because each face of *Cell A* can be considered separately from any other face.

Step 2 – Flux Reconstruction: There are three differences from the global construction. First, the flux that enters the local region on the left is obtained from the sum of the fluxes over the non-neighbor connections: $Q_k = \left(\sum_{\ell=1}^{N_f} Q_\ell \right) \cdot \left(A_k \Big/ \sum_{\ell=1}^{N_f} A_\ell \right)$. This sum of fluxes is equal to the flux that leaves *Cell A* on its $\alpha=1$ face. The second difference is that the refined transverse flux that leaves *Cell A* must vanish. This is a consequence of the $\varepsilon \to 0$ limit, as this flux is given by the transverse intercell velocity multiplied by the intercell area. In the boundary layer limit, this area vanishes and so does the flux. This result does not hold for the transverse intracell fluxes, which will remain finite in this limit. (Yes, this does imply that the local transverse velocities are infinite, as we will discuss in ***Step 4***.) A third difference, again in this limit, is that the system appears to be incompressible because the sum of the fluxes, let's say from *Cell k*, is $c\ V_k$ where now $V_k\ \varepsilon \to 0$.

Step 3 – Entry Point At Local Grid: Determine the local (α,γ) grid entry. On the local grid, there is no difference from the global construction. However, we exit the *Cell A* global grid at its outlet, $\alpha=1$, instead of its inlet, $\alpha=0$.

Step 4 – Trajectory Tracing: There is no difference in the trajectory tracing. It is performed in the (α,γ) unit space and is not directly impacted by the boundary layer limit. However, the calculation of the transit time is proportional to the Jacobian of the unit cell, which vanishes in the LBL limit. In other words, the transit time across the LBL is zero: there is no need to reference any of the geometric information of the refined cells. A zero transit time is consistent with the infinite transverse velocity mentioned in ***Step 2***.

Step 5 – Global Grid Exit: Determine the global (α,γ) grid exit. There is no difference from the global construction. When combined with the refined local grid from the adjacent cells, the local coordinate $\alpha=1$ will correspond to $\alpha=0$ in one of the cells to the right of the fault.

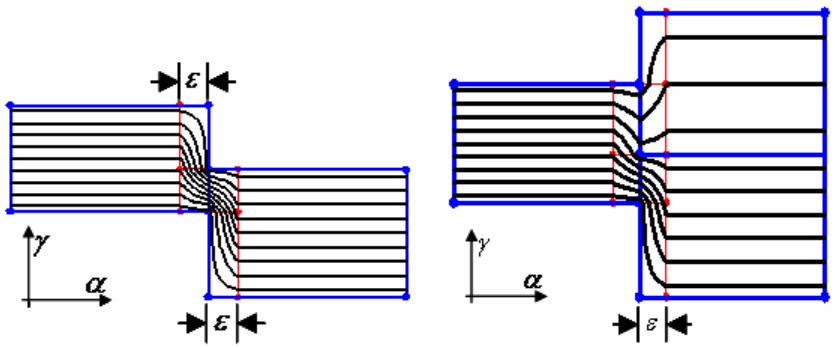

(a) *(b)*

Fig. 2.13– Faulted cells showing uniform flux away from the fault and local vertical refinement at the fault face. (a) Two faulted cells (b) Three faulted cells. $\varepsilon \to 0$ in the construction, but is shown here for a finite value to view the streamlines.

As an example, **Fig. 2.13** shows the locally refined grids corresponding to the two cell and three cell faulted cases of **Fig. 2.8** and **Fig. 2.9**. The reader may recognize that the problem solved on the local grid in **Fig. 2.13** is identical to the global refinement examples of **Fig. 2.8** and **Fig. 2.9**. This is because the latter two examples were chosen to be very simple, with zero transverse flow.

This local procedure is immediately applicable to three dimensional faulted cells. **Fig 2.14(a)** shows the local boundary layer for the faulted system in **Fig. 2.6** with the corresponding streamlines in **Fig. 2.14(b)**, the slip in trajectory is now following the flux across the non-standard connection. In general, the global refinement problem will have cross-flow terms. However, because of the nature of the limit as $\varepsilon \to 0$, the local refinement will always remain simple, with no transverse flow between cells.

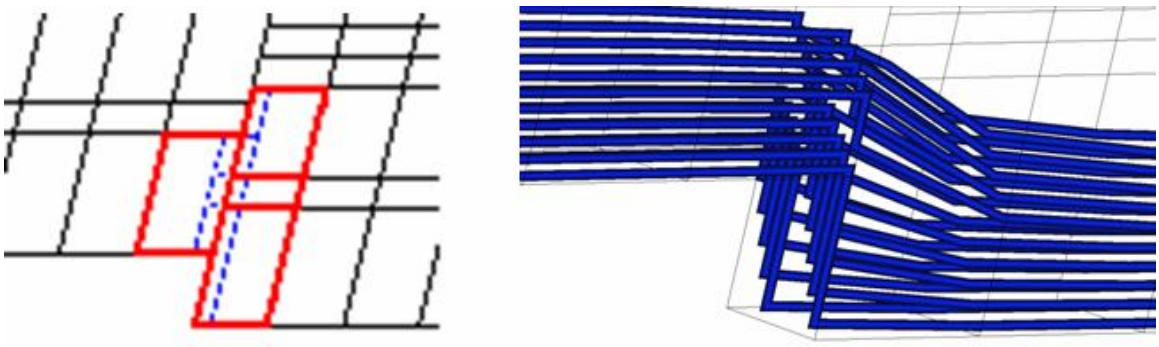

(a) *(b)*

Fig. 2.14– (a) Faulted system local boundary layer. (b) Streamlines for faulted system after LBL refinement.

This is a significantly simpler construction than that of the global refinement. The impact of this approximation on the travel time is shown in **Fig. 2.15**. Here we contrast the time of flight across *Cell A* of **Fig. 2.3** with that from **Fig. 2.8**.

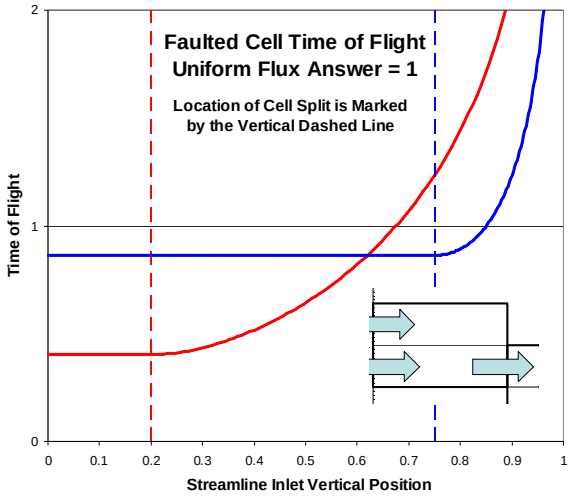

Fig. 2.15– Time of flight to the faulted cell face for a fault with 20% face overlap and with a 75% face overlap. As the overlap area is reduced, the contrast between the fast flow along the bottom of the cell and the slow flow near the top becomes more extreme.

In the boundary layer limit, the streamlines are straight and the transit time is identical for each streamline (normalized to unity). With the deviated streamlines of **Fig. 2.8**, the transit time depends upon the specific streamline. We show two examples: one

with a cell overlap of 20% and another of 75%. Streamlines that are close to the top of *Cell A* flow into the stagnation region and are retarded compared to the average. Similarly, streamlines that are close to the bottom are accelerated towards the fault face. With a pure flow/no-flow contrast this deviation can appear significant. However, when multiple layers all flow, the deviation will be much reduced. In addition, this is an error in calculated transit time that occurs in a single cell along the streamline, and will not contribute persistently.

Let's demonstrate the LBL construction with two additional three dimensional examples. The first, **Fig. 2.16**, is probably the simplest three dimensional fault problem. In this figure, the construction is presented as a montage, starting in the upper left and circling counter-clockwise.

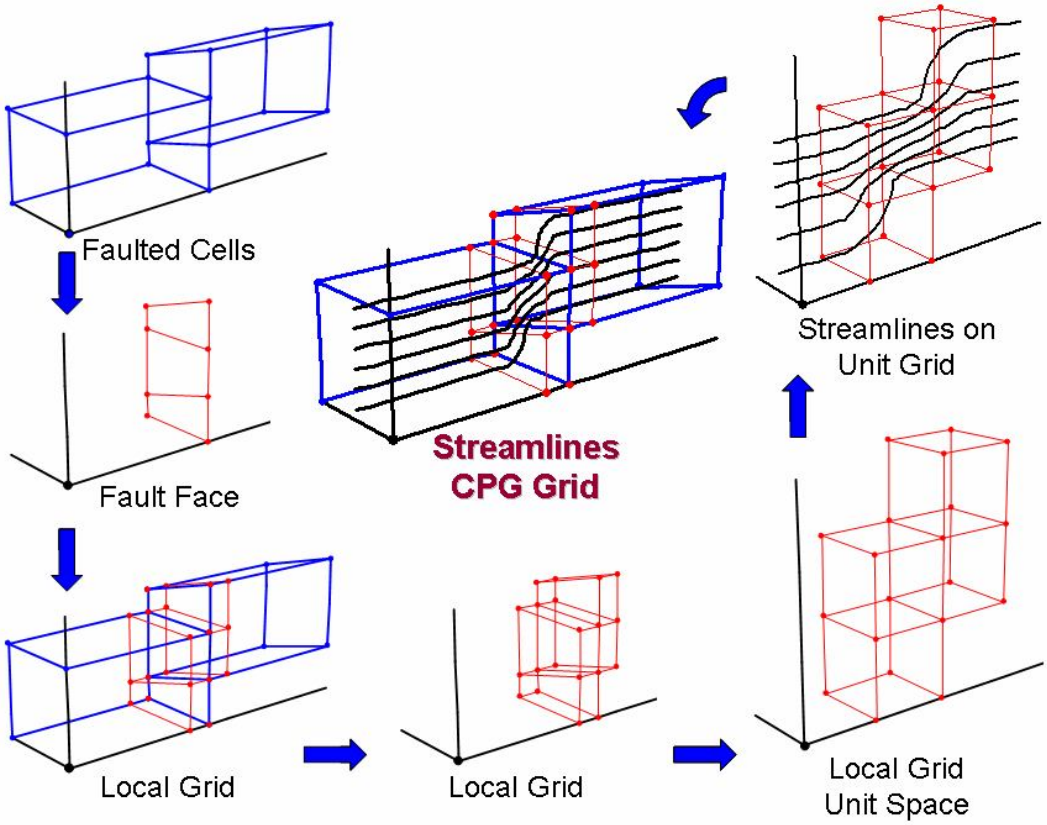

Fig. 2.16– Simple three dimensional calculation of the streamlines on a corner point faulted grid, with the six stages of its construction. Start in the upper right, and proceed counter-clockwise.

The construction in **Fig. 2.16** is as follows. (1) The pair of faulted cells. (2) The projection of the cells into the fault surface. The juxtaposition of the two cells can be described by three local layers, with communication between the faulted cells occurring on local cell at the middle of the LBL. (3) The quadrilaterals in the fault surface are extended forwards and backwards to generate three dimensional local grids in the two original cells. The local grids in the figure are given a finite width only to aide in the visualization. (4) The 2x1x3 local grid, of which two cells are inactive, and not shown. (5) The active cells of the 2x1x3 local grid viewed as unit cubes. Fluxes are reconstructed on this grid. (6) Streamlines traced from the first faulted cell, onto the 2x1x3 local grid, and then into the second faulted cell. (7) The streamlines, transformed back into a real space representation for the pair of faulted cells.

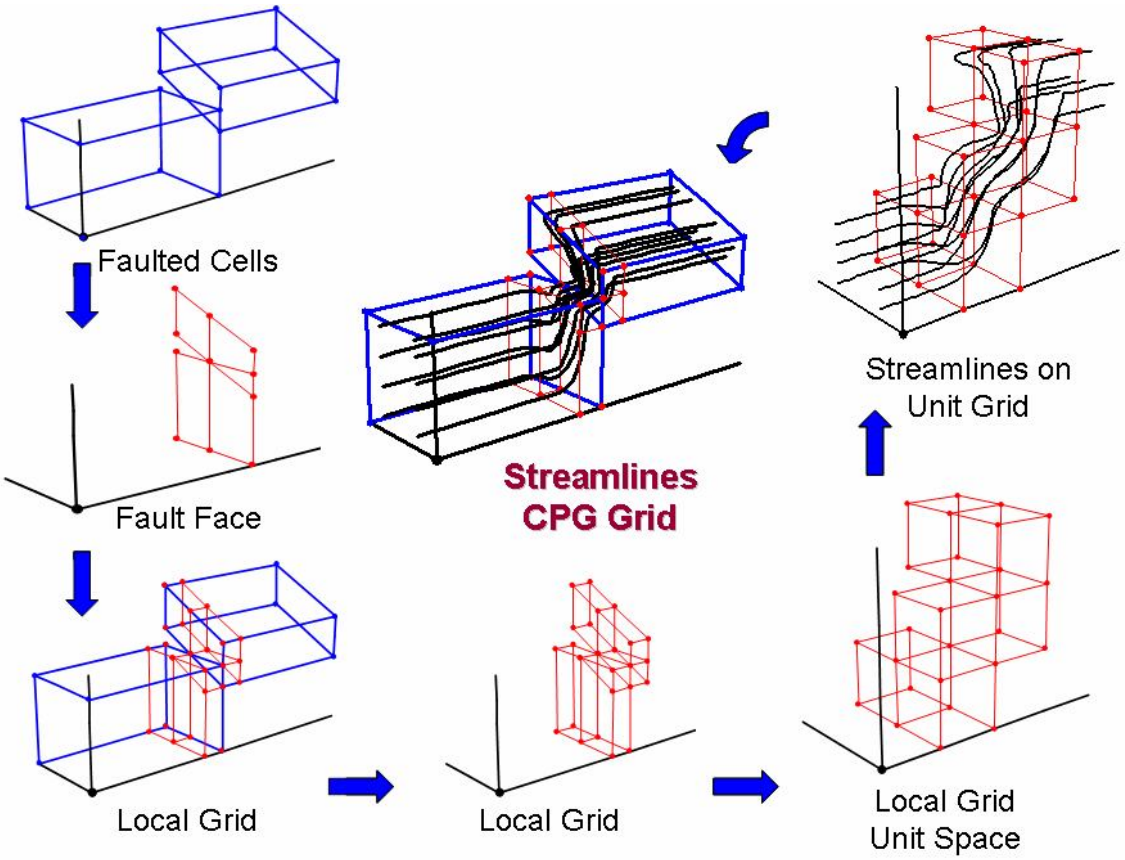

Fig. 2.17– A three dimensional calculation of the streamlines on a more complicated corner point faulted grid, with the six stages of its construction. Start in the upper right, and proceed counter-clockwise.

Fig. 2.17 shows a more complicated fault example. (1) The pair of faulted cells. In this example, the juxtaposition does not occur across the entire width of the cells. Unlike the previous figure, the streamline velocities will now have a transverse component. (2) The projection of the cells into the fault surface would naturally generate one triangle and two pentagons. To obtain quadrilaterals for the local corner point cell construction, an additional coordinate line is utilized. This generates a local 2x2x3 grid, of which 6 cells are active. In general, this local grid will be a 2nynz region, with inactive cells. Notice that the juxtaposition occurs across only a single cell pair. With ny>1 we can describe the necessary transverse flux. (3) The quadrilaterals in the fault surface are extended to generate three dimensional local grids in the two original cells. Again, the local grids are given a finite width only to aide in the visualization. (4) The 2x2x3 local grid. (5) The 2x2x3 local grid viewed as unit cubes. Only the active cells are shown. Fluxes are reconstructed on this grid. (6) Streamlines traced from the first faulted cell, onto the 2x2x3 local grid, and then into the second faulted cell. (7) The streamlines, transformed back into a real space representation of the pair of faulted cells.

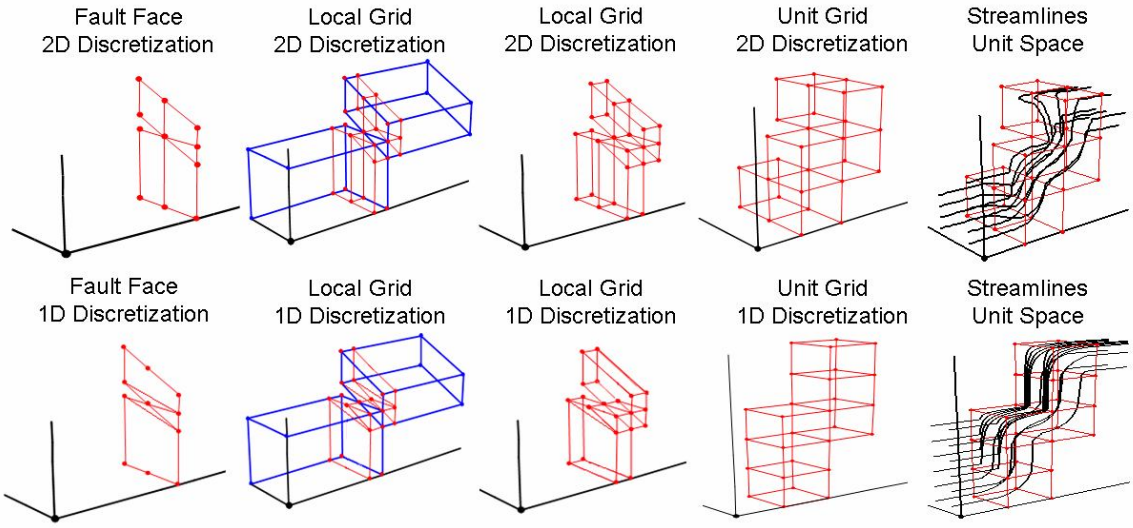

Fig. 2.18– Comparison of a two-dimensional local grid discretization versus a one-dimensional local grid discretization. The one-dimensional discretization greatly simplifies the reconstruction of fluxes avoiding the definition of transverse intracell fluxes.

The previous local boundary construction can be further simplified allowing a simpler implementation for any general case. Such simplification is presented in **Fig. 2.18**. The main difference rests in the fault face discretization, a one-dimensional refinement is used rather than a two-dimensional one. The introduction of the additional coordinate line in **Fig. 2.17** creates an additional unnecessary dimension in the local grid. This additional dimension requires the definition of transverse intracell fluxes in the β-direction which can be avoided by simply changing the fault surface discretization. By avoiding this unnecessary dimension the overall reconstruction of fluxes is greatly simplified, since it'll be reduced to a simple vertical subtraction. This will also benefit the streamline trajectory tracing along the LBL since we'll have a clean one-dimensional unit grid. All the other involved steps remain identical. **Fig. 2.19** shows several discretization examples for faulted faces, note that in all arising configurations it's always possible to build a stack of 1D unit cells via the LBL construction.

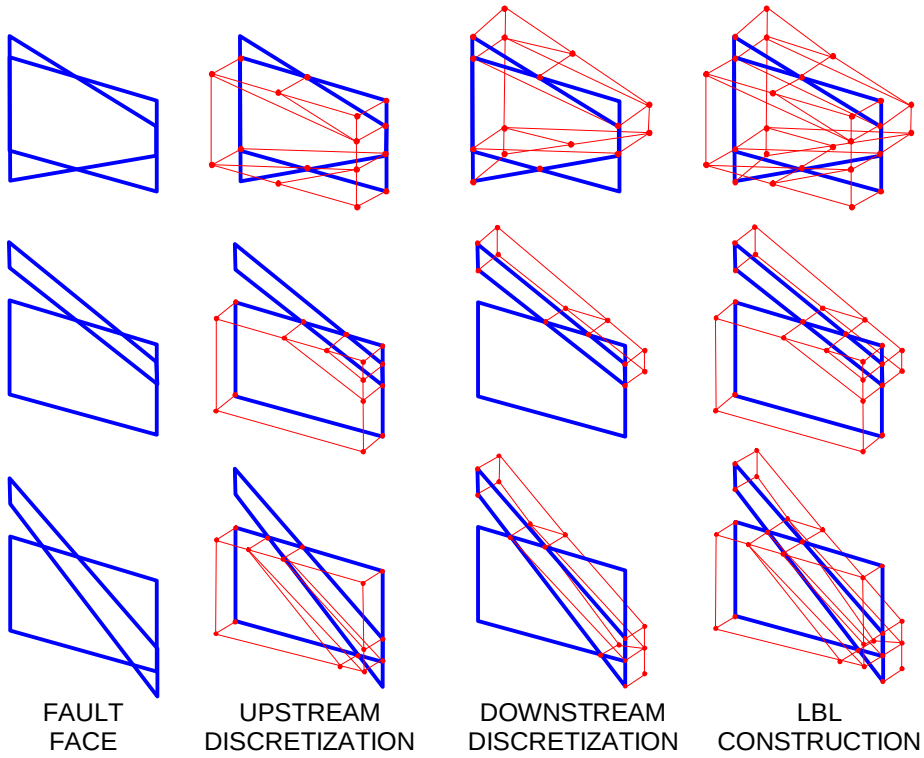

Fig. 2.19– 1D discretization examples for faulted faces. LBL construction can always be defined as a stag of 1D unit cubes.

2.3. Implications in Spatial Discretization

Streamline models rely on a coordinate transformation from the physical space to the streamline time of flight coordinates for saturation calculations. The coordinate transformation can be written in a discrete form as follows:

$$\phi \Delta x \Delta y \Delta z = \Delta \tau \Delta \psi \Delta \chi \tag{2.28}$$

From **Eq. 2.28** we can easily see the analogy between the spatial discretization in finite- difference and streamline simulation. The 3-D discretization elements in these two types of simulation are shown in **Fig. 2.20**. There are two basic elements of spatial discretization in streamline simulation:

1. A *longitudinal discretization* along streamlines in terms of $\Delta \tau$. This longitudinal discretization sets the resolution of the transport calculations along streamlines.
2. A *transverse discretization* in terms of $\Delta\psi\Delta\chi$. that defines the streamtube. In practice, however, we associate a volume $\Delta q=\Delta\psi\Delta\chi$ with the streamline passing through the center of the streamtube. This transverse discretization is primarily determined by the number of streamlines used during the simulation.

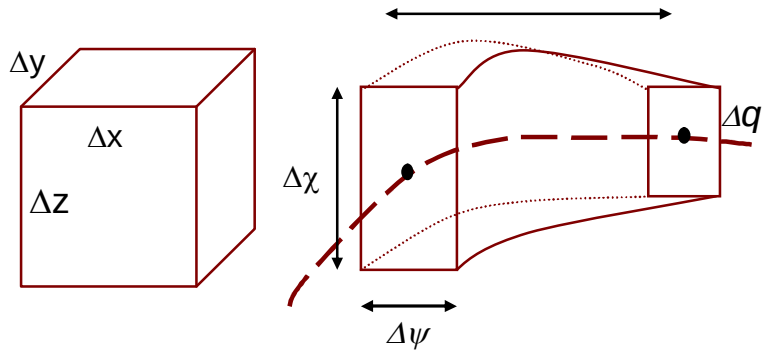

Fig. 2.20 −Discretization elements in finite-differences and streamline simulation.

The analysis of spatial discretization in streamline simulation can be carried out much in the same manner as in finite-difference. However, unlike finite-difference that requires definition of grid dimensions in each of the three coordinate directions, we will

be dealing with primarily two forms of spatial discretization in streamline simulation: a $\Delta\tau$ discretization and a Δq discretization. In light of the previously discussed LBL strategy, we will examine two forms of errors arising from longitudinal discretization: incorrect streamline trajectories and inaccurate time of flight.

2.3.1. Longitudinal Spatial Errors: Streamline Trajectories

So far we have given some evidence in how trajectory errors arise when using a uniform flux distribution in cells with non-neighbor configurations. Streamlines are inconsistent with the detailed flux distribution on the cell faces, therefore the trajectories will fail to represent the underlying flow field. The associated spatial error will have an impact in the time of flight computation and eventually will compromise the displacement calculations.

Let's investigate this with the heterogeneous permeability distribution presented in **Fig. 2.21**. Let's concentrate in highlighted cells *A*, *B*, *C* and *D* which have a contrast in permeability and a significant non-uniform flux distribution along the fault surface. For illustration purposes a finite LBL has been added to aid in the examination of the underlying flow field.

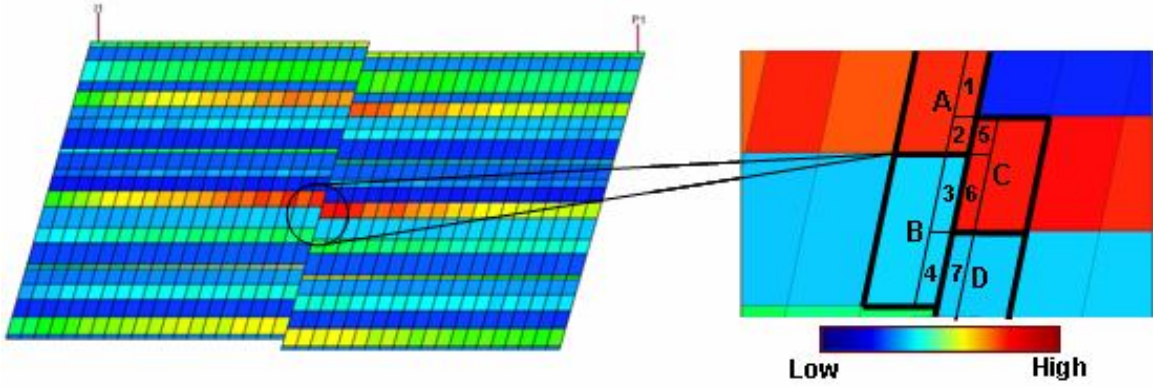

Fig. 2.21– Faulted grid with permeability contrast along non-neighbor connections. A finite LBL construction is provided to examine the underlying flow field.

The flux reconstruction along the LBL is presented in **Fig. 2.22**. The highest horizontal volumetric flux will occur between cells *A* and *C* (along local cells *2-5*), flux

between cells *B* and *C* (along local cells *3-6*) and flux between cells *B* and *D* (along local cells *4-7*) will be substantially smaller. Due to the LBL construction, there will be vertical intracell flux between local cells *1-2*, *3-4* and *5-6*. The nature of the LBL construction doesn't require a vertical flux definition between local cells *2-3* and *6-7*. To preserve consistency with the finite-difference solution, there will be a high vertical intracell flux between local cells *1-2* and *5-6*.

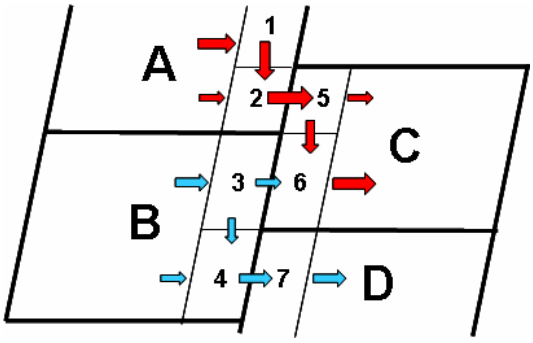

Fig. 2.22– Flux reallocation for LBL construction in faulted grid with permeability contrast.

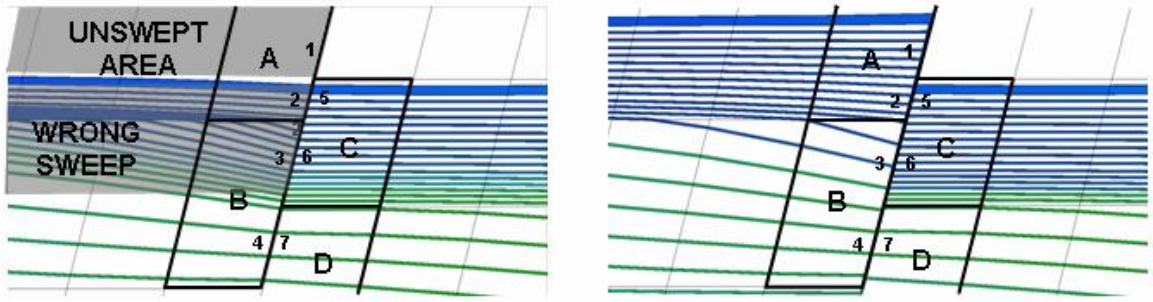

(a) *(b)*

Fig. 2.23– (a) Streamlines generated using conventional Pollock's algorithm (Streamlines fails to represent underlying velocity field). (b) Streamlines generated using local boundary layer (trajectory slippage is due to non-uniform flux at the NNC face).

Fig. 2.23(a) shows the trajectories generated based on Pollock's algorithm and **Fig. 2.23(b)** the streamlines based on the LBL construction. Let's start reviewing the streamlines downstream to the fault surface. Tracing is done from producer to injector (tracing from right to left) and after filtering the streamlines sweeping cells *C* and *D*, it

can be seen they're identical. Note that there's a clustering of streamlines in the upper section of cell *C* product of the streamlines converging to the high permeability layer.

Up to this point, there's nothing new on the trajectories since the tracing hasn't faced any non-uniform flux distribution at the cell faces. However, when the fault surface is reached there's a dramatic change in the streamline trajectories. On Pollock's side there's a noteworthy unswept area in cell *A* which corresponds to the vertical intracell flux between local cells *1* and *2*. The lack of resolution in Pollock's construction is simply not honoring the flux field. On the other hand the LBL construction is clearly conserving the flux resolution with the trajectory slippage that can be appreciated in the clustering of streamlines in the upper section of the local cell *1*. A similar situation occurs at the fault surface between cells *B* and *C*. Again, due to Pollock's lack of flux resolution, there's a mistaken allocation of streamlines between faces *3* and *6* which will generate a wrong sweep through to the subsequent upstream cells. The available resolution in the LBL, i.e. the vertical intracell flux between local cells *5* and *6*, will slip the streamlines preserving the underlying flow field. As we mentioned before, not honoring the flux resolution is a leading error in streamline simulation.

2.3.2. Longitudinal Spatial Errors: Time of Flight

After reviewing the trajectory errors, let's now focus on the impact in time of flight. **Fig. 2.24(a)** and **Fig. 2.24(b)** show contours of time of flight along streamlines generated based on both Pollock's and the LBL construction. Similar to the trajectories, the time of flight contours are identical before reaching the fault surface. After leaving the fault surface, Pollock's contour shows several unswept areas product of the trajectory errors explained before. There's also a perceptible difference in the front location throughout the entire cross-section.

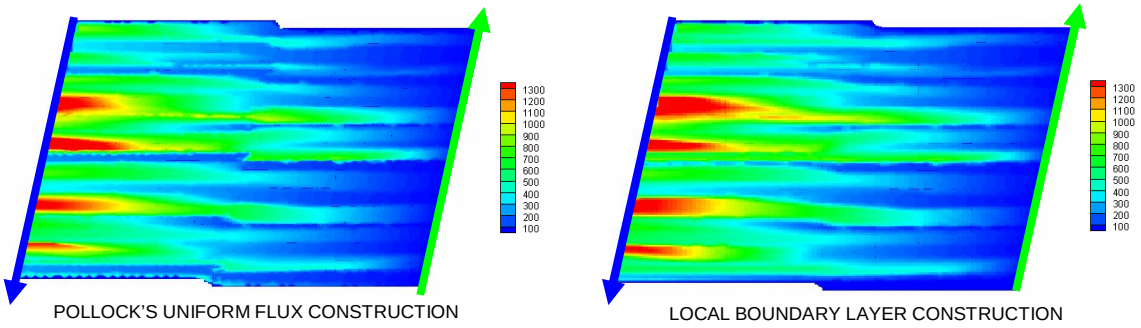

(a) *(b)*

Fig. 2.24– (a) Time of flight contour based on Pollock's algorithm. (b) Time of flight contour based on LBL construction.

This difference can better be appreciated when subtracting both contours as shown in **Fig. 2.25**. The blue contours represent all the unswept areas resulting from the loss of vertical resolution in Pollock's tracing. The red contours represent areas with an overestimated sweep which is a direct product of the streamline misallocation when assuming a uniform velocity field along the fault faces.

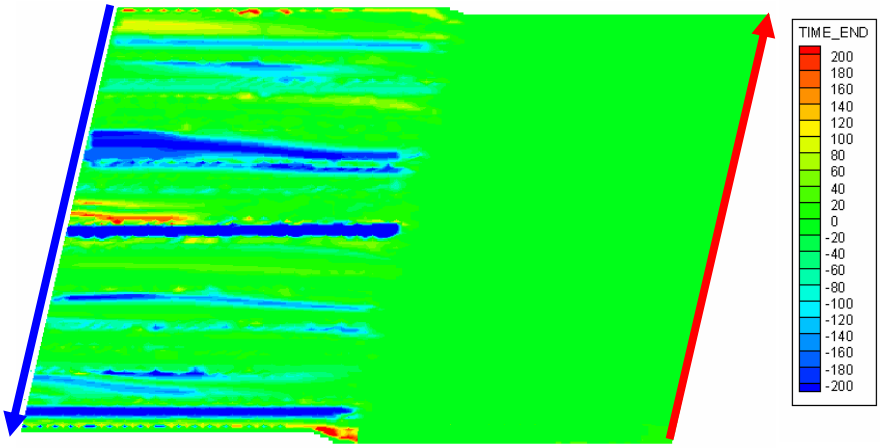

Fig. 2.25– Contour showing difference in time of flight between Pollock's and LBL algorithm.

If we now consider the implications in displacement calculations, our solution will rely on a longitudinal discretization along streamlines in terms of a wrong $\Delta \tau$ that will set an incorrect resolution for the transport calculations along streamlines. A simple

and convenient way to evaluate the discretization error magnitude can be accomplished comparing τ between sinks and sources for both Pollock's and LBL's streamlines. **Fig. 2.26** shows the τ difference (*x-axis*) for all streamlines (*y-axis*). Note that for this simple problem differences greater than 300 days were observed. The implications in large scale problems will be farther serious and will be examined with a field-scaled model.

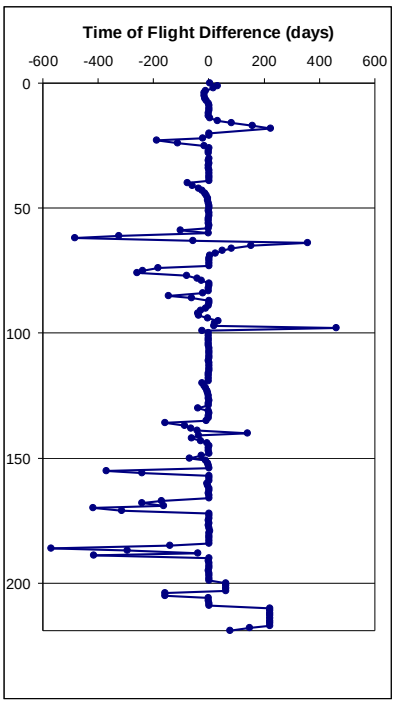

Fig. 2.26– Longitudinal discretization error associated to streamlines based on Pollock's algorithm.

Let's now investigate the magnitude of this longitudinal discretization error in a structurally complex and heavily faulted field-scaled model. **Fig. 2.27** shows the reservoir geometry along with its non-standard connections. There's an injector located at the northern region and a producer located at the southern cells.

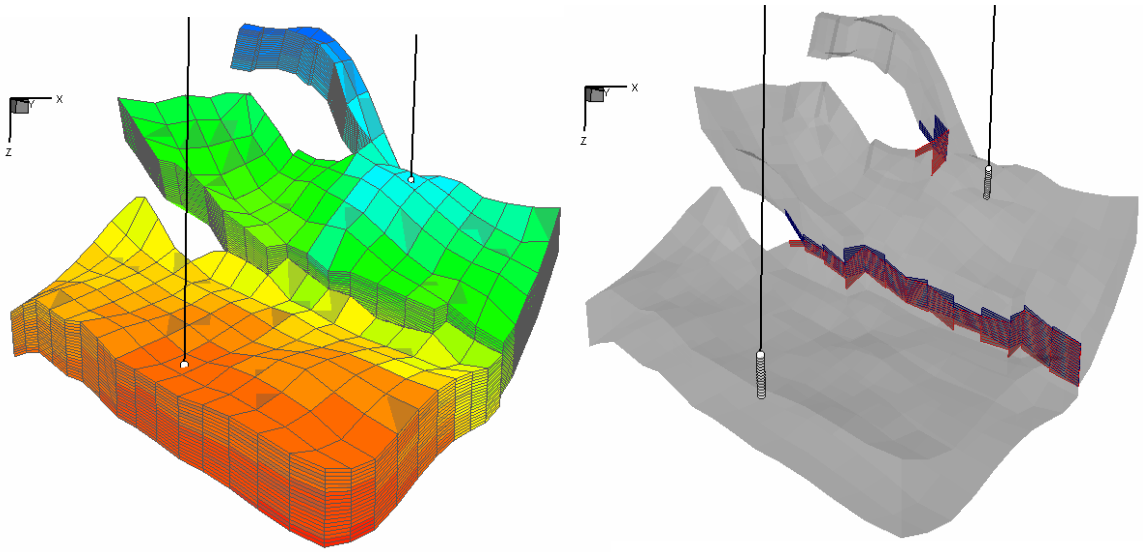

Fig. 2.27– Field-scaled faulted model with several non-standard connections.

A closer look at the non-standard connections is given in **Fig. 2.28**; there're numerous cells showing complex fault juxtaposition and several non-neighbor configurations in different faces. As we previously discussed, a 1-D LBL can be constructed along all these configurations.

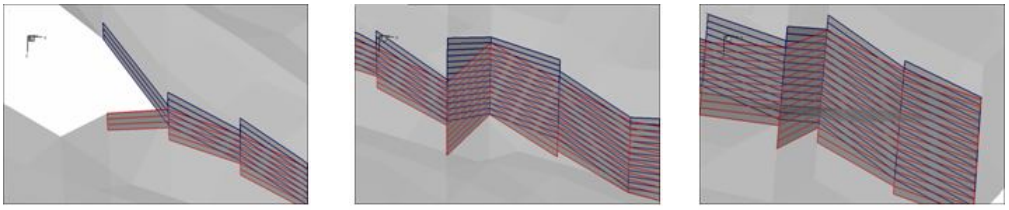

Fig. 2.28– Non-standard connections present in faulted system.

Figs. 2.29(a) shows a few streamlines derived from the LBL construction and the time of flight magnitude along the trajectory. As we did with the previous cross-section model, the LBL trajectories and time of flight were contrasted with Pollock's results. The implications for trajectories at reservoir scale are presented in **Fig. 2.29(b)**.

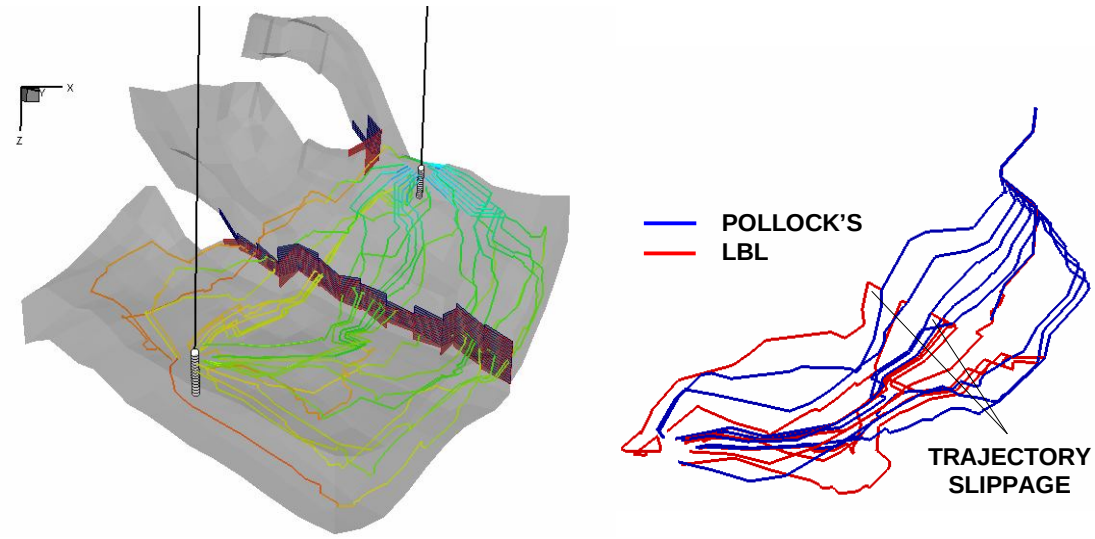

(a) *(b)*

Fig. 2.29– (a) Streamline trajectories using LBL construction (b) Contrast in Pollock's and LBL trajectories.

The blue lines represent the trajectories after Pollock's interpolation and the red lines the streamlines due to the LBL construction. Again, before reaching the non-standard connections all trajectories are identical, since the tracing is based in a uniform velocity field in all cells. As a consequence of the LBL treatment at the fault surface, a significant slippage in streamline trajectories is present. The lack of degrees of freedom in Pollock's treatment, leads to a severely wrong allocation of streamlines.

Let's now examine the impact in time of flight by contrasting both constructions. **Fig. 2.30(a)** shows the *τ-coordinate* for both Pollock and the LBL. A first impression suggests an overall τ delay in Pollock's treatment. On top of the delay, it appears that the total τ is uniform at zones where it should not be. This might be traced back to a wrong representation of the flow field. **Fig. 2.30(b)** shows the difference between the *τ-coordinates*. Differences greater than 5,000 days are observed; as mentioned before this will set an incorrect resolution for the transport calculations along streamlines.

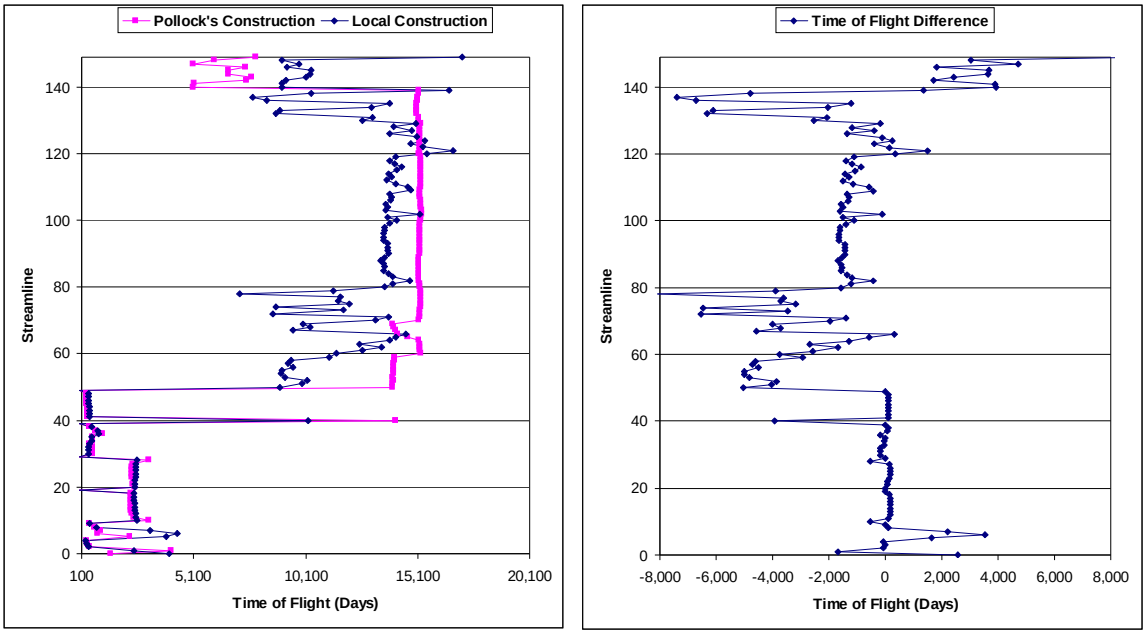

(a) *(b)*

Fig. 2.30– (a) Contrast in Pollock's and LBL time of flight between producer and injector (b) Time of flight difference between LBL and Pollock's construction.

2.4. Field Applications

As stated in the objectives of this research, a key deliverable is the implementation of all derived formulations in a software prototype to be interfaced with commercial and in-house finite-difference simulators. In this section, we'll show the practical utility of our tracing algorithm in several structurally and geologically complex full field models. Our objective here is to take full advantage of both finite-differences (FD) and streamline simulation (SLS). We'll utilize the FD versatility in modeling complex physical processes, and the unique reservoir insight obtained when generating streamlines. Specifically streamlines will be constructed based on the numerical velocity fields obtained when running commercial FD simulators.

2.4.1. Mature Colombian Field

Our first tracing application is in a mature Colombian field with estimated original oil in place of 3700 million barrels. The field was discovered in the late 1910's and over 1700 wells have been drilled in compliance with the primary-recovery waterflooding development plan. Cumulative production in more than 90 years of activity has not exceeded 800 million barrels providing an estimated recovery factor of 20%. The Colombian national company has launched a 12-stage program which ranks high among the world's largest secondary-recovery projects. It's expected to recover at least 200 million bbl of secondary oil. The reservoir has been divided into 12 separate sectors and future work is scheduled to undertake about one new sector each year. The EOR project will double the current field production by means of optimizing the water-injection program. The first stage is a pilot area with over 100 wells with a trustworthy reservoir description in a highly heterogeneous fluvial environment. Production in this pilot area averages almost 7,000 STB/D compared to 2,500 STB/D before flooding. The depositional environment and the convection driven process present in the entire model makes it a perfect candidate for streamline-based reservoir management.

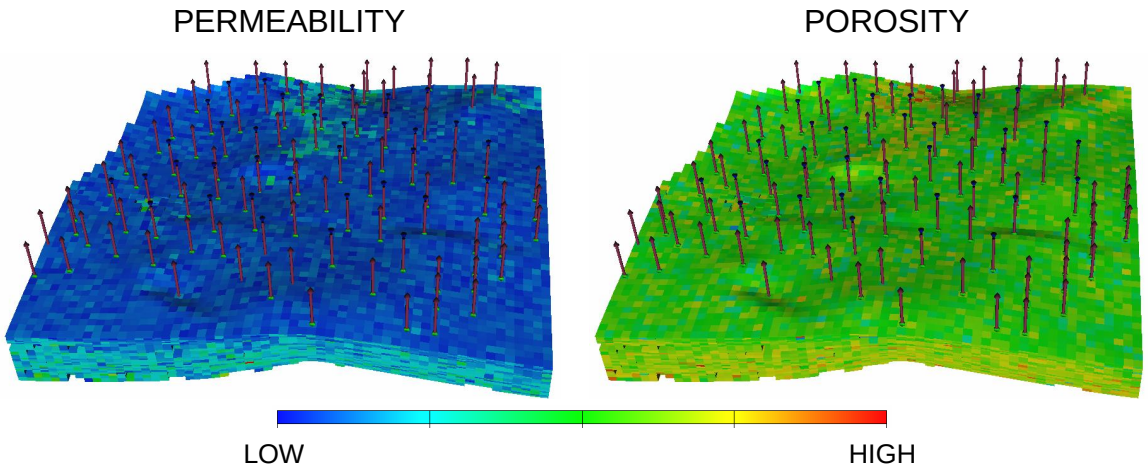

Fig. 2.31– Permeability and porosity distribution for mature Colombian field.

The well location and reservoir properties of this pilot area are presented in **Fig. 2.31**. Reservoir heterogeneity, hence flow performance, is primarily controlled by the

spatial distribution of the depositional facies in the fluvial environment. Thus, the depositional facies were first modeled and then populated with its corresponding specific porosity and permeability distribution.

A commercial finite-difference simulator was used to generate numerical pressure and velocity fields for more than 30 years of history. Two snapshots of the pressure field are presented in **Fig. 2.32**; note the increase in pressure due the injection maintenance program. As we mentioned before, the pressure field is converted to velocity via Darcy's law and is used to generate streamline trajectories and time of flight.

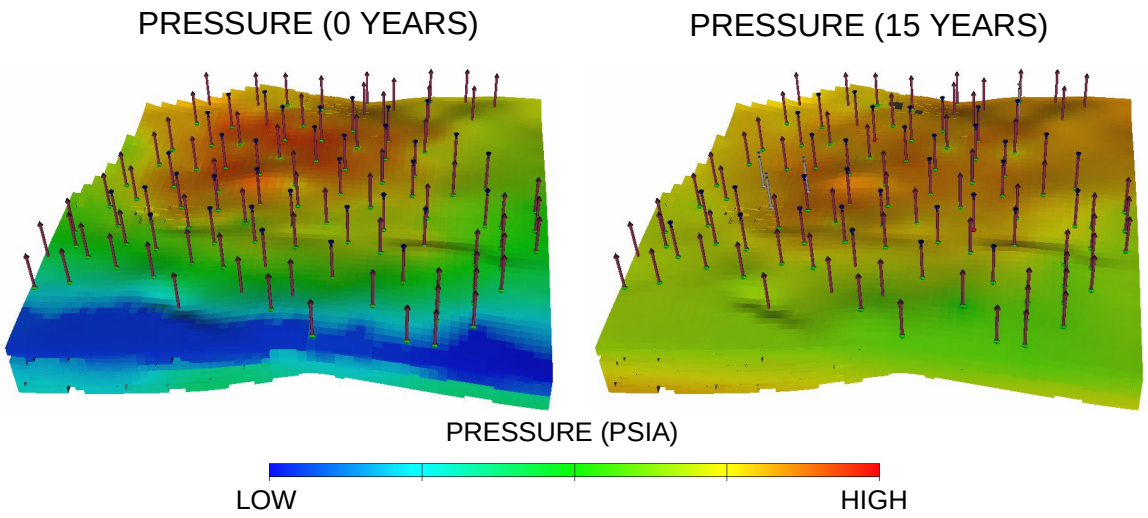

Fig. 2.32– Simulated pressure distribution for mature Colombian field.

Streamlines can aid in reservoir management by providing important information such as injector-producer relationships and allocation factors for wells. This information comes very naturally from streamlines but not from conventional numerical simulators. These allocation factors can be conveniently displayed using pie-charts and can be very useful for pattern balancing and flood front management.

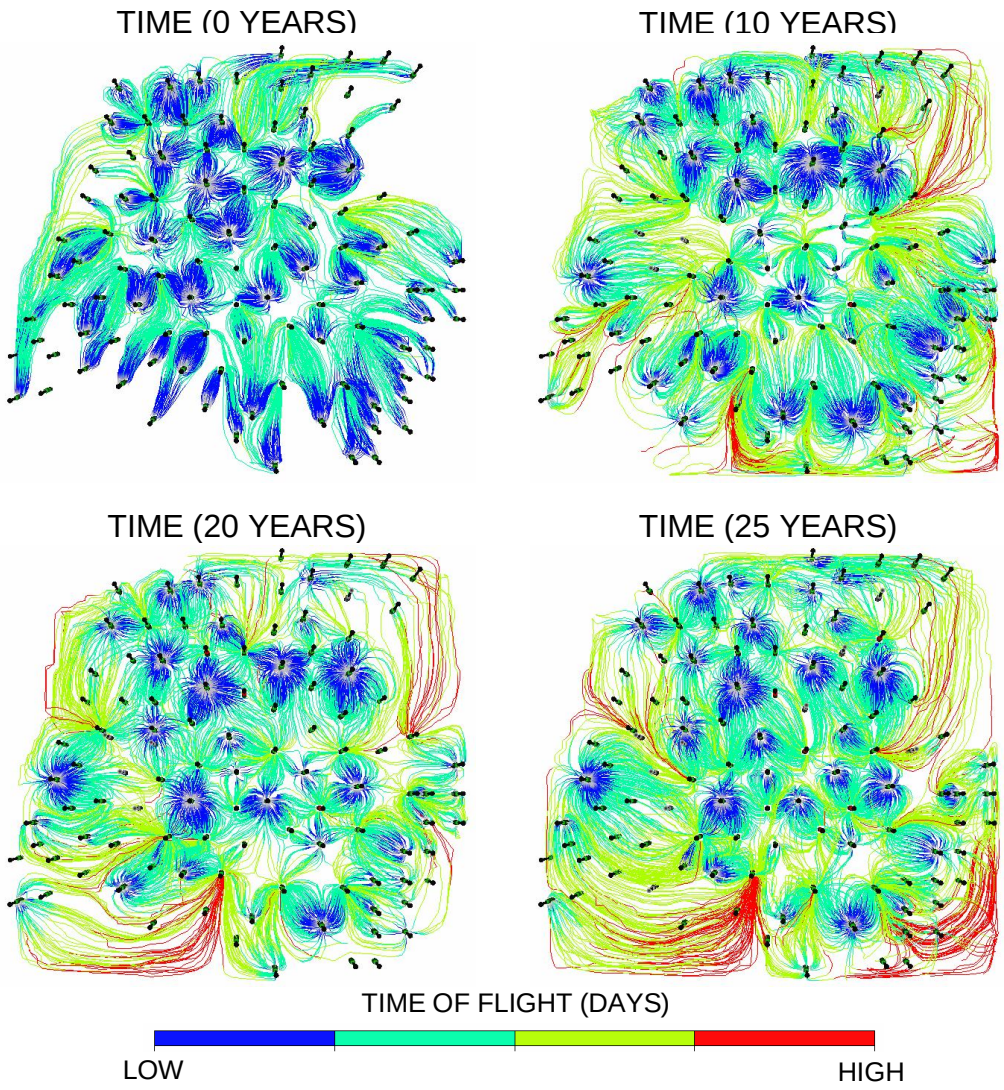

Fig. 2.33– Streamline trajectories and time of flight at different times for mature Colombian field.

Fig. 2.33 shows streamline trajectories and time of flight for several time snapshots. It can be seen how patterns of the streamlines are highly skewed, with injectors supporting producers several patterns over. These highly skewed patterns can be identified when examining the injector-producer allocations factors. Usually, large number of small allocations factors to widely separated well pairs will be found, indicating highly skewed patterns. For the scope of this work, no formal optimization was carried out, instead streamline based flow visualization and allocation calculations were provided to guide the reservoir engineers in the model assessment.

2.4.2. A Russian Field

Our second tracing application is a Russian oil field with over 400 wells and over 20 years of production history. The reservoir produced 9 years under primary depletion before entering the ongoing waterflooding operations. The reservoir model has a detailed rock and fluid description with several saturation and PVT regions. **Fig 2.34** shows the permeability and porosity distribution, which again were derived from a depositional facies modeling followed by population with petrophysical properties.

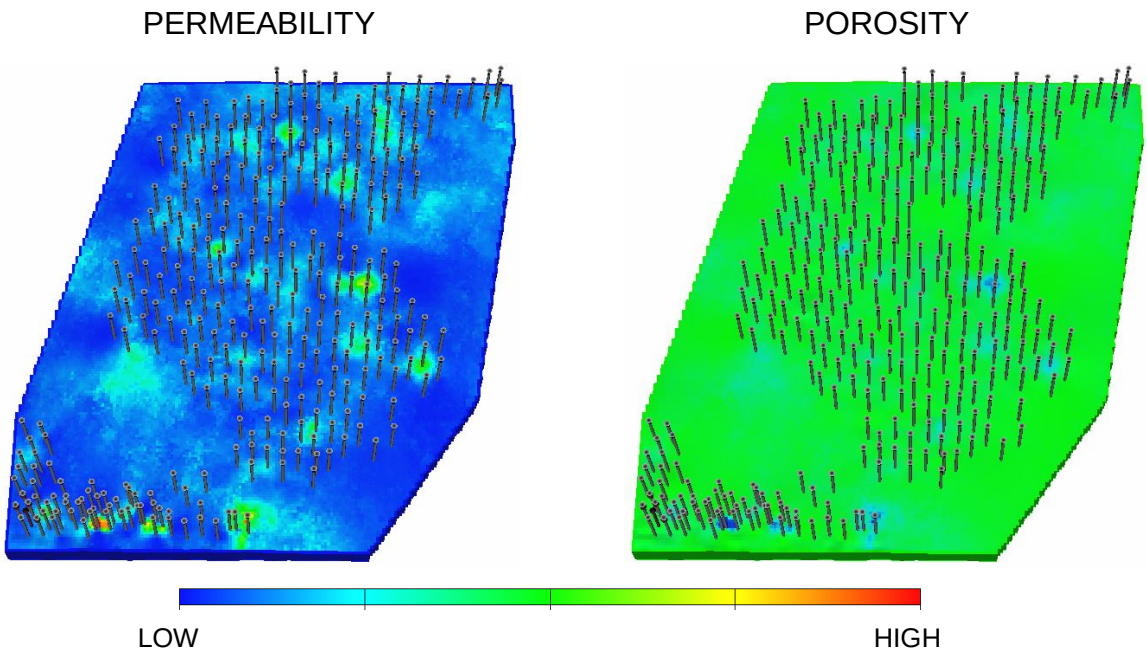

Fig. 2.34– Permeability and porosity distribution for giant Russian field.

Fig. 2.35 shows the well locations (all wells are presented for illustration purposes) and the pressure distribution every 6 years. Note how the field was originally developed only in the southern region and how the pressure drop only advanced to a few cells surrounding the wells. After 6 years the northern region was developed and again the pressured drop was confined to the local vicinity of the wells. Finally an aggressive water injection program started and is currently being evaluated for optimal performance.

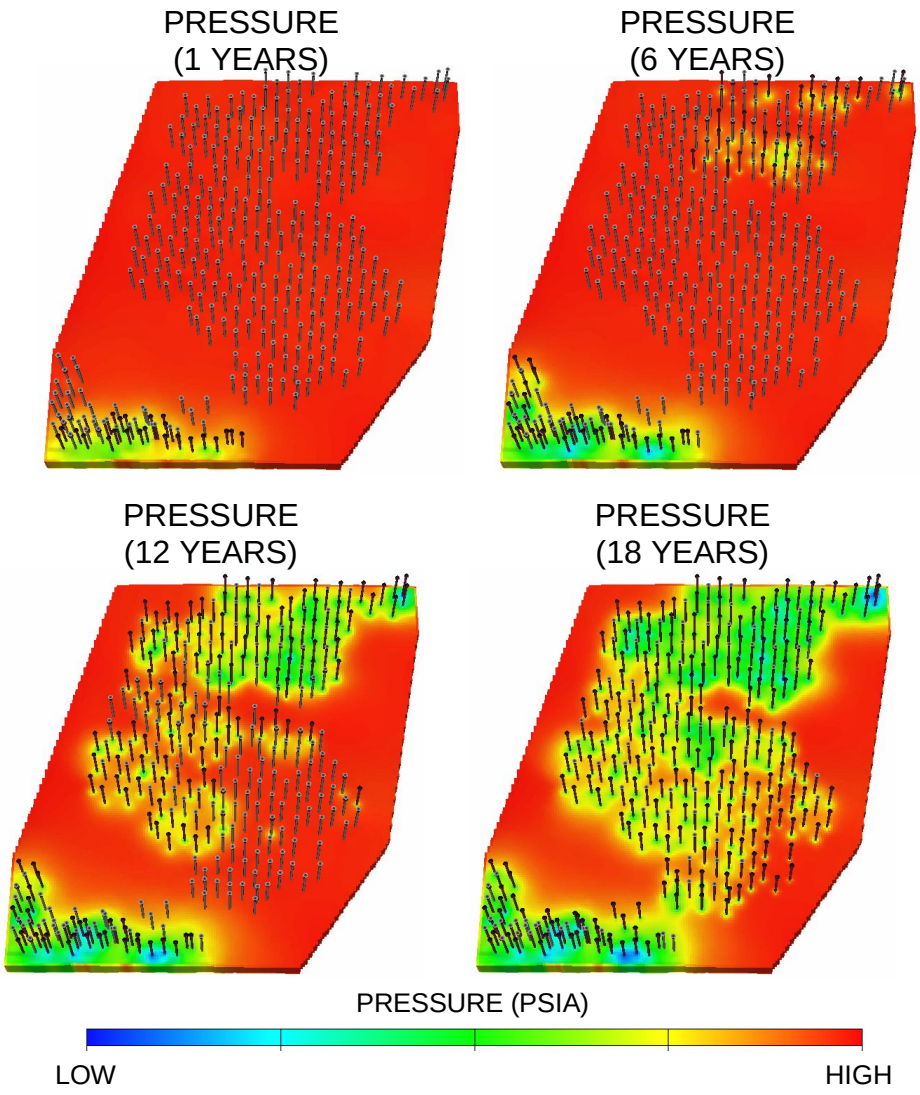

Fig. 2.35– Simulated pressure distribution for giant Russian field.

The streamlines generated with the numerical velocity fields are presented in **Fig. 2.36**. They provide a unique insight in the reservoir mechanisms dominating the fluid flow at the different production development stages. For example, the primary depletion streamlines after 6 year of production can provide unique advantages in computing drainage volume and swept areas. We know that the time of flight reflects the fluid front propagation at various times. For this particular time, the connectivity (volume below a selected threshold) in the streamline time of flight will provide us with a direct measure of volumetric sweep for arbitrary heterogeneity and well configuration.

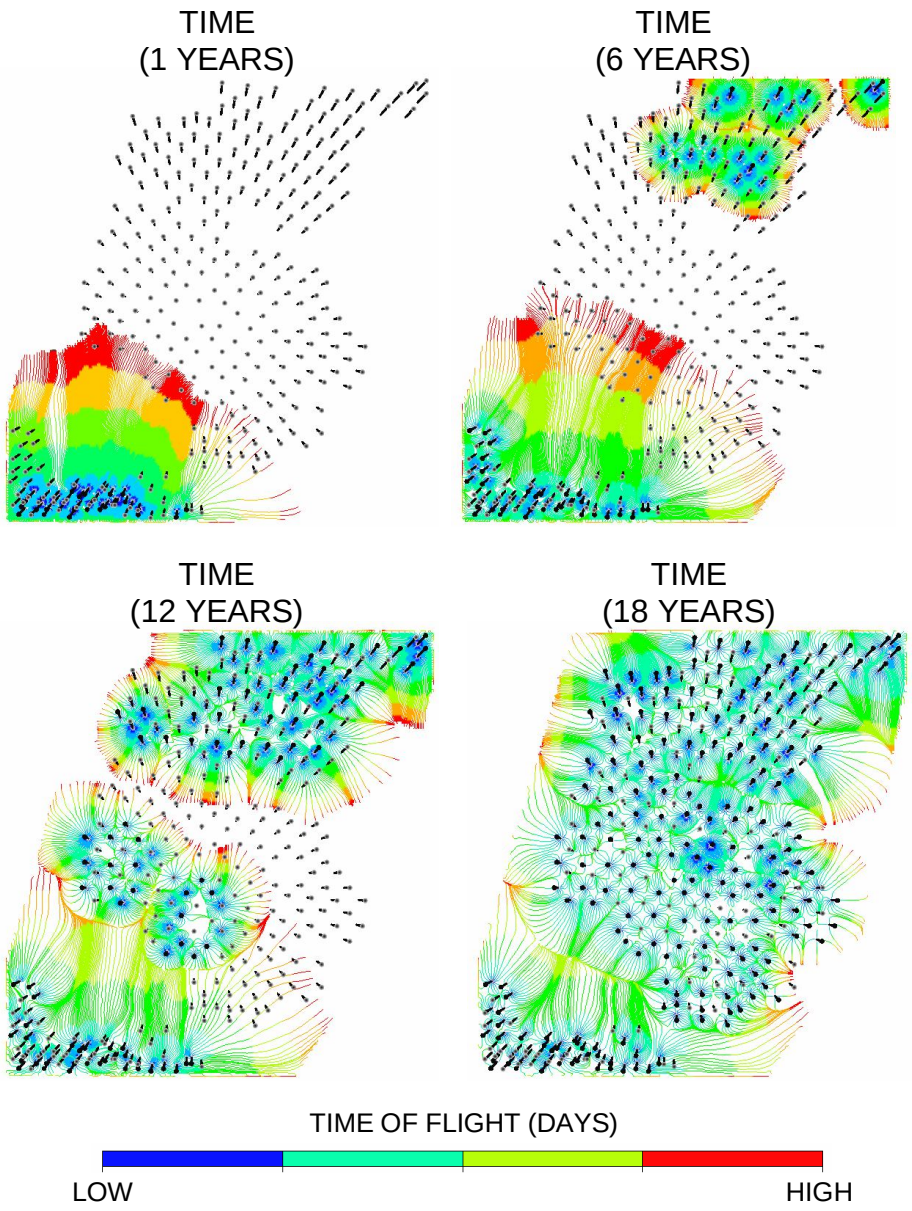

Fig. 2.36– Streamline trajectories and time of flight at different times for giant Russian field.

For the late production stages, the streamlines could be used again to support the operational decisions involved in the overall water flooding program. Maximizing the sweep efficiency is a must and this could be accomplished by balancing pattern breakthrough times. Adjusting the flow-rates to equalize the arrival of waterfront at the producers will maximize waterflood sweep efficiency[47]. Again, we're not providing optimization strategies; our main purpose here is to demonstrate the practical utility of our algorithm under challenging reservoir conditions.

2.4.3. Mature Canadian Field

Our last application is a mature Canadian field discovered in the mid 1950's with an original oil in place of about 1.5 billion barrels. The field produced under primary depletion for almost ten years before entering a 4 year waterflooding development. After production peaked at about 50,000 STB/D, production declined steadily for the next 20 years, dropping to 9,000 STB/D by the late 80's. Additional vertical and horizontal wells were drilled, increasing production to approximately 22,000 STB/D. By the end of the 90's, about 23% of the oil in the reservoir was recovered. Production was again declining rapidly and it was predicted that, unless a new solution could be found to enhance oil recovery, the total recovery would not exceed 25% of the original oil in place. A major secondary CO2 EOR operation was launched in 2000 to enable additional production. The idea is having the CO2 to mix with the oil, causing it to swell and become less viscous. The swelling and miscible displacements force oil out of the pores in the rocks, so that it can flow more easily. Water is pumped into the injection wells, alternating with CO2, to push the released oil toward producer wells, and for better mobility control. The success of the EOR project will be measured not only by the additional production, but also delivering the framework necessary to encourage implementation of CO_2 geological storage.

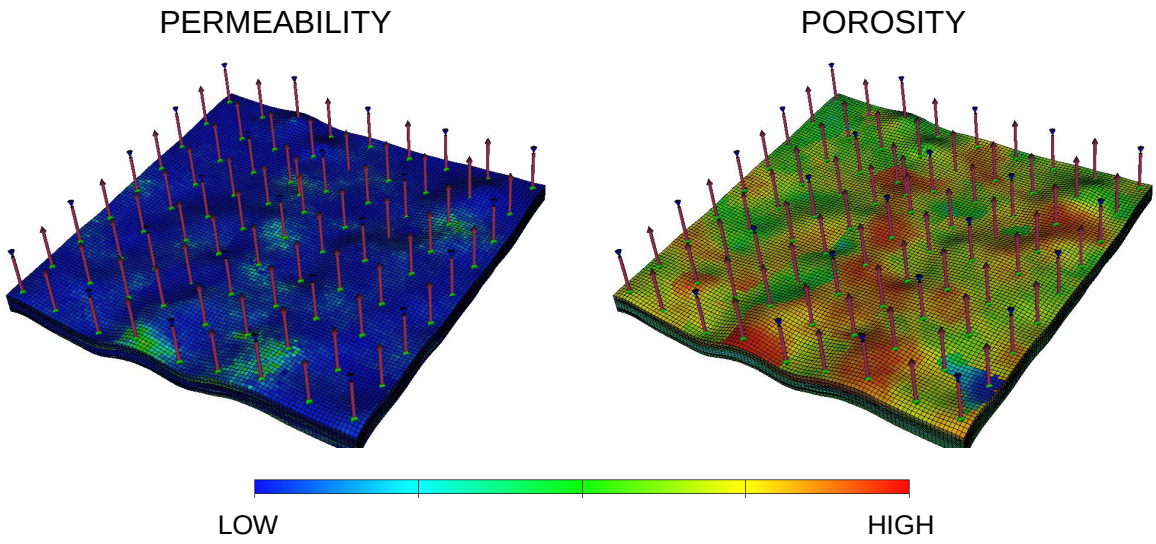

Fig. 2.37– Permeability and porosity distribution for mature Canadian field.

The field has a total of 720 wells drilled in a 9-spot grid pattern. **Fig. 2.37** shows the static model for a pilot area with 66 producing wells and 25 injectors. The model is highly heterogeneous with high permeability zones and high flow capacity rocks. **Fig. 2.38** shows the pressure distribution every 5 years. It can be seen how the area was fully developed after 10 years of infill drilling, followed by the 9-spot waterflooding development.

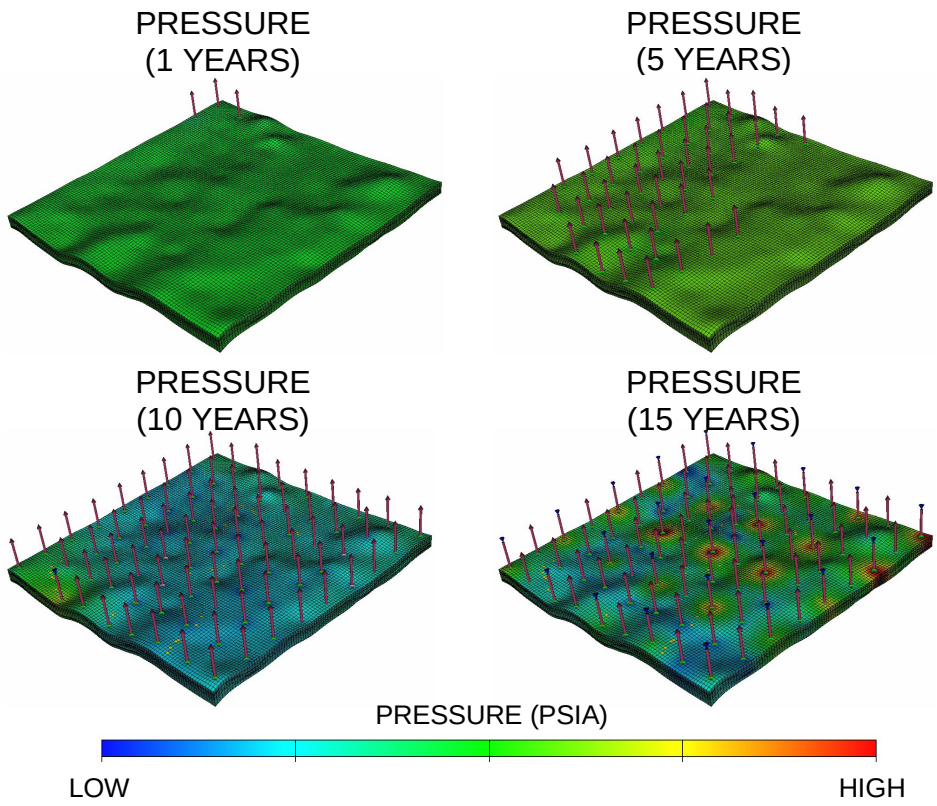

Fig. 2.38– Simulated pressure distribution for mature Canadian field.

The nature of the model makes it another good candidate to apply streamline-based techniques for reservoir management purposes. **Fig. 2.39** shows streamline trajectories for the pressure fields presented in **Fig. 2.38**. Once again streamlines will aid substantially in understanding the reservoir behavior and interactions between producers and injectors. They could also identify by-passed oil zones which would potentially help to optimize the alternate CO2 water injection program. Allocation factors could also

identify injectors contributing poorly to the oil displacement and have better foundations to take any operational decision in terms of where to concentrate the CO2 injection.

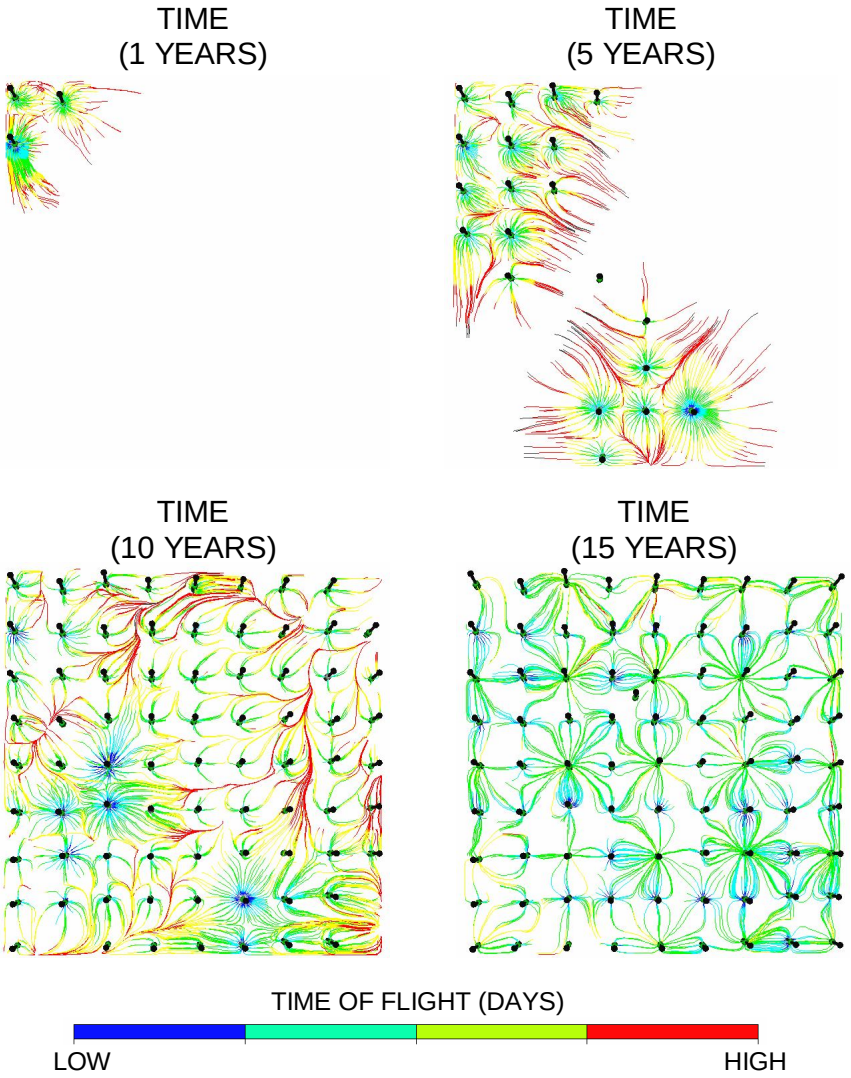

Fig. 2.39– Streamline trajectories and time of flight at different times for mature Canadian field.

CHAPTER III

PRODUCTION DATA INTEGRATION IN HIGH RESOLUTION MODELS USING STREAMLINE AND FINITE-DIFFERENCE SIMULATION*

Fig 3.1 shows a complete static/dynamic data integration workflow used through the lifecycle of a commercial hydrocarbon accumulation. After discovery a static model is generated and constrained by seismic data to obtain a reservoir representation consistent with petrophysical, geophysical and geological data. The seismically constrained model(s) is then up-scaled and prepared for reservoir simulation. Well models and field facilities are also modeled and connected to the reservoir simulator. Multiple development scenarios are combined with subsurface realizations (geologic models) that in turn, are simulated to produce a range of production forecasts and ultimately a business development plan. Since the reservoir simulation model is the main bridge between subsurface and surface engineering, it's imperative to constantly improve its reliability by honoring all relevant dynamic data. This vital process is usually carried out via production data integration, also known as history matching.

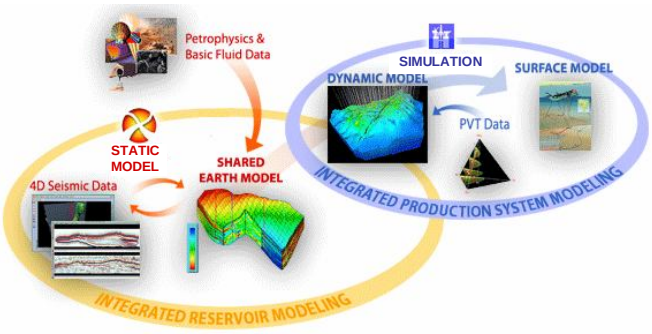

Fig. 3.1– Static/ dynamic integration workflow used through the lifecycle of a hydrocarbon accumulation.

* Part of this chapter is reprinted with permission from "Field Experiences with History Matching an Offshore Turbiditic Reservoir Using Inverse Modeling" by Hohl D., Jimenez, E., and Datta-Gupta, A. 2006. paper SPE 101983 presented at the 2006 SPE Annual Technical Conference and Exhibition, San Antonio, September 24-27. Copyright 2006 by the Society of Petroleum Engineers.

The most demanding and critical step in this workflow is reconciling the geologic model(s) with all available dynamic data. This step is decisive in order to improve the decision quality provided by reservoir simulation. Conventional approaches suffer from several drawbacks which may include: (1) parameter multiplier trial/error procedures that are extremely inefficient and endanger the realism and reliability of the geologic model (2) gradient based methods requiring sensitivity coefficient calculations and minimization which are inefficient and CPU intensive (3) not all available dynamic data (pressures, down hole well rates, 4D Seismic, etc.) are included in calibrating the geologic model(s) leading to loss of forecast performance.

Streamlines techniques offer an attractive combination of properties for production data integration in this workflow. A remarkable advantage is that they provide a prompt discretized flow domain and a unique foundation to calculate efficient sensitivities[30-38]. These sensitivities provide the fundamental relationships that allow us to efficiently invert the production data, measured at the wells, into modified reservoir properties between the wells. The major steps include: (1) flow simulation using either a finite-difference or a streamline simulator (2) well-based production data misfit quantification (3) streamline-based analytic sensitivity computations and, (4) updating of reservoir properties via inverse modeling.

In this chapter, the application of production data integration (water-cut data) via streamlines will be presented for two high resolution field models. We'll start by illustrating the overall procedure with a simple synthetic model and the corresponding formulation behind the approach. We'll then present an application in a giant middle-east field with over a million parameters. We'll show how the inversion results were used to aid in identifying the location and existence of fractures. The chapter will be concluded with an offshore turbitic model featuring a very complex structural model. After achieving a suitable history match, we'll show how the quality of the geologic model was restored after it was altered n a geologically unrealistic manner by parameter multiplier trial/error procedures. In this field application the streamline tracing treatment introduced in the previous chapter was coupled with a finite-difference simulator.

3.1. Background and Illustration

In this section, we'll briefly illustrate the application of streamline simulation techniques to production data integration. We follow an approach supported by streamline-based sensitivity coefficients and the concept of 'generalized travel time' inversion[31-34]. As in any other optimization, there're 4 major steps: (1) a forward model (2) establishing a misfit function between observed and simulated data, (3) defining sensitivity coefficients to relate the simulator performance to the geologic model and (4) the minimization of the objective function which will define a model with a suitable history match. We now briefly outline the mathematical background behind this approach which is summarized in **Fig. 3.2**

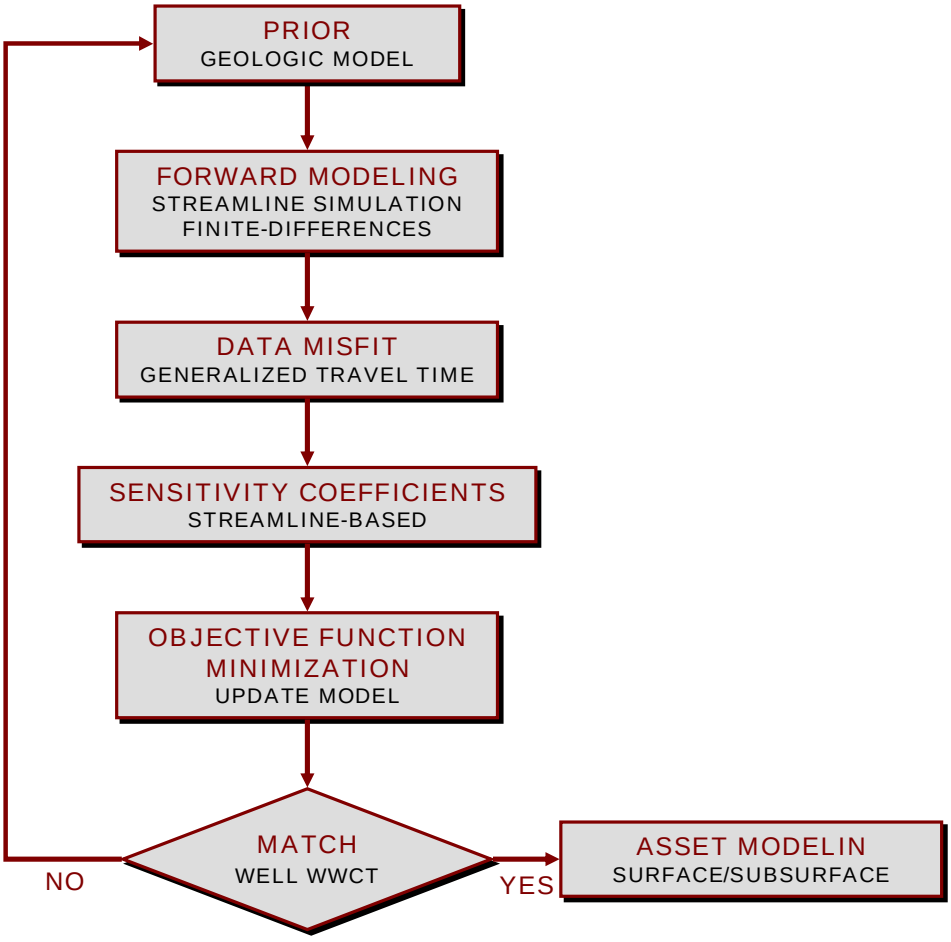

Fig. 3.2– Streamline-based production data integration workflow.

3.1.1. Forward Model

The production response and fluid flow in the reservoir might be obtained using either a streamline (SLS) or a finite-difference (FD) simulator. Besides computational efficiency, streamline models offer some unique advantages for production data integration to field-scale geologic models. Streamline simulators approximate 3-D fluid flow calculations by a sum of 1-D calculations along streamlines. The choice of streamline direction for 1-D calculations makes the approach extremely effective for modeling convection-dominated flows in the reservoir. This is typically the case when heterogeneity is the predominant factor controlling oil recovery, for example in waterflooding. Another important advantage of streamline models is that the computation time tends to show a linear-scaling with respect to the number of grid blocks and this makes the approach particularly well suited for large scale simulation studies involving multimillion cell geologic models.

When choosing a (FD) simulator, our objective is to take full advantage of not only (FD) but also (SLS). We'll utilize the (FD) versatility and resourcefulness in modeling complex physical processes, and the unique reservoir insight obtained when generating streamlines. Specifically streamlines are constructed based on numerical velocity fields generated by the (FD) simulator. Due to the complex geologic features present in hydrocarbon accumulations, an appropriate tracing in arbitrary faulted corner-point geometries becomes necessary. We'll follow the strategy presented in the previous chapter, which provides a consistent representation for streamlines and velocities near faults and non-neighbor connections. Recall that this novel approach will be based on a local (boundary layer) refinement construction that will be used to honor the fluxes at each face, without impacting the representation of flow within cells. The advantage of using a sophisticated FD simulator in this step is the straightforward incorporation of the full physics of fluids and flow, the disadvantage the high computational cost.

3.1.2. Generalized Travel Time Inversion

The next step in the production data integration approach is the quantification of the data misfit. We define a 'generalized travel time' (GTT) at each well for this purpose. In this approach, we seek an optimal time-shift Δt at each well so as to minimize the production data misfit at the well. This is illustrated in **Fig. 3.3** where the calculated water-cut response is systematically shifted in small time increments towards the observed response and the data misfit is computed for each time increment[34].

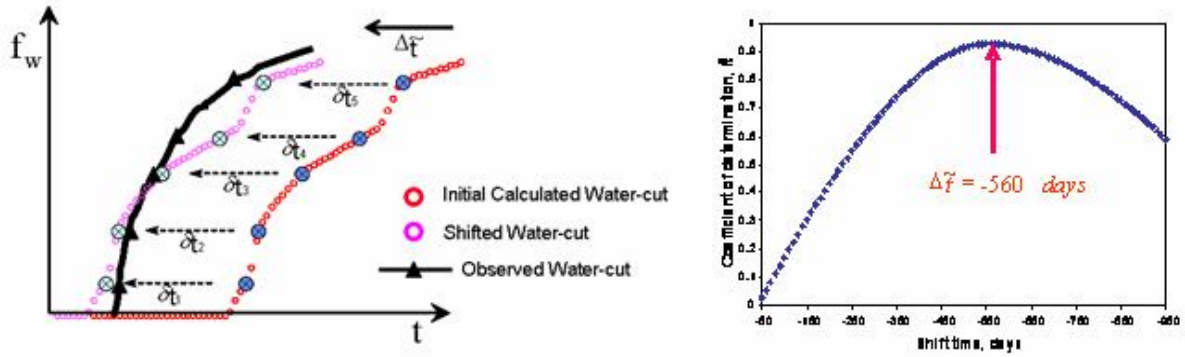

Fig. 3.3– Illustration of generalized travel-time inversion: (a) history-matching by systematically shifting the calculated water-cut to the observed history, (b) best shift-time which maximizes the correlation function.

The optimal shift will be given by the Δt that minimizes the misfit function,

$$J = \sum_{i=1}^{Nd} \left[y^{obs}(t_i + \Delta t) - y^{cal}(t_i) \right]^2 = f(\Delta t, m) \tag{3.1}$$

Or, alternatively maximizes the coefficient of determination given by the following

$$R^2(\Delta t) = 1 - \frac{\sum \left[y^{obs}(t_i + \Delta t) - y^{cal}(t_i) \right]^2}{\sum \left[y^{obs}(t_i) - \overline{y^{obs}} \right]^2} \tag{3.2}$$

Thus, we define the generalized travel time as the 'optimal' time-shift $\Delta\tilde{t}$ that maximizes the R^2 as shown in **Fig. 3.3(b)**. It is important to point out that the computation of the optimal travel time shift does not require any additional flow simulations. It is carried out as a post-processing at each well after the calculated production response is derived using a flow simulation. The overall production data misfit can now be expressed in terms of a generalized travel time misfit at all wells as follows,

$$E = \sum_{j=1}^{Nw} (\Delta\tilde{t}_j)^2 \tag{3.3}$$

The generalized travel time approach has been successfully applied to many field cases[1-8]. Furthermore, it leads to a robust and efficient inversion scheme because of its quasi-linear properties.

3.1.3. Streamline Based Sensitivities

One of the most important advantages of the streamline approach is the ability to analytically compute the sensitivity of the generalized travel time with respect to reservoir parameters such as porosity and permeability[33]. Even when using (FD), the generated numerical velocity field is used to derive streamline trajectories and carry out the sensitivity computations. The sensitivities form an important part of the data integration algorithm and can be expressed as one dimensional integral along streamlines[33].

In computing the generalized travel time, we shift the entire fractional flow curve by a constant time. Thus, every data point in the fractional-flow curve has the same shift time, $\delta t_1 = \delta t_2 = \cdots = \Delta\tilde{t}$, **Fig. 3.3(a)**. We can average the travel time sensitivities of all data points to obtain a rather simple expression for the sensitivity of the generalized travel time with respect to reservoir parameters *m* as follows,

$$\frac{\partial \Delta \tilde{t}_j}{\partial m} = -\frac{\sum_{i=1}^{N_{dj}} \left(\partial t_{i,j} / \partial m \right)}{N_{dj}} \tag{3.4}$$

This expression requires the sensitivity of the arrival times at the producing well, $\partial t_{i,j} / \partial m$. These sensitivities can be easily obtained in terms of the sensitivities of the streamline time of flight[22]

$$\frac{\partial t}{\partial m} = \frac{\dfrac{\partial \tau}{\partial m}}{\dfrac{\partial f_w}{\partial S_w}} \tag{3.5}$$

In the above expression, the fractional-flow derivatives are computed at the saturation of the outlet node of the streamline. Finally, the time-of-flight sensitivities can be obtained analytically in terms of simple integrals along streamline. For example, the time-of-flight sensitivity with respect to permeability will be given by

$$\frac{\partial \tau}{\partial k(\mathbf{x})} = \int_{\Sigma} \frac{\partial s(\mathbf{x})}{\partial k(\mathbf{x})} dx = -\int_{\Sigma} \frac{s(\mathbf{x})}{k(\mathbf{x})} dx \tag{3.6}$$

Where the integrals are evaluated along the streamline trajectory, and the ‘slowness’ which is the reciprocal of interstitial velocity, is given by

$$s(\mathbf{x}) = \frac{\phi(\mathbf{x})}{\lambda_t k(\mathbf{x}) \left| \nabla P(\mathbf{x}) \right|} \tag{3.7}$$

Note that the quantities in the sensitivity expressions are either contained in the initial reservoir model or are available after the forward simulation run.

3.1.4. Data Integration

This step involves computing the changes in the model parameters by means of a least-squares minimization technique that uses the streamline-derived sensitivity coefficients. This amounts to a linear expansion of the modeled production data in terms of the underlying model parameters. The data integration process must be iterated to self-consistency because the simulation model is not linear. When implementing such approach we must satisfy the following:

- Match the field fluid history within a reasonable tolerance,
- Preserve geologic realism by minimizing changes to the prior geologic model. This model is already including static data and available geologic information and
- Allow for smooth and large scale changes since production data has low resolution and cannot be used to infer small variations in properties.

This involves the solution of an underdetermined inverse problem. We follow a deterministic approach in which we start from the prior static model that already incorporates geologic, well log, and seismic data. This can be represented as the minimization of a penalized misfit function

$$\left\|\delta d - G\delta R\right\| + \beta_1\left\|\delta R\right\| + \beta_2\left\|L\,\delta R\right\| \tag{3.8}$$

In **Eq. 3.8** $\delta\mathbf{d}$ is the vector of generalized travel-time shift at all wells, i.e. the difference between the observed and simulated production response. **G** is the sensitivity matrix containing the sensitivities of the generalized travel time with respect to reservoir parameters. Also, $\delta\mathbf{R}$ correspond to the change in the reservoir property and **L** is a second spatial difference operator that is a measure of roughness. It is analogous to imposing a prior variogram or covariance constraint. The first term ensures that the difference between the observed and simulated response is minimized. The second term is a norm constraint that penalizes deviations of the updated model from the initial model. Finally, the third term, a roughness penalty, simply recognizes that production data has low

resolution and is best suited to solve large-scale structures rather than small-scale property variations. The minimum can be obtained by an iterative least-square solution of the augmented linear system[56,58].

$$\begin{pmatrix} G \\ \beta_1 I \\ \beta_2 L \end{pmatrix} \delta R = \begin{pmatrix} \delta d \\ 0 \\ 0 \end{pmatrix} \tag{3.9}$$

Where the weights $\beta 1$ and $\beta 2$ determine the relative strengths of the prior model and the roughness term. An important advantage of the streamline-based inversion is that the sensitivities of the production response with respect to reservoir parameters can be obtained semi-analytically using a single forward simulation. Thus, the approach can be orders of magnitude faster than perturbation based inversion schemes that may require multiple flow simulations depending upon the number of data points or model parameters. It is also conceptually simpler and easier to implement than variational approaches such as the adjoint method. This feature makes the present workflow well suited for dynamic conditioning for large multimillion-cell models.

3.1.5. Synthetic Example

To illustrate the generalized travel time inversion a two-dimensional nine-spot water flood model will be used. **Fig. 3.4(a)** shows the prior permeability map generated using conditional simulation. Streamline trajectories and time of flight are presented in **Fig. 3.4(b)**. The model was initialized enumerating pressure and water saturation to constant values. All producers were constrained by liquid rate (600 STB/D) and the injector by pressure (4,000 psia).

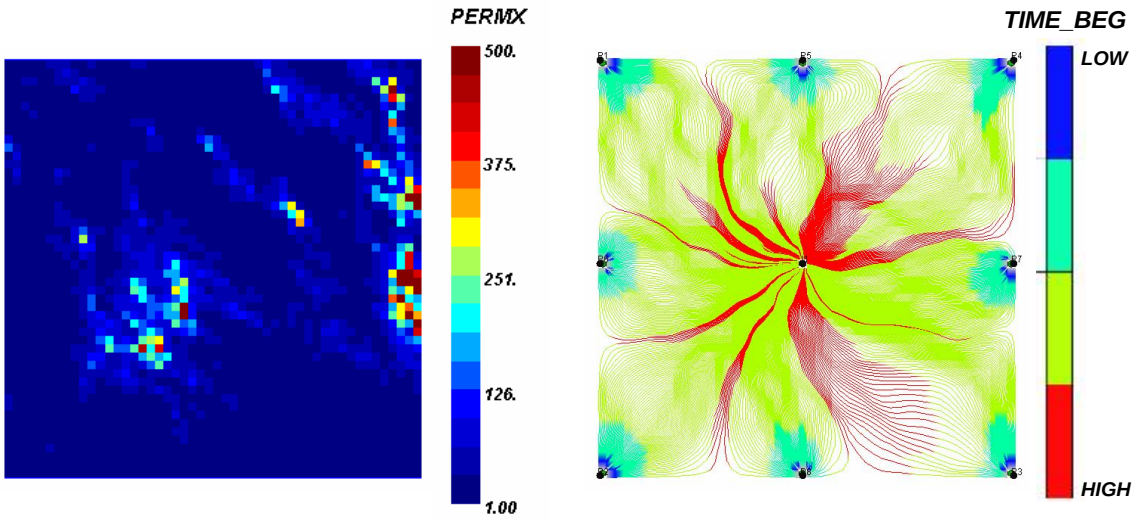

Fig. 3.4– (a) Synthetic permeability used to illustrate generalized travel time inversion, (b) streamline trajectories and time of flight for synthetic model.

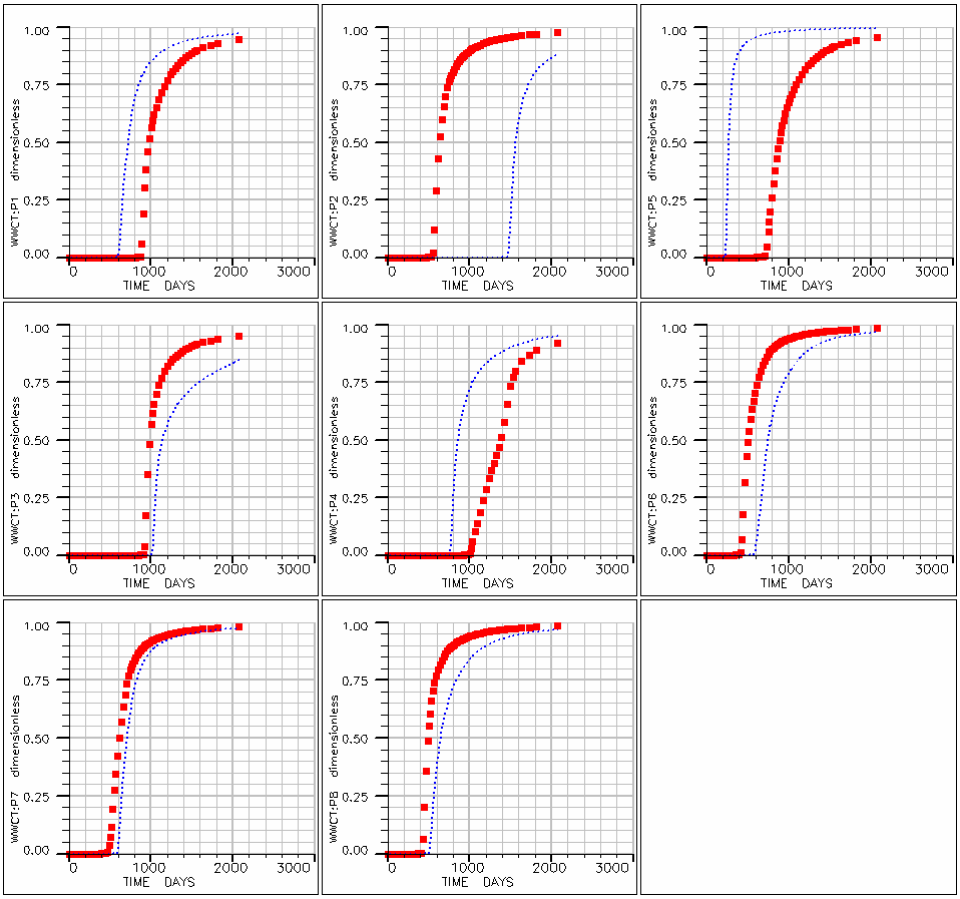

Fig. 3.5– Initial water cut match for synthetic model.

Fig. 3.5 shows the initial water cut match for each well. The given permeability field is only able to represent the water breakthrough in producer P7. The offset breakthrough times in the rest of producers range from ±1000 days. The model is predicting water with accelerated and delayed breakthrough times 3 years away from the observed data. Its eventual use for any prediction exercise will become a dangerous liability.

Our main objective is to integrate the water cut information without destroying the given permeability features. This reconciliation is accomplished after decomposing the underlying fluid flow pattern using streamlines and calculating the generalized travel time sensitivities of each well to permeability. **Fig. 3.6** shows the streamline trajectories and sensitivities for all wells after a full forward simulation. The color code represents the sensitivity magnitude for each cell. The blue color represents high sensitivity values and the maroon small values.

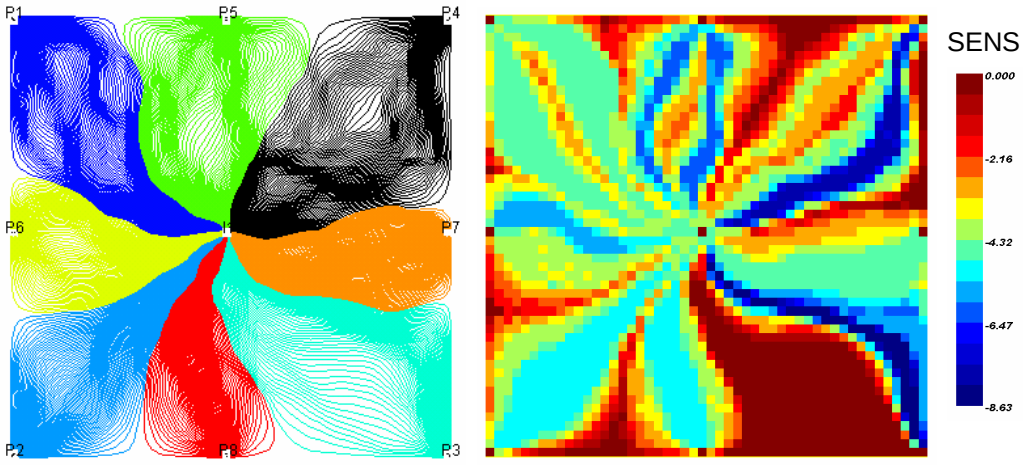

Fig. 3.6– Flow domain decoupling provided by streamline-based sensitivities.

Let's qualitatively examine the sensitivities a little bit more, as they might provide additional insight in how the flow domain is discretized. A high sensitivity could be associated with a high density of streamlines providing water to the producers; these cells will be the ones presenting significant permeability changes when required. Let's take a look at producer P4. Due to the high permeability surrounding this well, the streamlines

ending in it are likely to have a small time of flight and an early water cut. When compared to the observed data it can be seen how a significant shift time must be achieved to delay the water breakthrough. The sensitivities are showing a contrast which indicates which zones are contributing the water to this producer. After running the data integration we'll expect to see great changes all around these cells.

Another good example is producer P2, where a late simulated water breakthrough is observed. To increase the speed of the waterfront, streamlines providing water are to be considered for the sensitivity estimation and the sensitivity magnitude will determine how big the changes will be. From **Fig. 3.6** we can see how this magnitude is quite uniform through the whole drainage area. What this means is that considerable changes are expected for this well in order to delay the breakthrough time.

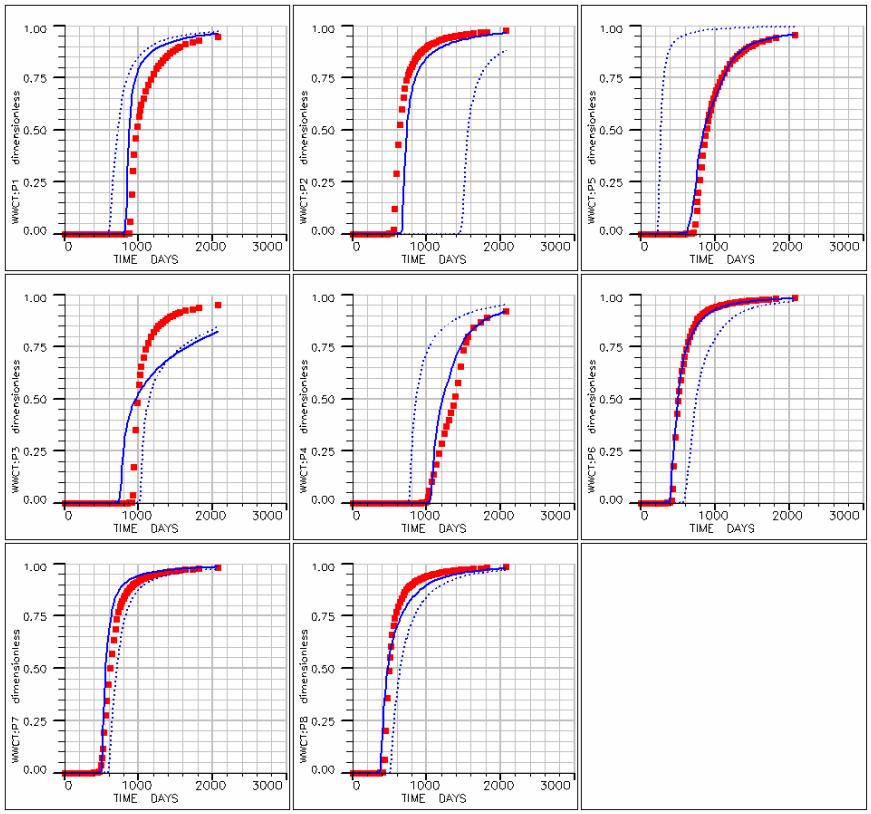

Fig. 3.7– Water cut performance before and after generalized travel time history match.

Fig. 3.7 shows the water cut match in all wells before and after the inversion. The results speak by themselves; in all 8 wells the water cut match was dramatically improved. The travel time misfit was reduced from 685 days to 65 (that's one order of magnitude) and the water cut misfit was reduced from 1.24 to 0.073 (more than one order of magnitude). Both travel time and water cut misfit are presented in **Fig. 3.8**. Note that the main changes are done through the first 3 or 4 iterations, this is a common behavior observed in previous applications.

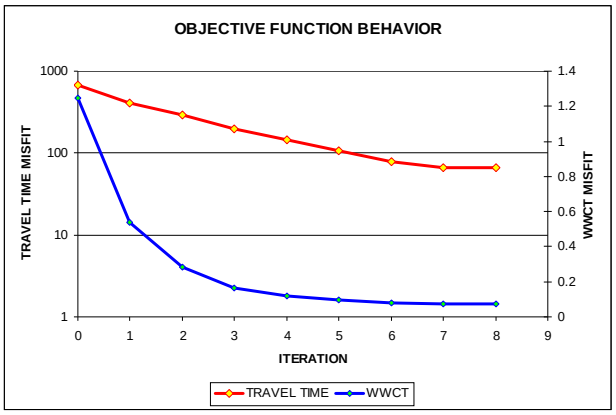

Fig. 3.8– Objective function behavior for heterogeneous five spot example.

After calculating the sensitivities the next step is to minimize the misfit function via LSQR optimization and update the permeability field. The main LSQR output is a deviation array that must be added to the permeability model. **Fig. 3.9(a)** shows the final updated permeability and **Fig. 3.9(b)** shows the deviation array after running all iterations. The blue color means that the permeability is decreasing and the red color that it's increasing. Note that the sign of the change is decided by the shift time obtained when evaluating the data misfit via generalized travel time. This picture is an excellent diagnostic indicator when addressing the presence or absence of barriers, fractures or even faults.

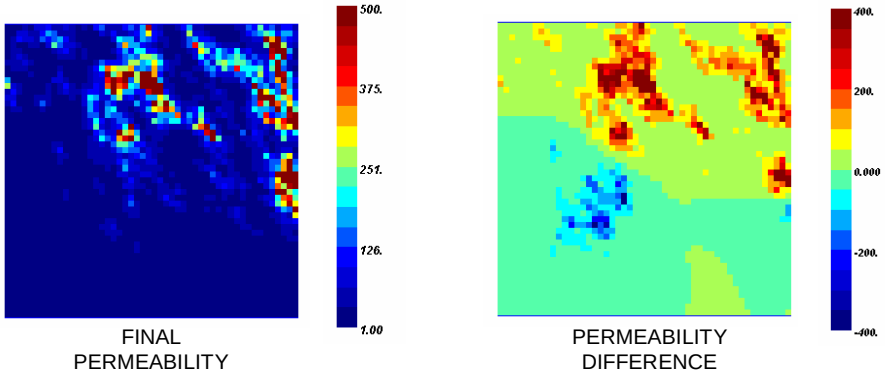

Fig. 3.9– (a) Updated permeability model after inversion (b) Difference in permeability after integrating production data.

An important validation step for the reconciled permeability is checking its moment's behavior. **Fig. 3.10** shows the histogram for the permeability before and after the inversion. Clearly we can see that we're preserving the first and second moments of the prior permeability.

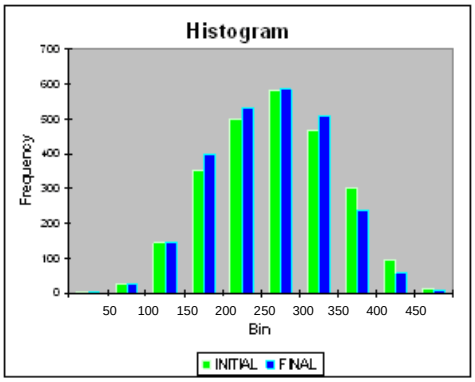

Fig. 3.10– Histogram comparison between final and initial permeability for nine-spot synthetic model.

Now that the generalized travel time inversion has been illustrated with a synthetic model, its application to field cases will be presented. We'll start with a giant middle-east field using streamline simulation as forward model and we'll conclude the chapter with an offshore field using finite-differences. In both applications post-processing strategies will be presented to maximize the GTT reservoir modeling capabilities.

3.2. Field Applications in History Matching Using Streamline Simulation

In this section we'll present the application of the streamline-based generalized travel time inversion to a giant Middle East field. Using highly detailed geologic and rock- fluid property models, over 30 years of production history within 170 wells were integrated to update the permeability distribution and quickly identify and reconcile discrepancies between geologic and dynamic modeling.

The method leads to significant savings in time and man power as we were able to integrate the production history in a period between 24 and 36 hours of computation time. To our knowledge, this is the first application of inverse modeling for conditioning geologic models with a million parameters to field production history.

The geologic model derived after conditioning to production response was used to identify the distribution and orientation of dominant fractures and preferential flow paths in the reservoir. A systematic analysis using statistical moments and facies-based vertical proportions was carried out to examine the geologic realism of the updated permeability model. Our results indicate the existence of extensive localized fractures with very high permeabilities associated to specific facies with no resulting lost in geologic realism.

3.2.1. Overview: Giant Middle East Oil Field

The reservoir under consideration is located in the middle-east and ranks among the largest hydrocarbon accumulations in the world. The field was discovered in 1948; production began in 1951 and reached its peak in the early 80's. Production was restrained in the middle 80's for market reasons and an aggressive development followed the 90's.

The initial geologic model was created based on well log derived porosity, facies information and 3-D seismic data. The facies model contains seven different indicators, mainly divided into dolomitic and non-dolomitic lithologies. From the facies based

porosity model, 3-D permeability distributions were generated using appropriate core based porosity-permeability transforms. Conceptual geology studies suggest that the field is naturally fractured. However, the static modeling stage didn't include any fracture modeling techniques. The geo-cellular model contains about 1 million cells representing a north-east striking anticline. The whole model is divided in several stratigraphic zones which played an important role in validating and locating the existence of natural fractures.

The initial water saturation was obtained using several facies-based J-curves and capillary-gravity equilibrium conditions. The oil-water contact dips more than 660 feet to the northeast. The contact is consistently higher on the west flank of the field than on the east, and a tar mat is associated with the original contact. Water injection wells are completed above this tar mat for pressure maintenance.

Production data smoothing is an important step during generalized travel-time inversion with field data. The field production history data are frequently erratic with large-scale fluctuations. Very often the time step sizes in simulation are larger than the intervals of observation data. Thus, the fluctuations within short time intervals in the production data are not captured by simulation. We suggest averaging (smoothing) the production data before inversion over pre-specified interval using the simulation time steps as guidelines. This helps the inversion capture the general trend of the production history and not be trapped by small details. Data smoothing also facilitates the calculation of the shift-time during generalized travel-time calculations. Typical production smoothing examples are presented for a few wells in **Fig. 3.11**.

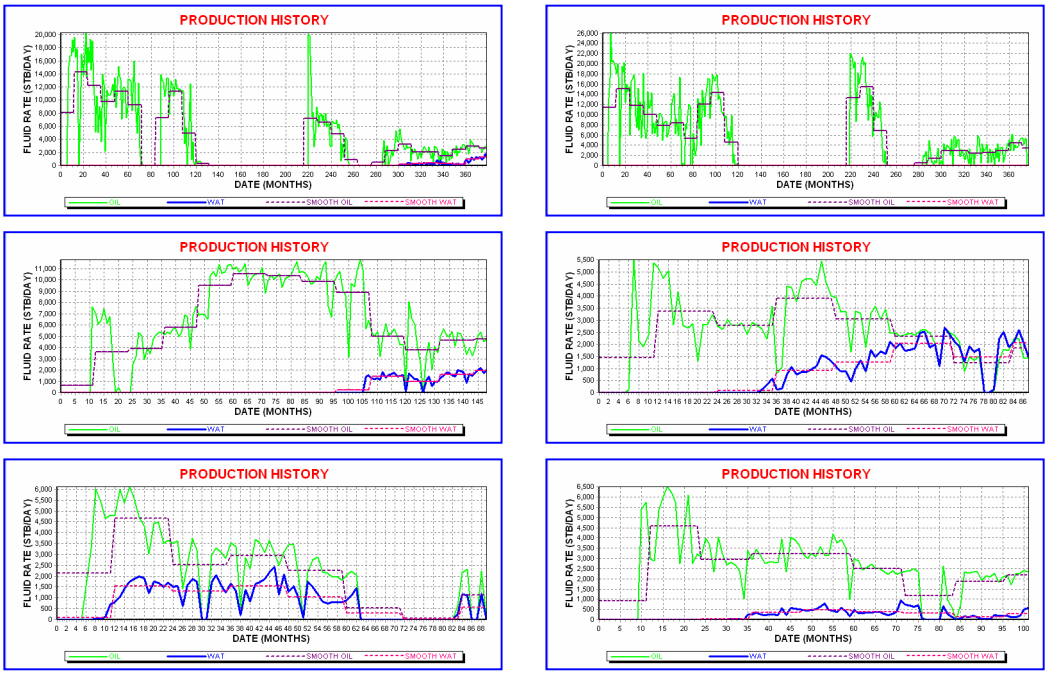

Fig. 3.11– Production smoothing examples for Middle East Field. The smoothing facilitates the shift time evaluation at all wells.

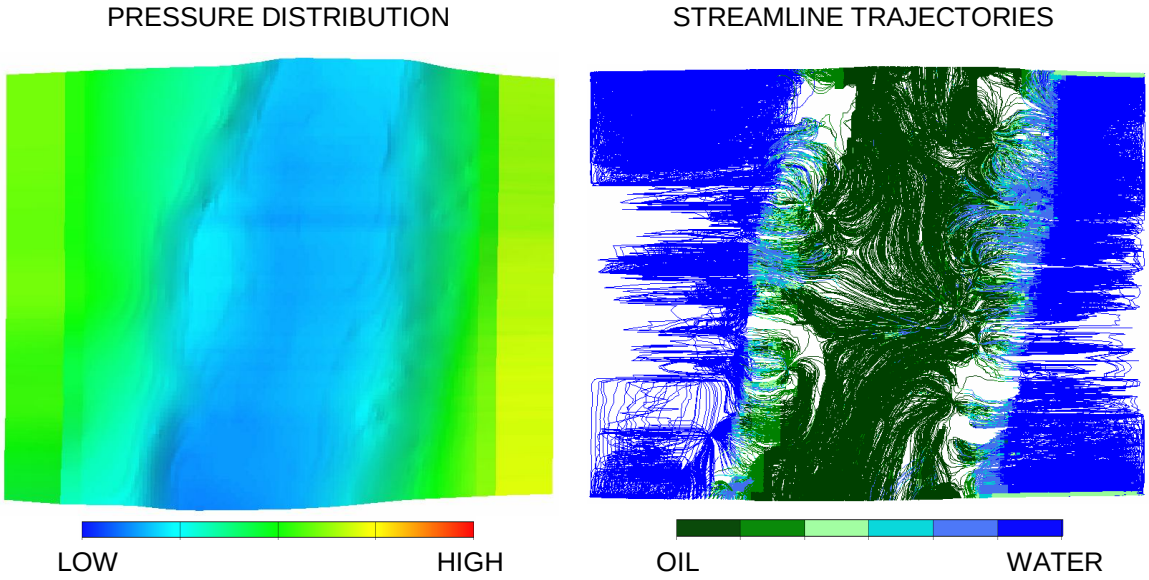

Fig. 3.12– Pressure distribution and streamline trajectories for last time step in forward simulation. The streamlines are displaying fluid distribution, unexpected and extensive flooded areas are identified.

Fig. 3.12 shows the streamline trajectories and field pressure for the prior model at the final time step of the initial forward simulation. The streamline trajectories also display the associated oil saturation in each streamline segment. It can be seen how the water has broken through earlier than expected and the existence of an extensive flooded area in the flanks of the area of interest.

The initial water cut match for a few wells (WWCT) is presented in **Fig. 3.13**. A common observation in several wells is the early breakthrough and quick rise in water cut. This problem is further serious; the majority of wells show water production where only oil is being produced. The prior model is failing in representing the observed production data and its reliability for further forecast diagnosis is simply not acceptable. Our objective is to let the GTT inversion handle all these problems, not only improving the water-cut performance, but also aiding in identifying important geologic features to re-visit and improve the static modeling stage.

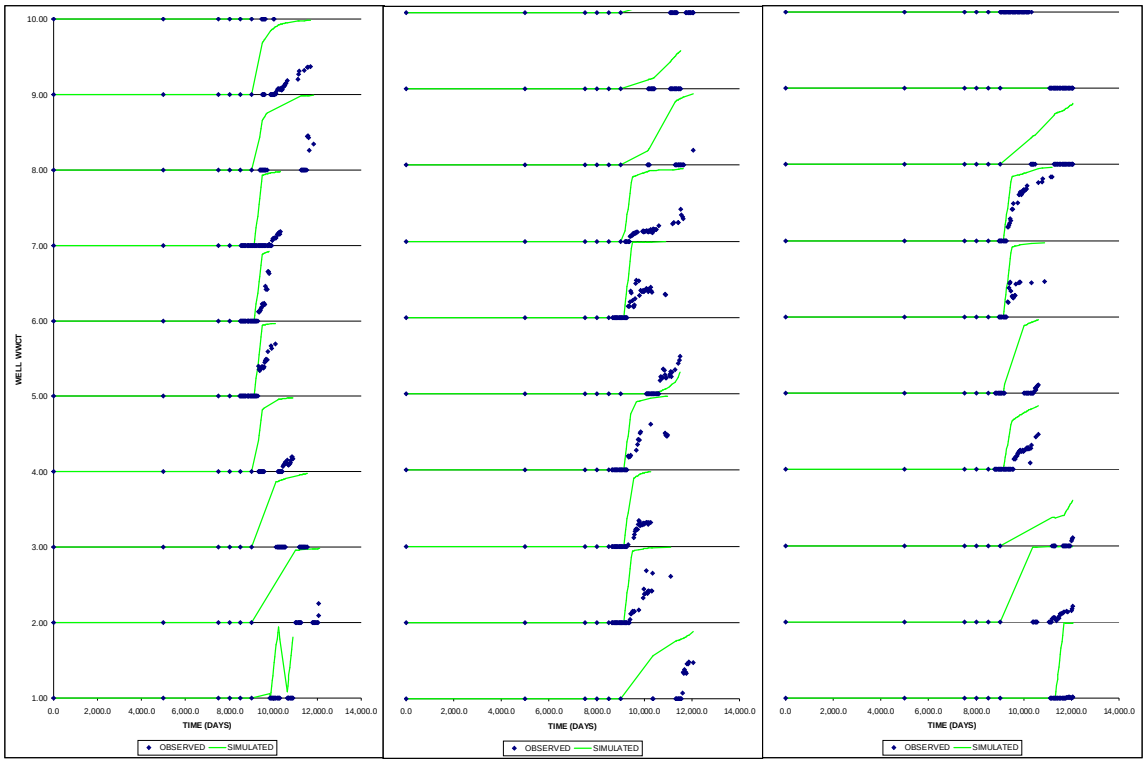

Fig. 3.13– Initial well water-cut match for Middle East field. The majority of wells show high water rates as opposed to the field history.

3.2.2. Inversion Approach and Results

After evaluating the performance of the prior model, two main discrepancies were observed: (1) early and extremely high simulated WWCT and, (2) significant water production in wells with no observed breakthrough. After running the GTT inversion a significant improvement in the overall water cut performance in all wells was observed. **Fig 3.14** shows a typical WWCT match improvement for a pair of wells. For the well presented in **Fig. 3.14(a)**, the initial water breakthrough occurred at 9,000 days with a travel time misfit close to 3,000 days. After breakthrough, water cut increased very fast reaching a 96% value after 8 years. After running the inversion, the breakthrough time was delayed and the whole observed water cut profile was matched. This delay represents a decrease in the permeability of those cells containing streamlines providing water to the producer. The well presented in **Fig. 3.14(b)** is another typical case where the initial amplitude match wasn't satisfactory because of the high and early water rates. The final amplitude match was significantly improved with a more consistent and representative rate performance.

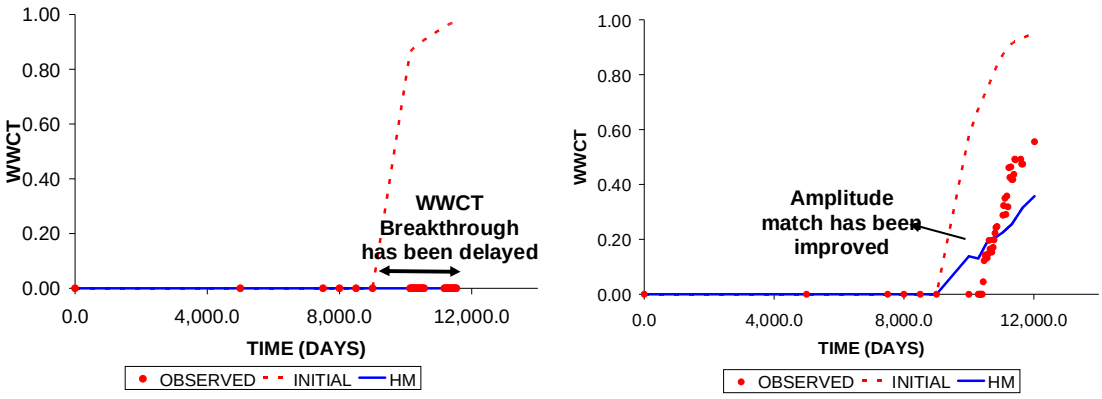

(a) *(b)*

Fig. 3.14– Illustration of GTT inversion improvement for Middle East field: (a) well illustrating delay in water breakthrough, (b) well showing improvement in amplitude match.

The initial and final WWCT match for several producing wells is presented in **Fig. 3.15**. Both travel time and amplitude match has been improved in more than 75% of the wells. The inversion managed to reduce drastically the WWCT to values closer to the observed range.

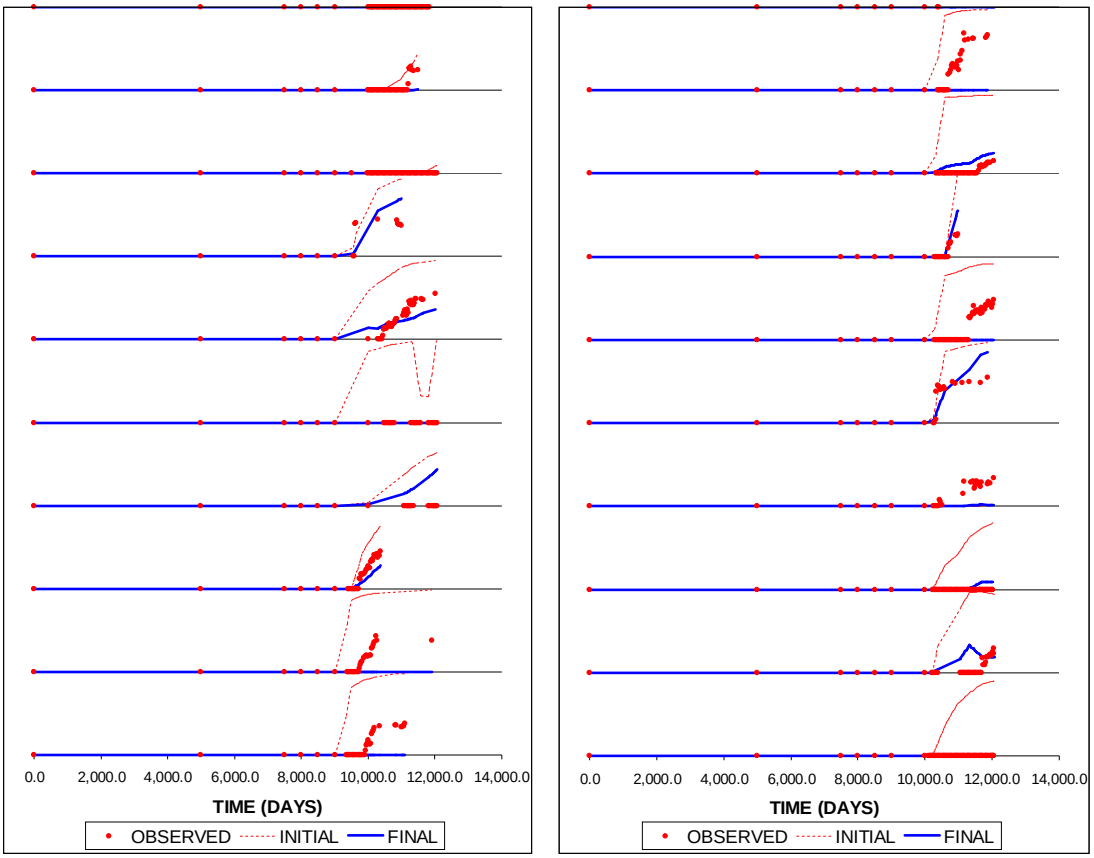

Fig. 3.15– Water cut history match for Middle East field after GTT inversion. History match was improved in 75% of active producing wells.

3.2.3. Impact in Prior Geologic Model

After reviewing the water cut match at the wells, a detailed look at the changes in permeability was performed in a layer by layer basis. The main objective during this step is to locate significant changes in the prior model, which eventually will provide foundations to justify the existence of fractures. Results are presented for a few representative layers in **Fig. 3.16**. The left pictures represent the prior model, the middle

the history matched and the right pictures the difference between the final and initial permeability attribute. The red cells on this right picture represent the decrease in permeability and the white cells the increase.

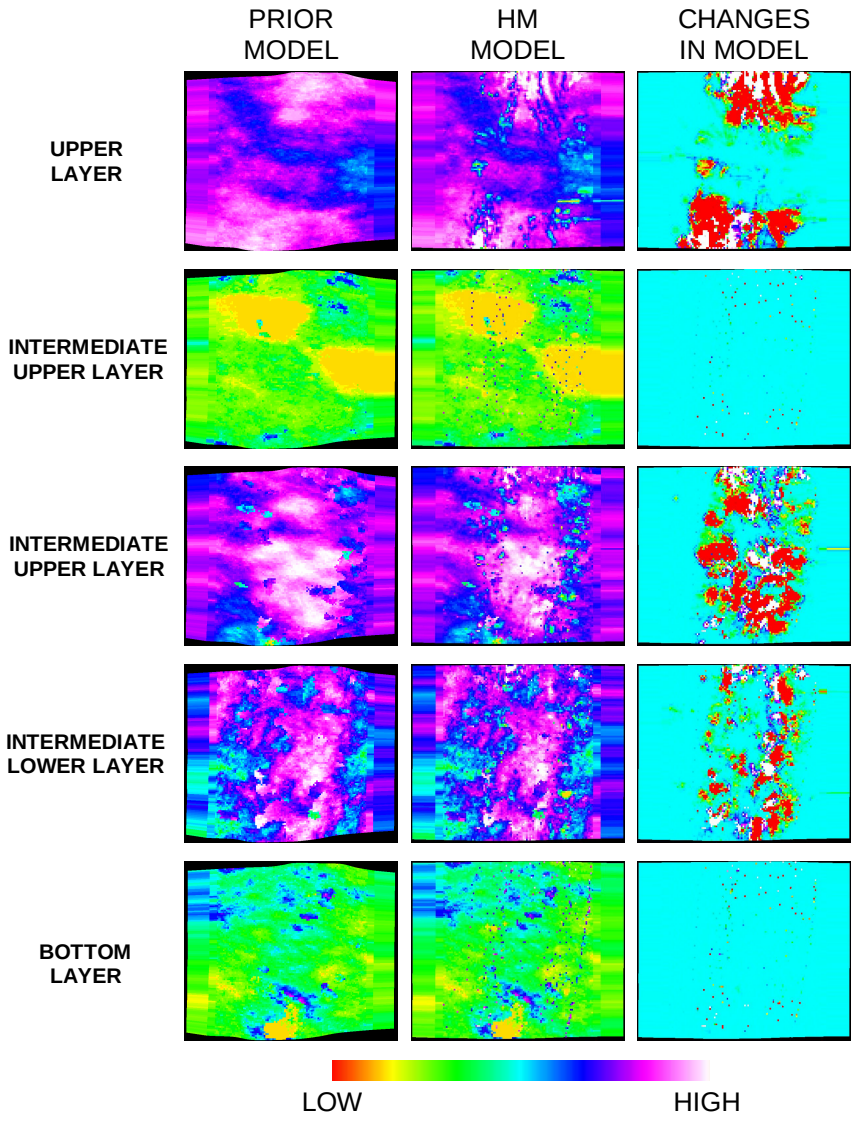

Fig. 3.16−Permeability comparison between prior and history matched geologic model for Middle East field. The GTT inversion localized changes in layers dominated by dolomitic facies.

A first impression shows a considerable change in permeability throughout the whole vertical section. There's a substantial permeability contrast in both north and south regions within the upper layers. In the northern region, permeability channels intercalated with permeability barriers have appeared after the inversion. A very encouraging observation is the lack of changes in those layers dominated by non-dolomitic facies. These layers are located in the intermediate upper and bottom layers. The intermediate upper layers show extensive decrease in permeability located in both flanks of the structure. This decrease is an indicator of these cells being in part responsible for the early simulated water breakthrough.

One of the questions the inversion must answer is which lithologies are having the most substantial changes in permeability. Any sizeable changes may indicate the presence and location of fractures. Before localizing these changes, it is necessary to picture how big these changes are. In **Fig. 3.17** the first moment for each lithology is presented before and after the inversion. Although we were expecting a decrease in permeability to delay the water-cut profiles, the average values increased substantially. Such increases are greater in the dolomitic facies.

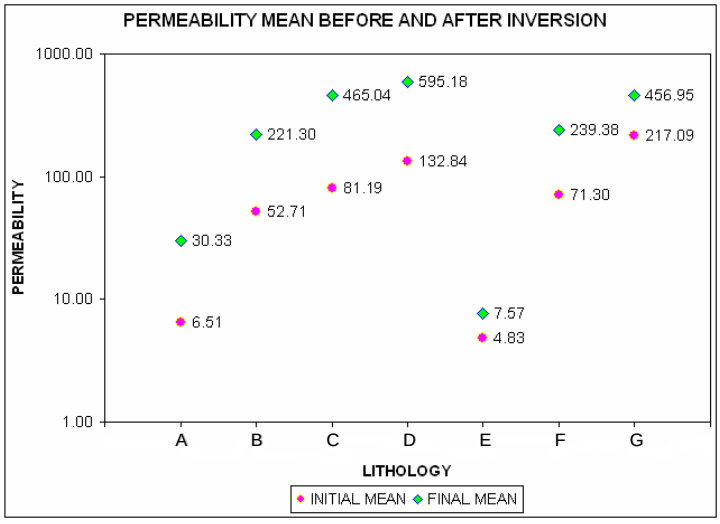

Fig. 3.17– First moment behavior for facies before and after the inversion for Middle East field.

With evidence of considerable changes from the mean behavior, permeability histogram functions for each facies were built before and after the GTT inversion. The functions are presented in **Fig. 3.18**; the following remarks can be made,

- *Lithology A (non-dolomitic)*, one of the 3 lithologies with low permeability (0.001-100md). Both probability functions show multimodal behavior. However, there's a considerable reduction in permeability that can be seen on the right tail of the posterior histogram.
- *Lithology B (non-dolomitic)*, this is another lithology with low permeability when compared to the rest. On the right half of the prior histogram zones of 20 and 200 md were removed by the inversion. The left tail of the posterior histogram shows a greater occurrence of low permeability values.
- *Lithology C (non-dolomitic)*, prior model showed a multimodal histogram which was preserved during the inversion. This lithology showed little change to the inversion approach except for the increase in the number of permeability values between 0.5 and 1 md.
- *Lithology D (dolomitic)*, this is a lithology with good reservoir properties, the right tail in the posterior histogram is clear evidence that the inversion increased the initial permeability. This kind of behavior is quite important, since it might be the foundation to make the statement of fracture presence in the model and within a particular lithology.
- *Lithology E (dolomitic)*, this is perhaps the lithology with the most extensive changes in permeability. The increase in permeability is quite considerable indicating that this lithology is most likely to contain predominant fractures.
- *Lithology F (dolomitic)*, the tail end to the right in the posterior histogram is a clear indicator of substantial increase in permeability.
- *Lithology G (dolomitic)*, this lithology is quite interesting. Although there's a permeability increase in the posterior histogram (tail to the right); within the right half of the prior histogram, zones of 200 up to 500 md were removed after the inversion.

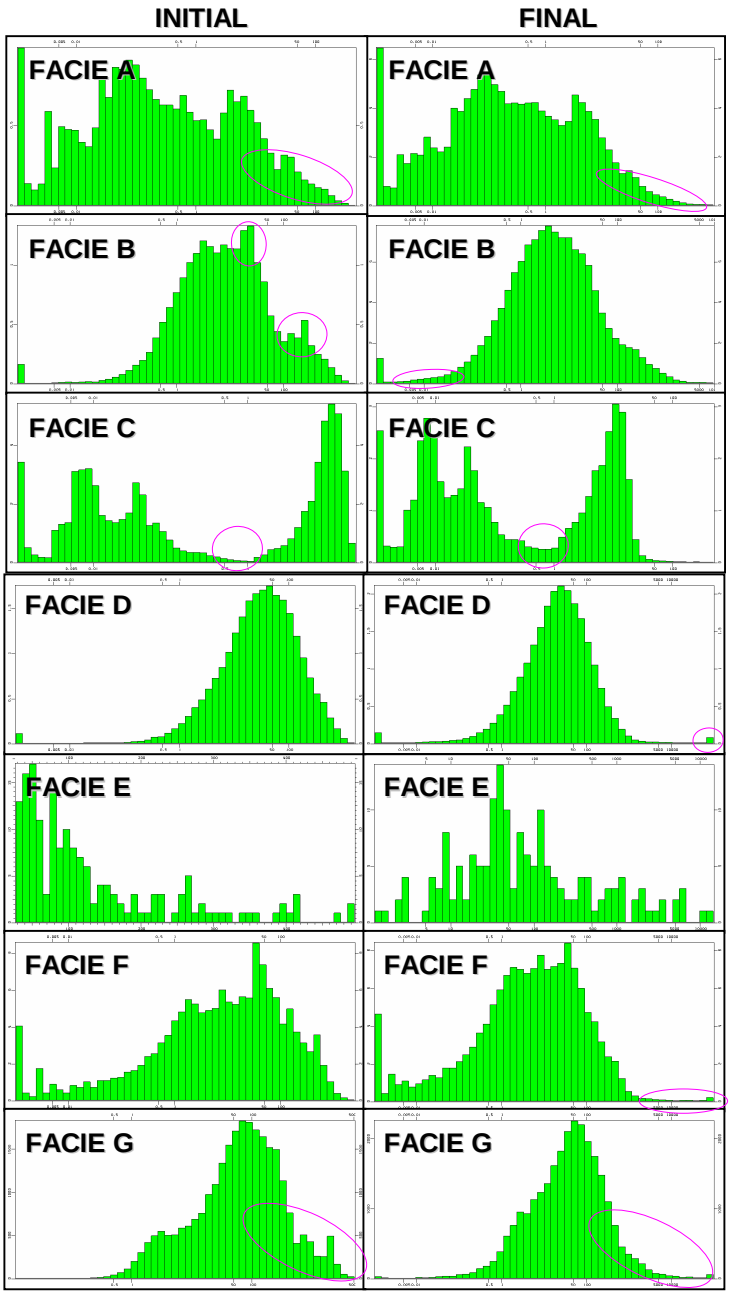

Fig. 3.18– Permeability histogram for each facie before and after the GTT inversion. The tails in the histograms provide foundations to locate fractures in the model.

The high permeability values observed in the histograms are the first evidence of fractures in the model. However a substantial localized decrease of permeability is

necessary to delay the water breakthrough in all wells. The starting point to locate these geologic features is to come up with pictures that encapsulate the global permeability behavior. The simplest one is a vertical section with the mean and median for each stratigraphic zone before and after the inversion. This set of curves is presented in **Fig. 3.19**. In **Fig. 3.19(a)** it can be seen how the permeability mean has increased in all layers as a result of the high permeability values generated by the inversion. Due to these high permeability values, the standard deviation has increased considerably. However, when comparing the median, **Fig. 3.19(b)**, what the inversion has really done is decrease the global permeability. This was expected due to the delay observed in the simulated water cut. All these observations start pointing towards the existence of localized fractures in the model. The question to answer is where these fractures are.

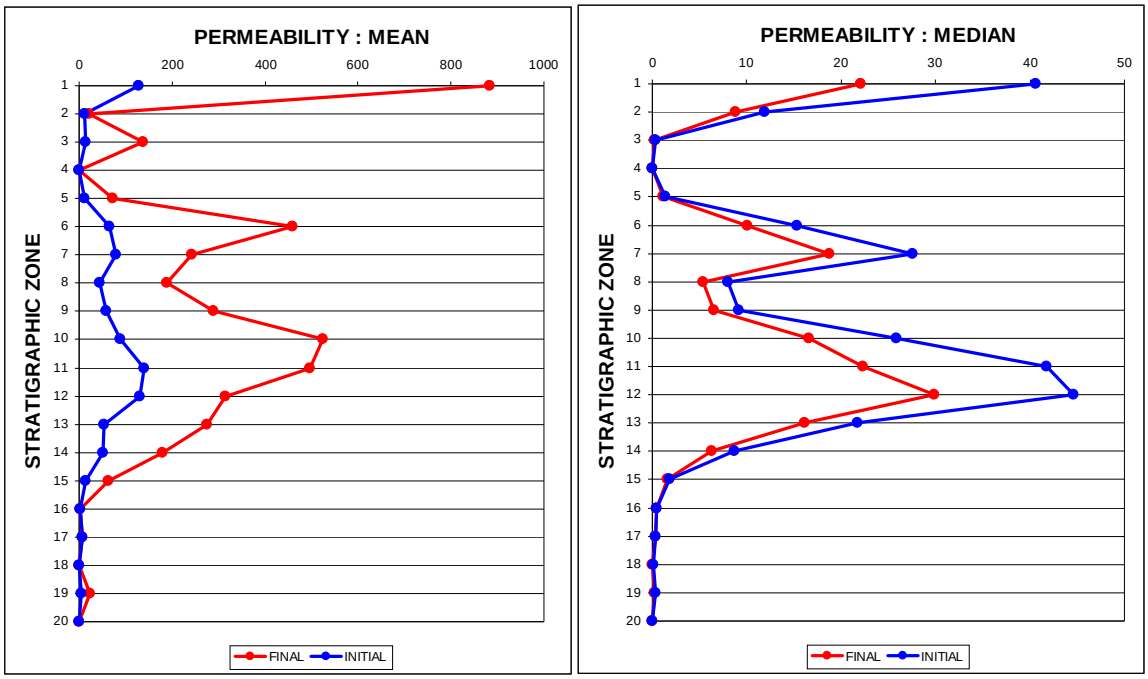

(a) *(b)*

Fig. 3.19−Vertical sections showing mean and median behavior before and after the GTT inversion. (a) Mean behavior, permeability average has increased throughout the entire vertical section. (b) Median behavior, what the GTT inversion has done is decrease the permeability in the model.

Another efficient and simple way to recognize the global and local changes in permeability is done overlapping the initial and final permeability. We present results for a few stratigraphic zones in **Fig. 3.20**. The blue dots represent the initial permeability and the purple ones the permeability after the GTT inversion. As we were expecting, there are very high permeability values located in specific stratigraphic zones and an extensive decrease in permeability. In zone **5** the permeability has been drastically reduced to delay the water breakthrough. In zones **2** and **11** we can undoubtedly see high permeability streaks that can only be explained with the presence of fractures. Zone **18** shows no major changes; this zone is dominated by non-dolomitic facies and is a strong indicator that the inversion is locating its changes to the productive facies.

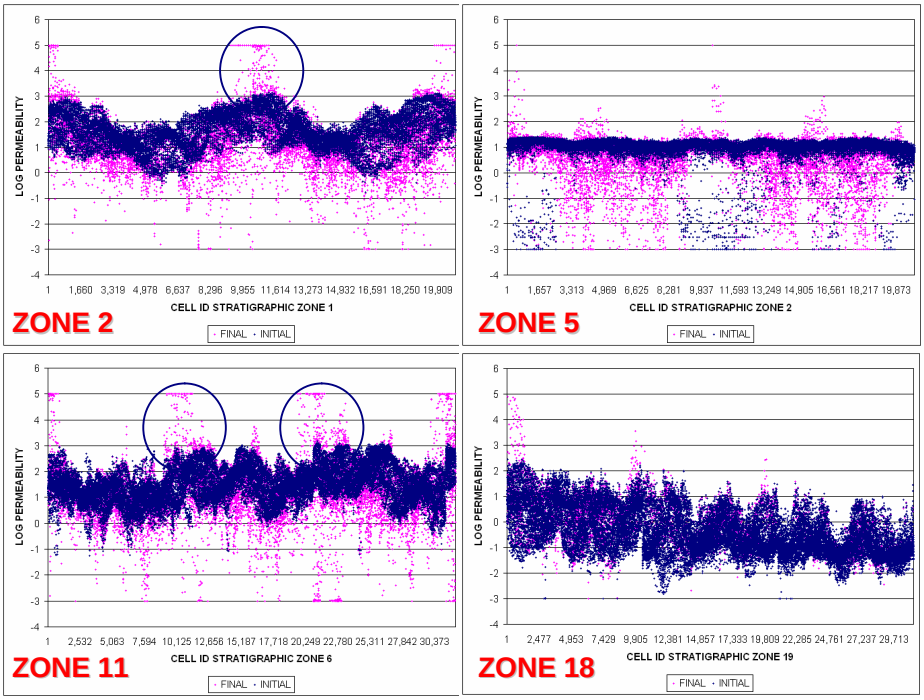

Fig. 3.20– Series showing permeability before (blue) and after (purple) the GTT inversion. The high streaks are evidence of the fractures location.

So far we have shown the evidence of large scale changes in the prior model that can only be explained with the presence of localized fractures. We have also shown that

in order to delay the early and high simulated water cut, there must be substantial decreases in permeability. However, the most important question still remains unanswered: which lithology is likely to be fractured? Where're these fractures located? Is the reduction in permeability also associated to a lithology?

To tackle these questions we used the concept of vertical proportion curves (VPC). These curves are nothing else but piled bar diagrams condensing the vertical evolution of any property and its lateral changes. **Fig. 3.21** shows a simple example of how they're calculated. Basically a discrete or continuous range is defined among the property and cells within a layer are counted to eventually calculate the proportions.

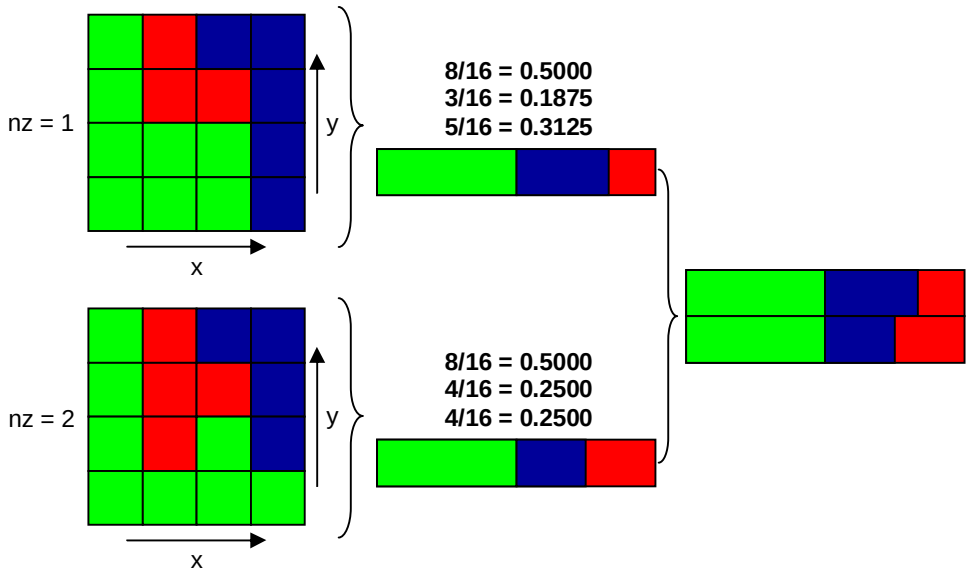

Fig. 3.21– Illustration of how to construct vertical proportion curves.

Fig. 3.22 shows the VPC for the lithologies and permeabilities before and after inversion. Understanding the lithology using the VPC is quite intuitive; however, for a successful use of these curves the conceptual depositional model should be consistent with the vertical evolution of lithologies. To use the curve we just need to go to a particular layer and read the proportions, for instance layer 1 in **Fig. 3.22(a)** has over

95% of non-dolomitic lithology **B** and less than 5% of dolomitic lithology **G**. The bottom layers are dominated by lithology **A** with a small occurrence of lithology **G**. The mid layers have mixed proportions of all occurring lithologies.

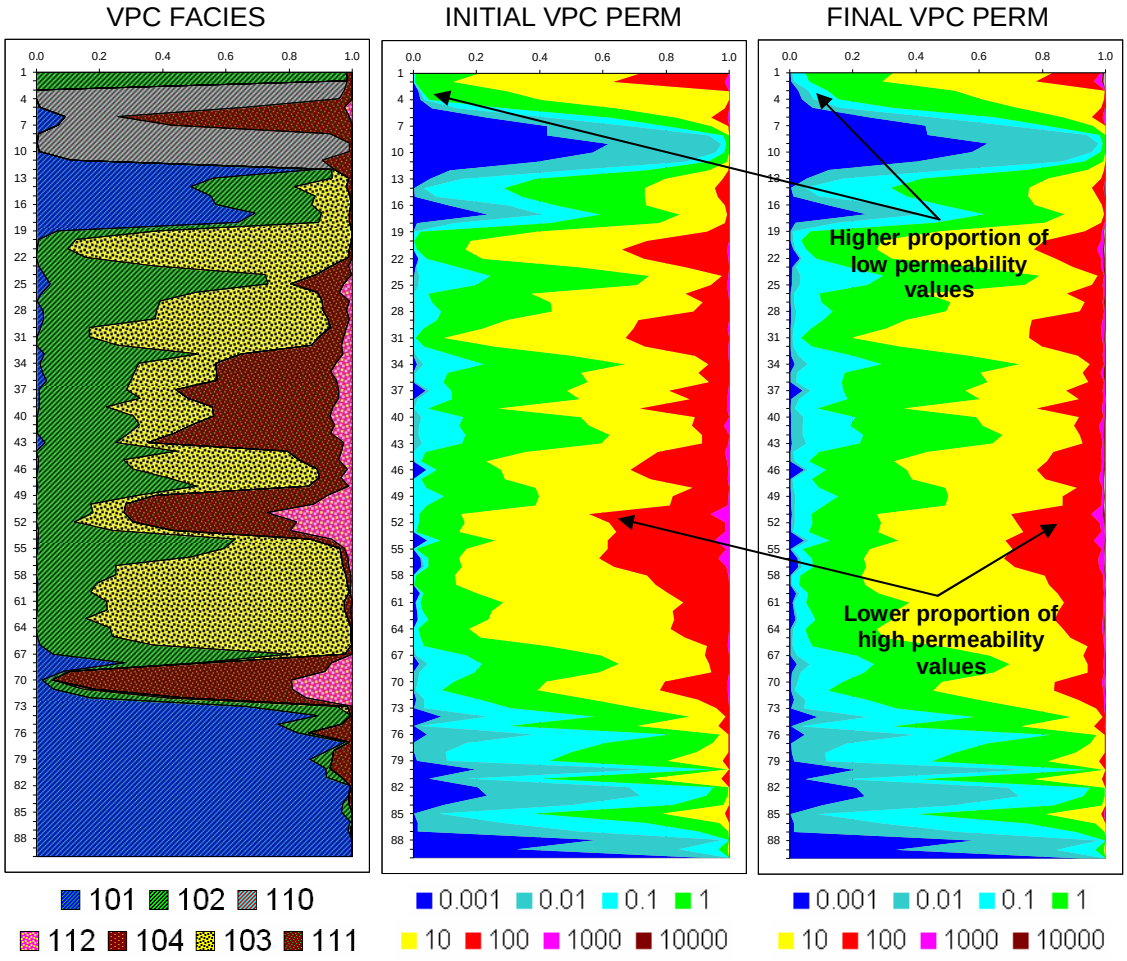

Fig. 3.22– Facies based proportion examination to inversion changes in geologic model. (a) Facies VPC for entire reservoir, (b) permeability VPC before inversion and (c) permeability VPC after inversion.

The permeability VPC, **Fig. 3.22(b)** and **Fig. 3.22(c)**, is a little different; unlike lithology, permeability is a continuous variable. Essentially, the colors indicate the proportion of cells occurring within a particular range. As an example, in layer 10 over 50% of cells are within the range of blue which according to the legend are those

permeabilities greater than 0.001 md but less than 0.01 md. In this very same layer, only 1% of the permeability occurrences are within the green region; such color represent those values greater than 1.0 md but less than 10 md.

Having the lithology and permeability VPC at the same level, we now have a useful tool to locate where the fractures are occurring and to which lithology they're associated. The inversion is really doing and excellent job preserving the overall permeability proportions but there're also big changes. For example, in layers 1 and 2 in **Fig. 3.22(b)** and **Fig. 3.22(c)**, the light blue color in the final VPC shows that the proportion of low permeabilities values has increased to 5%. We can also detect proportion changes in the green, yellow and red ranges. The green and yellow correspond to higher proportion of low permeability values which are explained by the delay in water cut. The smaller red area relates to a reduction in high permeability values (100-1000md) that again obeys to the water cut profiles.

All these reductions are good news, but the changes must also satisfy the high rates in the model and this can only be achieved with high permeability values available in fractured environments. A closer look is presented in **Fig. 3.23** where the proportion of extremely high permeability values (light blue and maroon) has clearly increased in the final VPC. The maroon and light blue colors show that 1% of the permeability has increased significantly verifying the existence of localized fractures. With such features we're now in a very convenient position to determine how the fractures are proportionally distributed throughout the stratigraphic model.

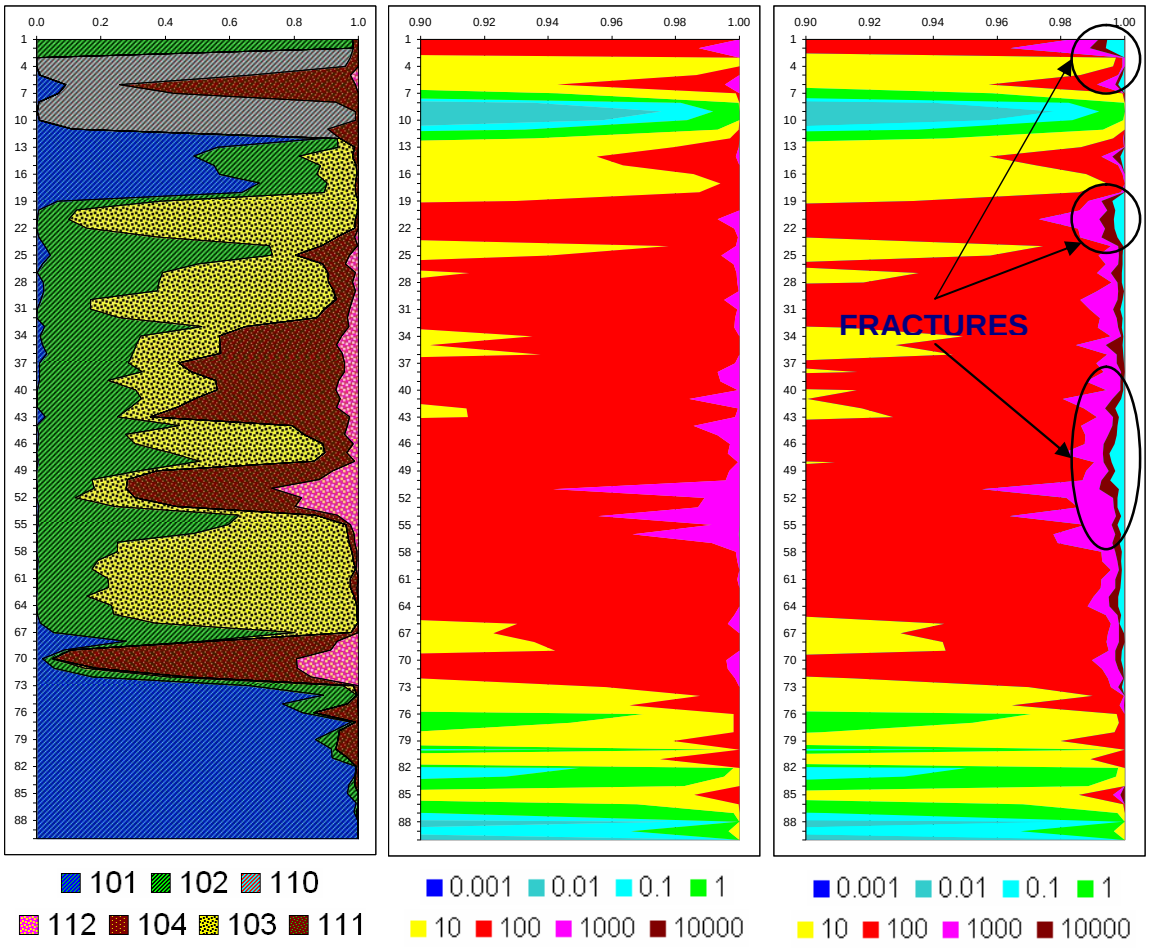

(a) *(b)* *(c)*

Fig. 3.23– High permeability proportion examination to inversion changes in geologic model. (a) Facies VPC for entire reservoir, (b) permeability VPC before inversion and (c) permeability VPC after inversion.

Now that we're able to locate the fractures in the vertical section, let's see which lithologies are likely to be fractured and where. Using the VPC approach we tackled each lithology separately. The results are presented in **Figs. 3.24** through **Fig. 3.28**. In each figure we extracted the prior and posterior permeability for each lithology and built the corresponding VPC. We also subtracted the final and initial VPC to identify the stratigraphic zones where the major changes are occurring. In our convention, a positive proportion value will represent an increase in the number of cells and a negative value a reduction.

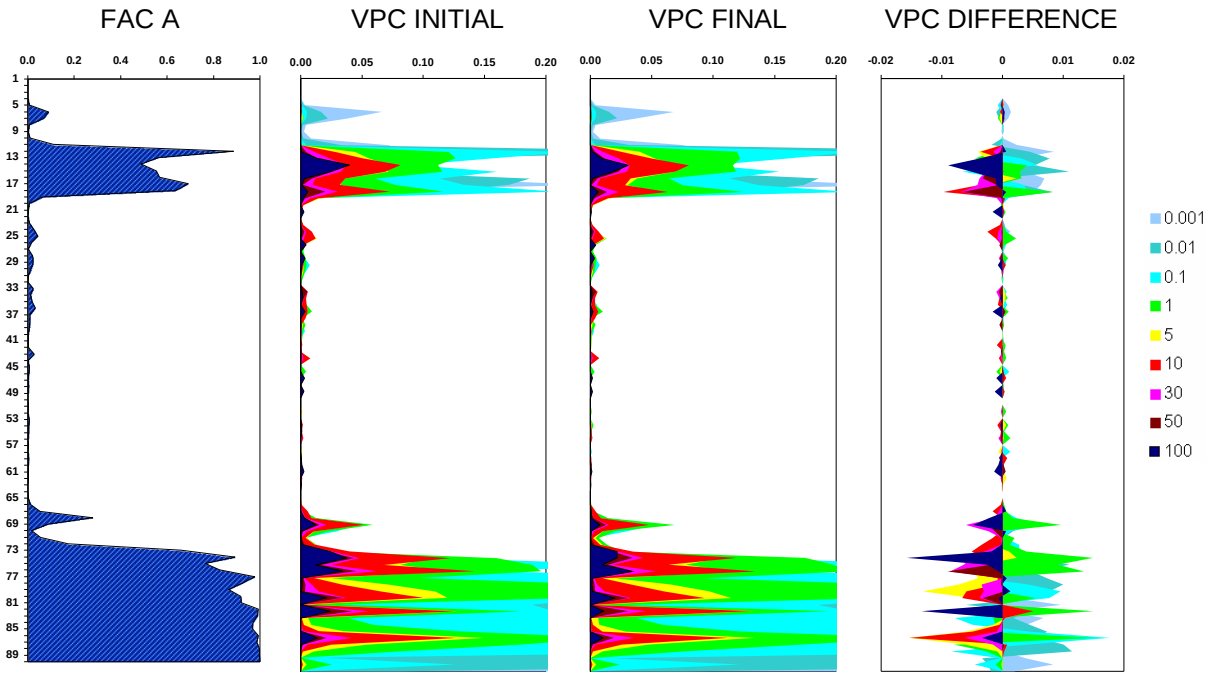

Fig. 3.24– VPC diagnosis to locate fractures in lithology A.

Fig. 3.24 shows the VPC diagnosis for lithology **A**. We know from descriptive statistic that this is a non-dolomitic facie with bad reservoir quality. The occurrence of this lithology is in the upper and bottom stratigraphic zones and the permeability varies form 0.001 to 400 md. From the VPC difference we can see how the inversion is decreasing the permeability significantly (dark blue area shifted to the left). This reduction is entirely related to the quality of this rock; the GTT inversion is suggesting that this facie should have a smaller magnitude.

Fig. 3.25 shows the same diagnosis to lithology **B**, permeability has gone down a little bit, but the changes are almost negligible. It's encouraging to see how the inversion is honoring the petrophysical characteristics of this facies by minimizing the changes to it. An interesting remark is the large increase in permeability through the upper layers. This lithology is unlikely to be fractured; so it's very likely that such magnitude change is related to structural origins or boundary effects.

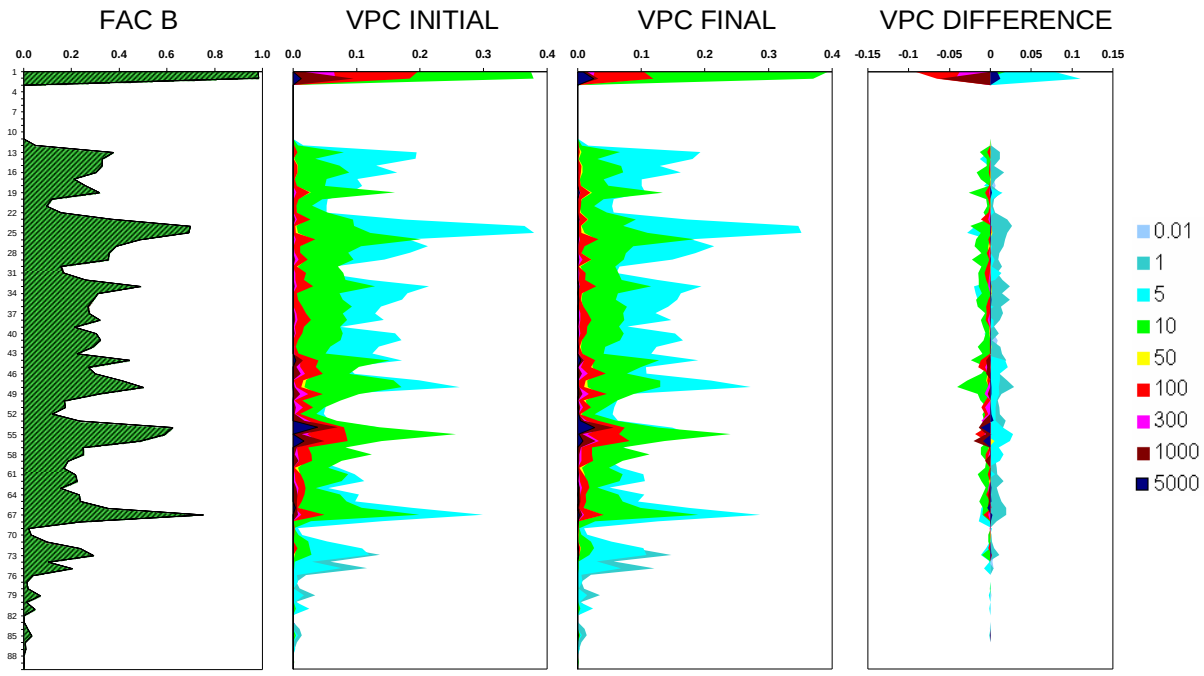

Fig. 3.25– VPC diagnosis to locate fractures in lithology B.

Having reviewed the non-dolomitic lithologies, we can state that the inversion has minimized the changes to these rock facies**.** We'll now discuss what happened to the dolomitic lithologies. Lithology **D** in **Fig. 3.26** shows a localized increase in several zones. It's also important to note the significant reduction in permeability, represented by the light blue area shifted to the right. This reduction is definitely associated to the dynamic model to delay the water breakthrough in wells. However, to balance the production rates the inversion has localized fractures in the model.

Lithology **F** (**Fig. 3.27**) shows a similar behavior. There're little changes in the upper zones, however the changes in the intermediate zones indicate fracture existence. It's also interesting to note how the occurrence of high permeability values intercalates between the stratigraphic zones. This behavior might indicate vertical discontinuity within fractures for a particular zone which is not the case in lithology **D** where the permeability always went up.

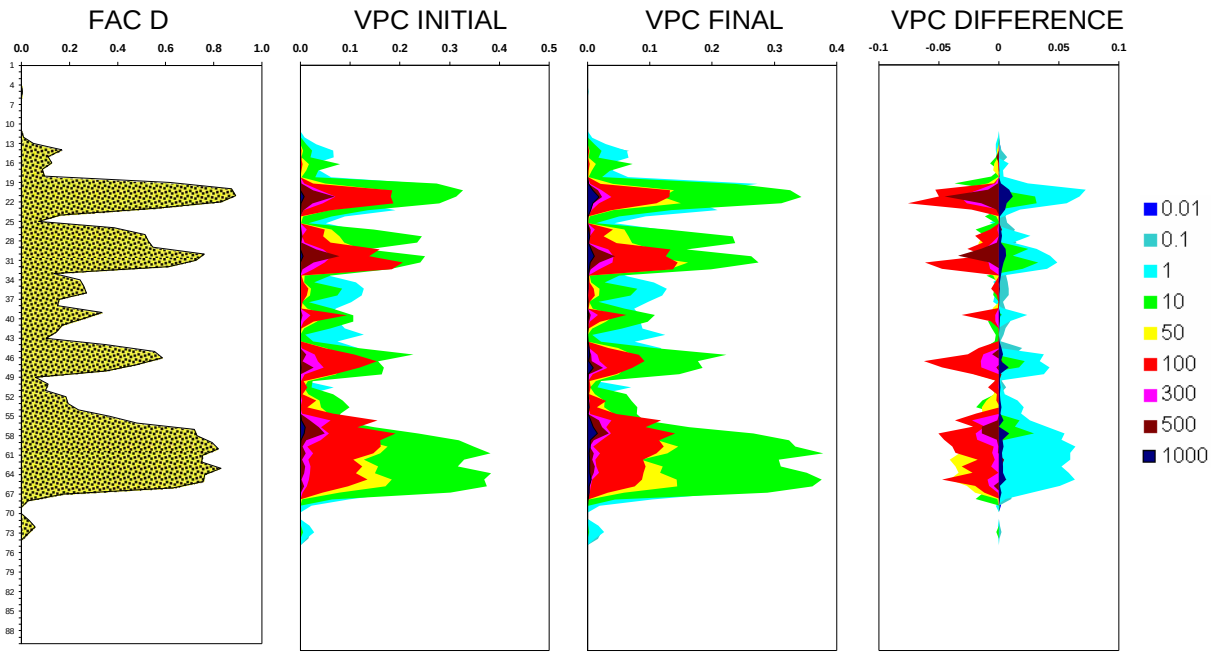

Fig. 3.26– VPC diagnosis to locate fractures in lithology D.

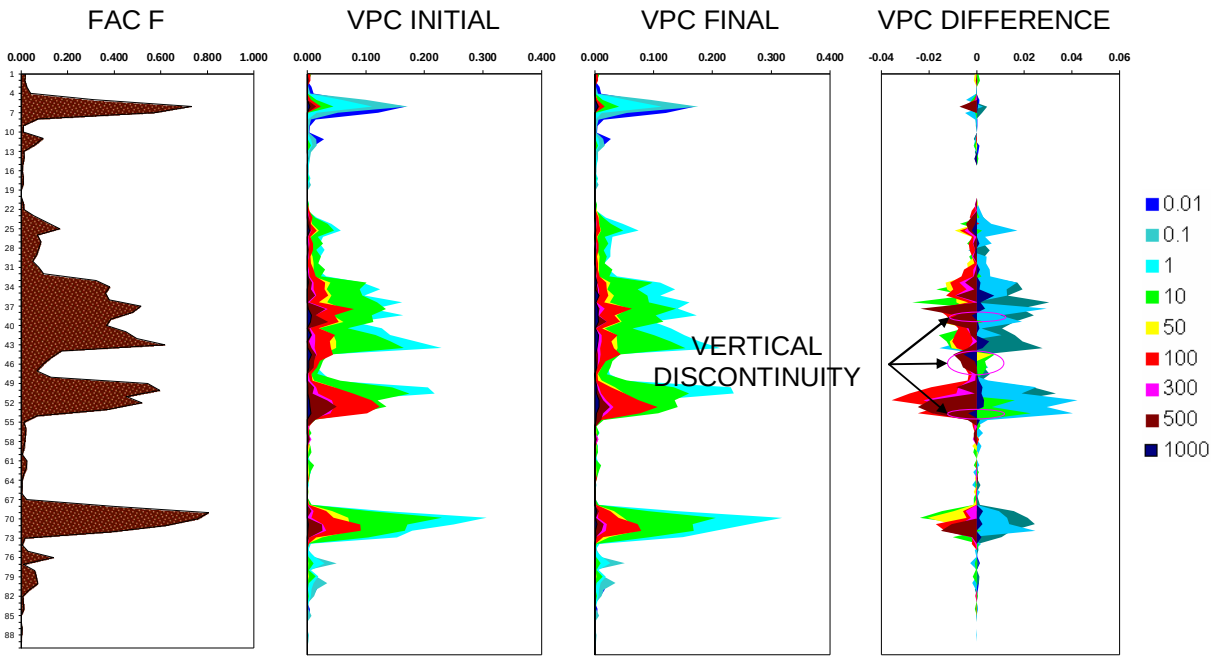

Fig. 3.27– VPC diagnosis to locate fractures in lithology F.

Considering the behavior of lithologies **D** and **F**, we were expecting to see the same pattern in lithology **G**, **Fig. 3.28**. Unlike the other lithologies, the permeability has been dramatically decreased by the inversion in all zones where this lithology exists. This could be an indicator that the quality of this lithology must be reevaluated.

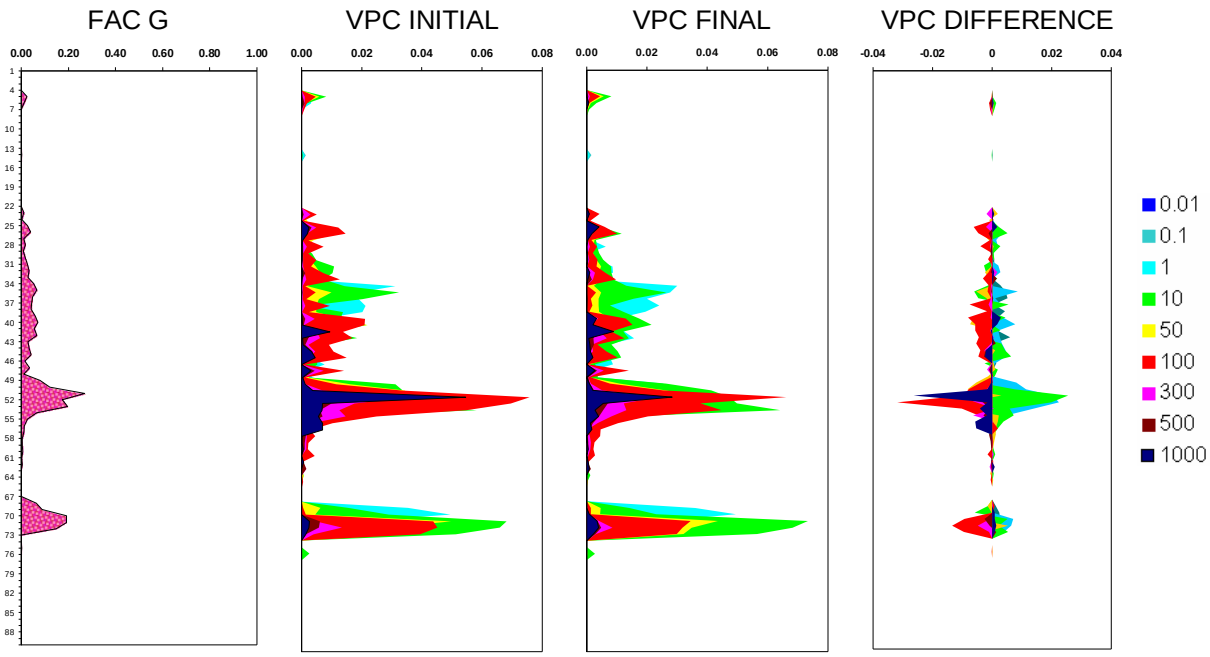

Fig. 3.28 – VPC diagnosis to locate fractures in lithology G.

To summarize the results, detailed looks at the facies-based statistical moments of the permeability indicate that the fractures appear to be located primarily in the dolomitic facies. The non-dolomitic facies have undergone a reduction in permeability to account for late water breakthrough in the field. Further examination of the facies-based vertical proportions of permeability ranges before and after the integration of water-cut data reinforces the conclusion that the fractures are localized in nature.

We'll now present a different field application in which instead of using streamline simulation as forward model, a finite-difference simulator was used. Again, we'll show how the streamline-based generalized travel time inversion appears to be a viable means for conditioning high resolution geologic models to production data.

3.3. Field Applications in History Matching Using Finite-Difference Simulation

In this section, we discuss the application of streamline-based automatic history matching to an offshore turbiditic reservoir. We demonstrate that automatic history matching for conditioning static geologic models to production data is applicable to real data sets and complex reservoir models, and carries real business value. The specific implementation of the inversion method used in the present contribution:

- Uses a commercial (FD) simulator as forward model.
- Utilize liquid rates and water breakthrough times as input data and is well suited for waterfloods such as the field considered here.
- Inverts absolute permeabilities and no other model parameters.
- Performs streamline tracing and sensitivity calculations following a rigorous formulation, which can handle highly non-orthogonal cells and non-standard connections.

The coupling of a commercial (FD) simulator to the streamline-based inversion engine combines the efficiency of the streamline-based sensitivity computations, with the versatility and accuracy of a full-physics finite-difference model. In this way, limitations introduced into streamline simulation models are avoided, and we converge to the next local minimum in the objective function of the full-physics simulation (FD) model.

3.3.1. Overview: Offshore Turbitic Oil Field

The field under consideration here is located offshore in water depths of 400 to 800m. Three partially connected Eocene deep-marine reservoirs (organized in sheet and channel sands, see **Fig. 3.29**) at a depth of approximately 3000 m contain an estimated 500 MMSTB of oil at pressures of 4000 psi at the time production started. No reliable pressure data were collected subsequently, and field management relied on the observation of well productivity and, after several years of production, water was observed in several wells.

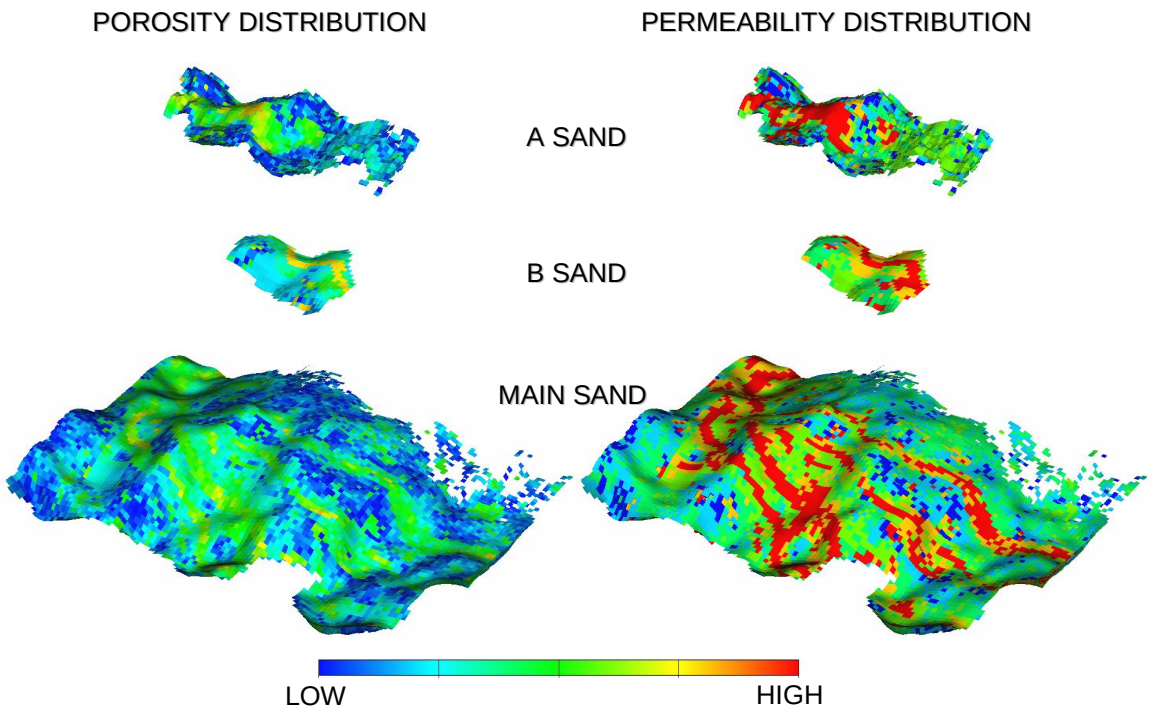

Fig. 3.29– Porosity and permeability distribution for offshore turbitic reservoir.

The field was initially produced under natural flow conditions (primary depletion) from 2 wells for 6 years (≈30 MMSTB). It was then completely shut in and redeveloped (waterflood) with 6 new producers and 4 water injectors, all drilled and brought on production over a time frame of 3 years. After redevelopment, another 3 years of production history (≈32 MMSTB) were available for history matching. Several normal faults span the field, and fault transmissibilities and permeability are the main uncertainties. The quality of the producing sands is excellent, with thicknesses up to 70 m, porosities ranging from 20 to 35%, and permeabilities up to 10 Darcy. The net-to-gross ratios of the reservoir sands are between 45% and 98 %, and stacking of high and low permeability sands is pronounced. The high-quality sands were identified in structure and position from seismic inversion and imported into the static reservoir model. Stochastic modeling was used to distribute high-permeability channels throughout the model, and both single and bimodal porosity-permeability relationships were used in defining the permeability values for the grid cells. A K_v/K_h ratio of 0.01 was applied, this

might be considered a slightly high value for heterogeneous turbidities such as those found in the model, but the thin layering of the simulation model makes it a lower effective value than when used in thicker layered models.

The simulation model was initialized with 10 different saturation regions as shown in **Fig. 3.30**. The fluids saturation distribution shows different oil-water contacts defined in all reservoirs. The distribution follows the partial connection between **A** and **MAIN Sand**, and the full connection between **B** and **MAIN Sand**. Such structural complexity must be successfully addressed while generating streamlines.

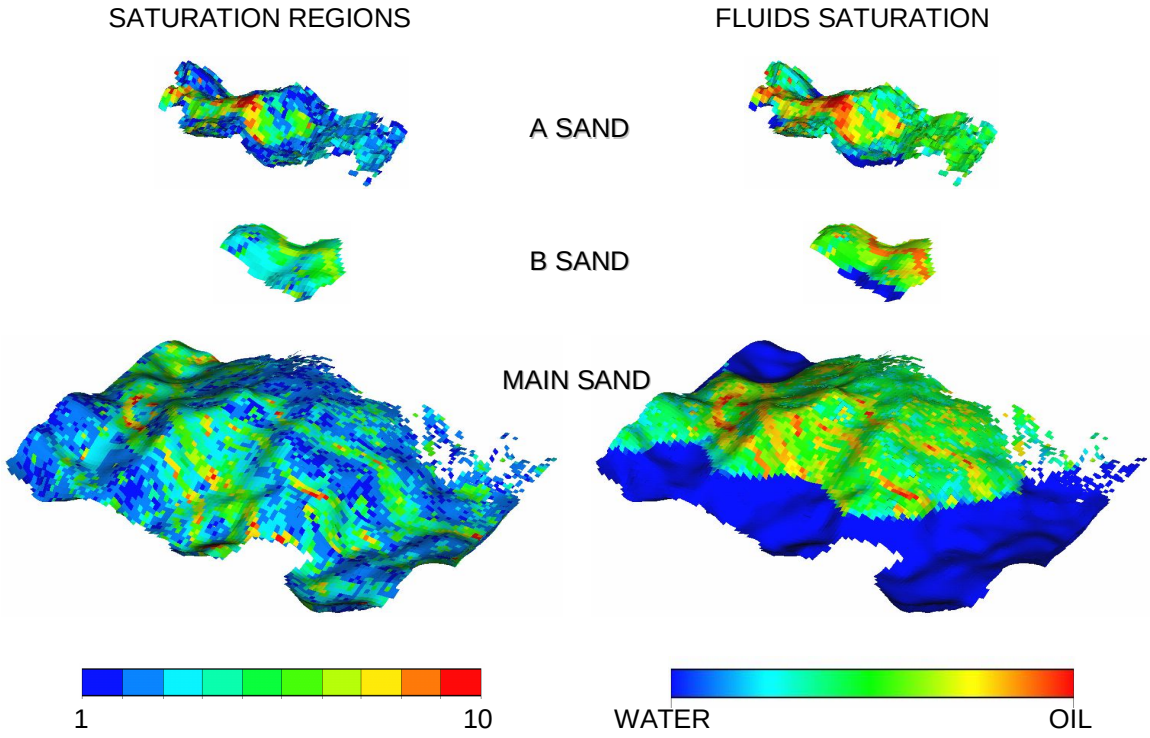

Fig. 3.30– Saturation regions and distribution for offshore turbitic reservoir.

The initial water cut match at all wells is presented in **Fig. 3.31**. Wells **1** and **4** show a delay in the simulated water cut. After the inversion is completed, it's likely to see an increase in permeability in order to accelerate the water fronts in these wells. Wells **5**, **6** and **7** show small water cut quantities, regardless of their magnitude, this data is still used in the inversion exercise. Wells **2** and **3** show no water cut data at all,

however to further constrain the inversion; these two wells were constantly monitored and included in the sensitivities and data misfit calculation.

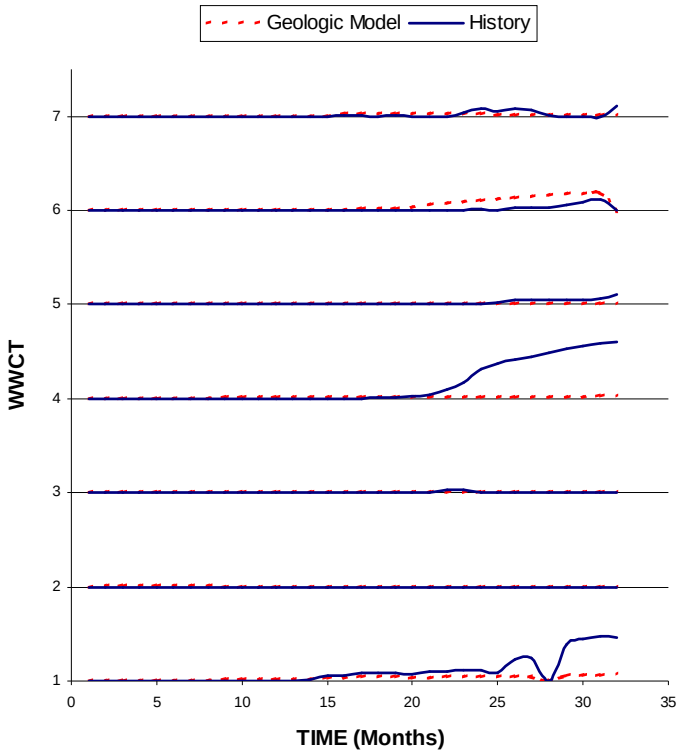

Fig. 3.31– Well water cut performance for initial geologic model.

History matching was carried out using a highly detailed initial geologic model consisting of more than 850,000 grid cells (200,000 of which are active cells). The initial geologic model was first manually history matched using rectangular-shaped areas of permeability multipliers. This technique is known to carry the risk of distorting the existing geologic model. Such undesirable impact is illustrated in **Fig. 3.32**. In **Sand A** several non-pay cells are converted to pay cells, which can lead to and overestimation of reserves and production in this sand. Both **Sand B** and the **Main Sand** show an obliteration of the channel structures identified using seismic data, and the geologic realism of the model is negatively affected. This is a clear example how parameter multiplier trial/error procedures, are extremely inefficient and endanger the realism and reliability of the geologic model.

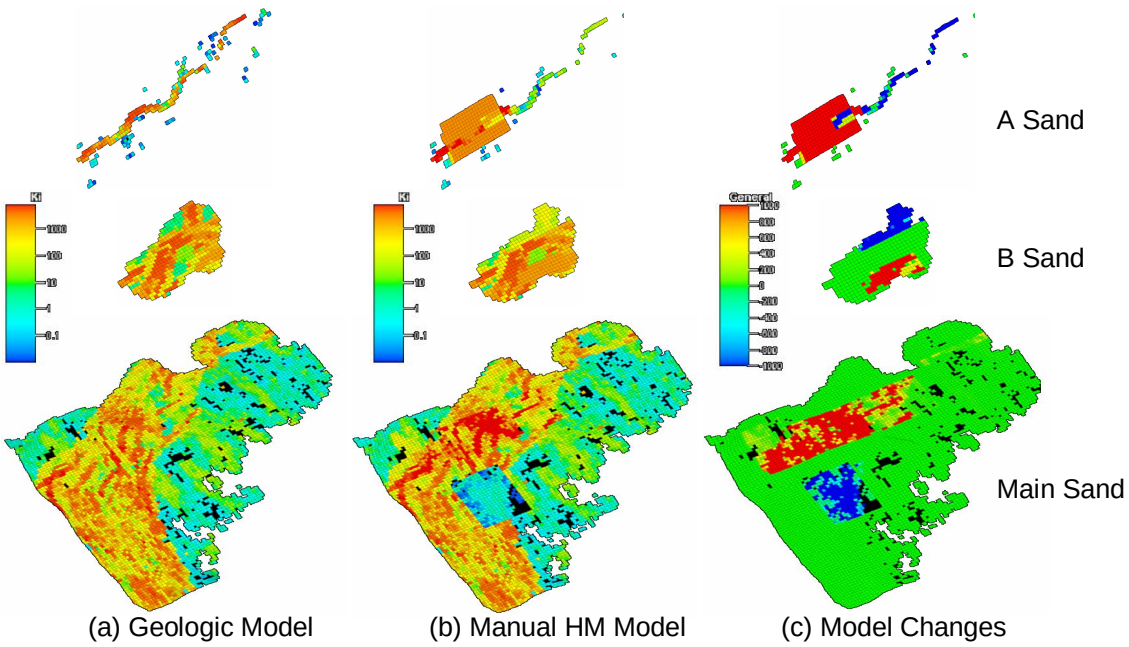

Fig. 3.32– (a) Initial permeability distribution. (b) Multiplier-contaminated permeability distribution. (c) Permeability difference, clean vs. contaminated permeability model.

3.3.2. Inversion Approach and Results

Automatic history matching using streamline-based inversion was carried out using the same initial geologic model. Note that the reservoir grid has multiple non-neighbor connections and pinch-outs, features that are often not correctly handled by conventional tracing algorithms. Such features were effectively addressed using the novel tracing algorithms discussed in the previous chapter. **Fig. 3.33** shows the streamline trajectories for two different field development stages: **Fig. 3.33(a)** represents the time of primary depletion by two wells. The pattern of streamlines shows the flow from the aquifer and from some cells with high potential towards the production wells. **Fig. 3.33(b)** shows the streamline flow pattern after the water injection program commenced. The flow now takes place primarily between water injector wells and producers. A barrier dividing the reservoir into two parts that communicate poorly is clearly visible.

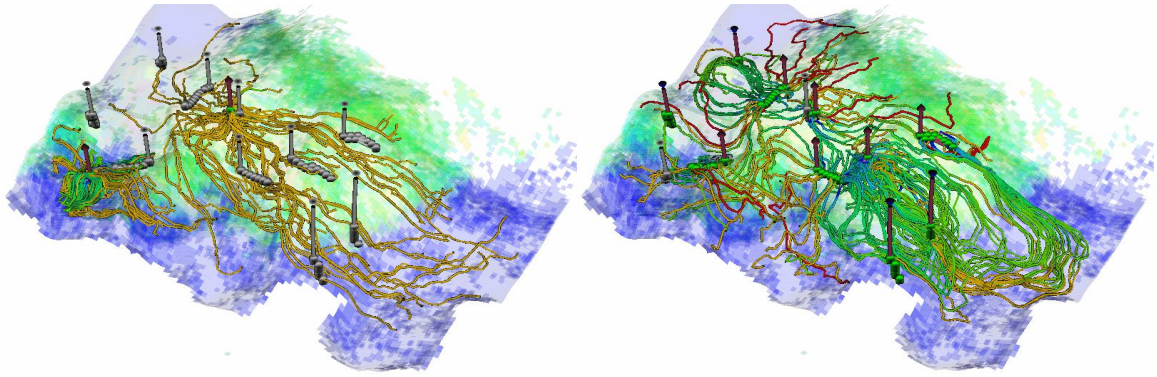

(a) Streamlines under primary depletion (b) Streamlines under waterflooding

Fig. 3.33– Streamline trajectories generated with numerical velocity field from (FD) simulator: (a) Streamlines under primary depletion, (b) Streamlines under waterflooding. All wells are shown in both graphs for illustration purposes.

After 6-7 iterations of the loop shown in **Fig. 3.2** a suitable history matching was obtained. Within each iteration, the numerical velocity field generation using (FD) took only 30 min of CPU time on a state-of-the-art desktop PC. The computational effort to perform the streamline tracing and compute the streamline-derived sensitivities was negligible for this particular application when compared with the flow simulation itself. The whole inversion exercise took around 5 hours of computing time, leading to a significant saving in time and man power.

The post-inversion history match for all wells is shown in **Fig. 3.34(a)**. Note the substantial improvement in the water-cut match for the problem wells **1**, **4** and **6**, while the good match at the other wells is maintained. **Fig. 3.34(b)** shows both the shift-time and water-cut misfit reduction. The inversion reduces the travel-time misfit by 80% within the first 2 iterations and the water-cut misfit was reduced to less than 50% of the original misfit.

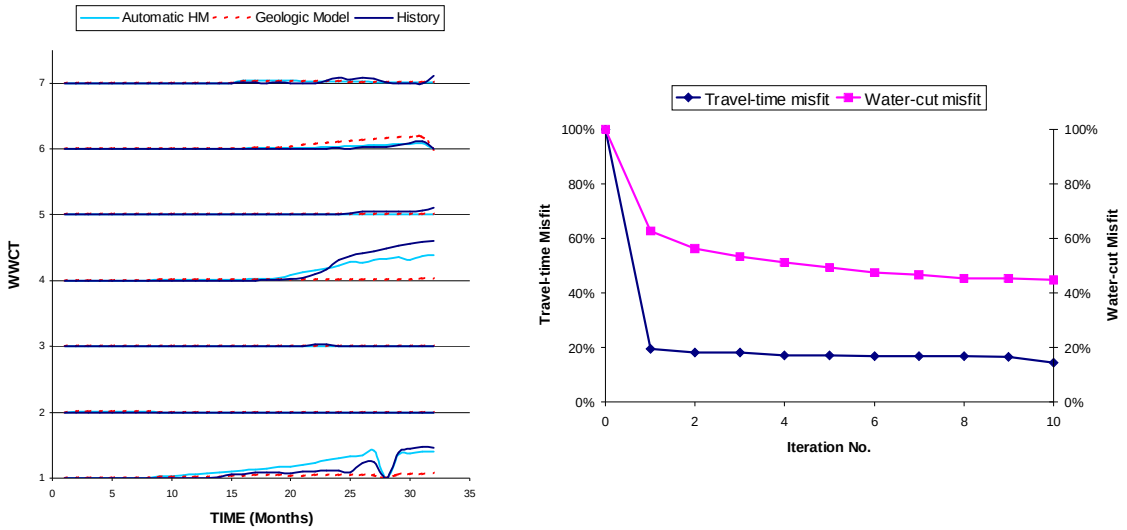

(a) Water cut history **(b) Misfit reduction**

Fig. 3.34– (a) Water cut match before and after streamline-based automatic history matching (b) Water cut and shift time reduction for production response by automatic history matching.

3.3.3. Impact in Prior Geologic Model

Fig. 3.35 shows typical changes in the permeability distribution induced by the inversion procedure in all three sands. **Figs. 3.35(a)** and **3.35(b)** show the initial and reconciled geologic model. The changes maintain geologic realism and are not "random" or geometrically regular in nature (**Fig. 3.35(c)**). They are localized along the conductive channels, as defined by the streamline flow domain decoupling. Qualitatively, the changes are consistent with the insights obtained from the manual history match. Permeabilities can change by several Darcy, all without user intervention, in a geologically realistic fashion, and in a time frame of few hours (as opposed to several weeks used in manual history matching).

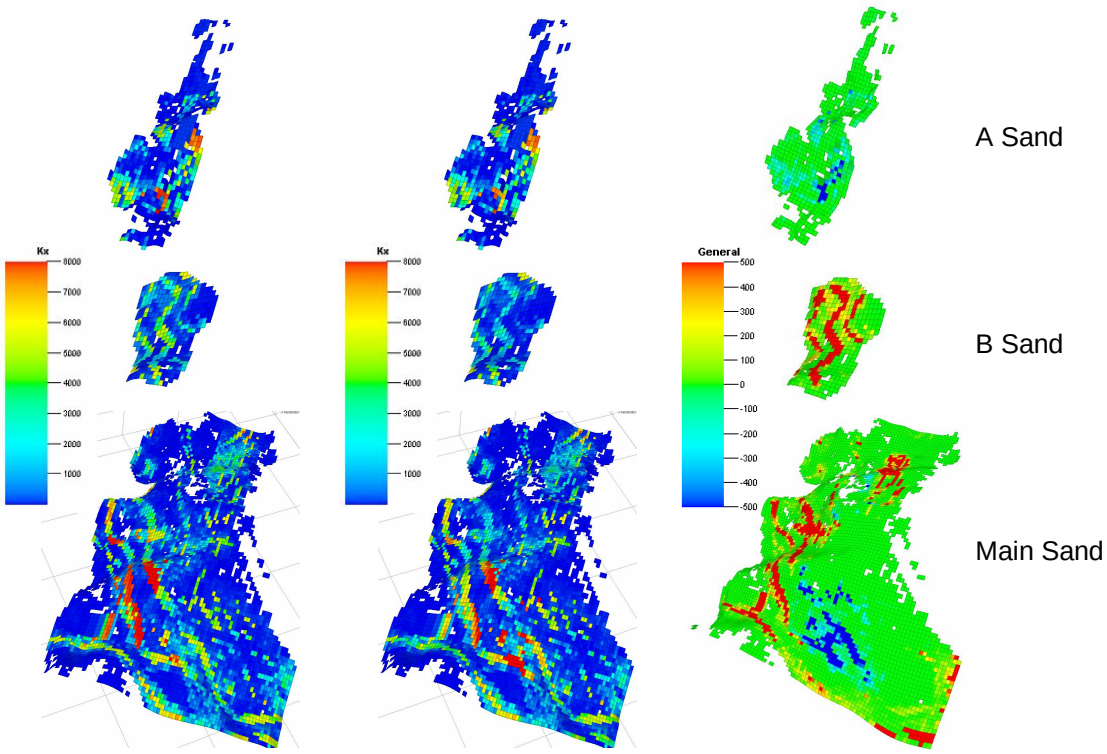

(a) Geologic Model (b) HM Model (c) Model Changes

Fig. 3.35– Permeability distribution in the 3 sand reservoirs, initial geologic model (left) and history matched model (center). The difference between final and initial permeability is shown in the right graph. Note that the color scale on the permeability difference (bottom) ranges from –500 mD to + 500 mD. The changes imposed by the inversion algorithm follow the geologic features of the reservoir (channels) and are not "random".

As we did with the giant middle-eastern field, we have also used the concept of vertical proportion curves (VPC) to further validate the inversion changes to the geologic model. **Fig. 3.36** shows typical layers of the facies model and the corresponding facies and permeability VPC. The facies VPC is quite intuitive; each reservoir represents a different depositional environment, dominated by the presence of a particular lithology. **A Sand** has a thin channel dominating the whole section; **B Sand** does not have any shale content and has the highest proportion of the high quality lithology. Finally the **Main Sand** features major channels with very good rock quality. The permeability VPC is somewhat different; unlike lithology, permeability is a continuous variable, and the colors indicate the proportion of cells occurring within a particular range. Note the high

proportion of cells with permeabilities greater than 1 Darcy and how they're present through the whole stratrigraphic column.

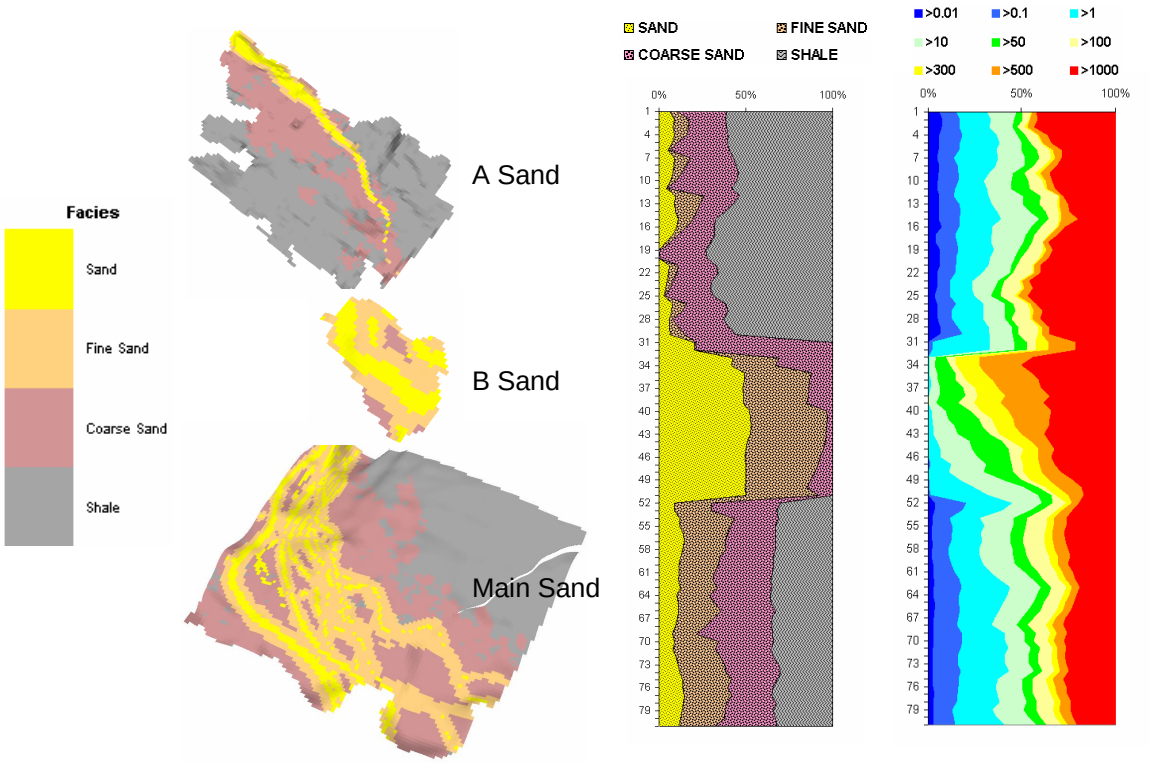

a) Facies Model (b) VPC Facies (c) VPC Permeability

Fig. 3.36– (a) Facies model used for evaluating impact of streamline-based inversion over geologic model. (b) Vertical proportion curve for facies. (c) Vertical proportion curve for initial permeability distribution. Vertical axis in (b) and (c) is layer number in model.

VPC diagrams are useful tools to locate where the changes are occurring and to which lithology they are associated with. To examine the impact on each lithology, its corresponding permeability was extracted and a VPC was constructed. For each lithology, the history matched and initial permeability VPC were subtracted and used to locate the inversion changes. **Fig. 3.37** shows the VPC changes for two different facies. A positive value represents an increase in the number of cells with a particular proportion, while a negative value represents a proportion reduction. Note that these values are weighted with the number of grid cells in a particular sand, i.e. permeability changes in

the drainage area of one well will lead to smaller VPC changes in the large **Main Sand** than in the smaller **B Sand**. The sand facies in figure **Fig. 3.37(a)** is a good example. It shows the largest change in the **B Sand** (layers 32-52), where the overall permeability has increased. This increase is associated with an accelerated water breakthrough in well **4** and is confined to the high quality facie. On the other hand, as expected for geologic reasons, **Fig. 3.37(b)** shows minimal or no change to the coarse sand proportions. It is encouraging to see the inversion preserve the overall permeability proportions for those facies that are not likely to change, but also allow change for those facies which are geologically expected to be modified.

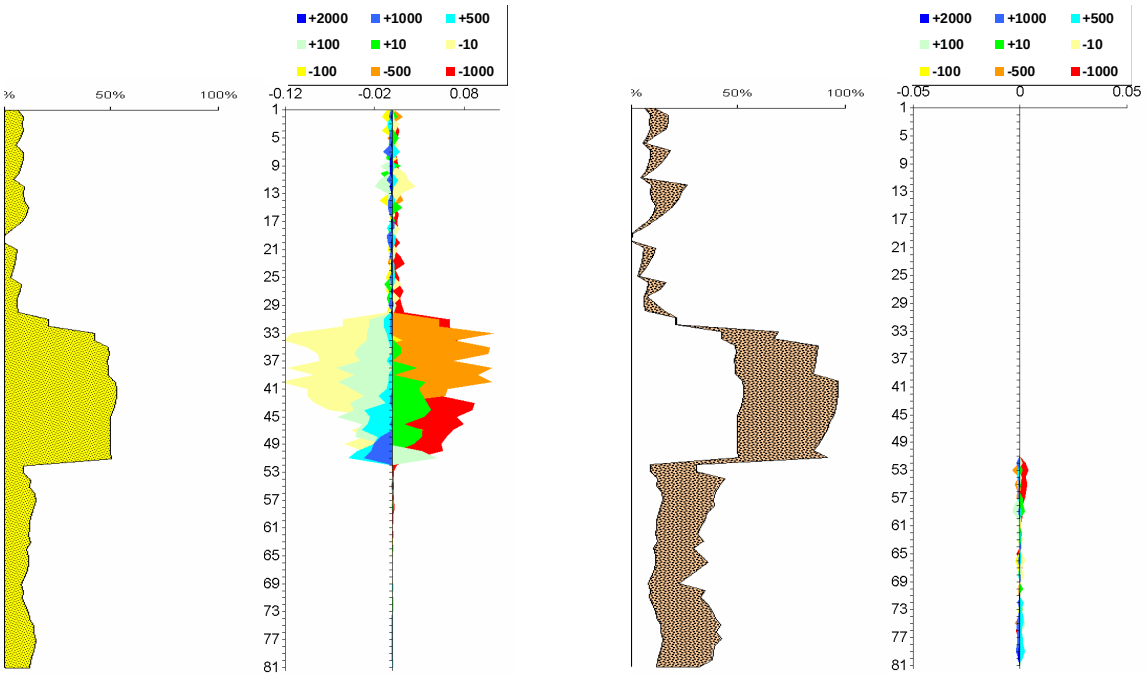

(a) Sand Facie (b) Coarse Sand

Fig. 3.37– Impact of streamline-based inversion in geologic model (a) Proportion changes to sand facies (b) Proportion changes to coarse sand facie.

CHAPTER IV

TIME-LAPSE SEISMIC DATA INTEGRATION USING STREAMLINE-BASED SENSITIVITIES

In the previous chapter we discussed how reconciling high-resolution geologic models to multiphase production history ("history matching") is one of the most time-consuming aspects of the workflow for geoscientists and engineers. "History matching" typically uses well-based measurements and is therefore severely limited in the lateral reservoir model resolution. We present a history matching approach that can use information from high-resolution seismic data to supplement the areally sparse production data. Our approach utilizes streamline-derived sensitivities to perform the history match as parameter optimization in multi-dimensional space at a fraction of the time required for manual history matching. The method can be applied using either finite-difference or streamline models.

In the approach presented here, the seismic data are not used directly but in the form of fluid saturation and pressure maps derived either by traditional interpretation or by seismic inversion. These maps provide a separate set of constraints in addition to the production data. An elegant and efficient gradient-based multi-parameter optimization can be performed because the derivatives of both the production data and the fluid saturations/pressures with respect to the permeabilities are calculated using a streamline formulation for the fluid flow. The essential ideas underlying this approach are similar to those used for high-frequency approximations in seismic wave propagation. In both cases, this leads to solutions that are defined along "streamlines" (fluid flow), or "rays" (seismic wave propagation). Specifically, a finite-difference or streamline flow model is used to generate velocity fields from which we compute streamlines and multi-parameter sensitivity coefficients, including those related to the saturation constraint maps.

Synthetic and field-scale data examples are presented to demonstrate that interpreted or inverted seismic data provides a large amount of additional information for history matching. Our example leads us to the conclusion that the problem of non-uniqueness in this complex inverse problem is greatly reduced when constraints in the form of saturation maps from spatially closely sampled seismic data are included. A schematic workflow for joint seismic-production data history matching based on streamline inversion functionality is presented.

4.1. Mathematical Background

Similar to what we did with the 'generalized travel time' (GTT) inversion workflow, there're 4 major steps involved in the seismic integration: (1) a forward model used to represent reservoir fluid flow and properly generate streamline trajectories (2) establishing a misfit function between observed and simulated responses for both production and time-lapse seismic data, (3) defining production and seismic sensitivity coefficients to relate the simulator performance to the geologic model and (4) the minimization of the production and seismic objective function which will define a model with a suitable history match.

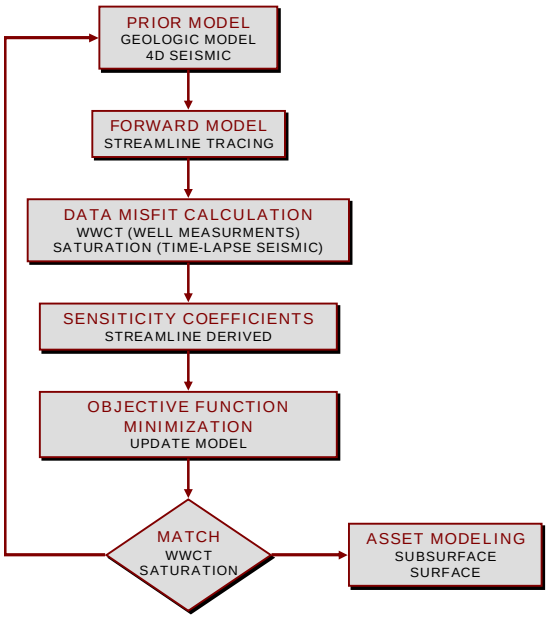

Fig. 4.1– Streamline-based production and seismic joint integration workflow.

We now outline the mathematical background behind this approach which is summarized in **Fig. 4.1**

4.1.1. Streamline based Sensitivity Computations

There are several advantages associated with our trajectory-based approach. The most important one is that we obtain an analytic expression for the traveltime (τ) of the front along the streamline trajectory Ψ,

$$\tau = \int_{\psi} s(x) dr \tag{4.1}$$

Where s is the slowness defined as the reciprocal of the interstitial velocity,

$$s = \frac{1}{|v|} = \frac{\phi}{k\lambda_{rt}|\nabla P|} \tag{4.2}$$

In **Eq. 4.1** we have an expression for the traveltime along a trajectory Ψ in terms of fluid properties (λ_{rt}), reservoir flow properties (k), and the pressure distribution (∇P). This expression can be interpreted in terms of the physical processes at play in multiphase flow. By transforming the flow problem into characteristic coordinates (coordinates oriented with respect to the trajectories) we obtain a semi-analytic expression for the saturation history at a point on the trajectory,

$$S_w(t,\tau) = S\left(\frac{\tau}{t}\right) \tag{4.3}$$

The sensitivities required to solve the inverse problem follow from the form of the solution defined along the trajectories. Specifically, in order to better fit the observations, we must relate perturbations in the model parameters (reservoir flow parameters) to perturbations in the observations (seismic saturations observations). Since the flow

properties enter the sensitivities through the time of flight definition, we can consider a perturbation in this quantity. A perturbation in τ is related to a perturbation in saturation δS_w by[23],

$$\delta S_w\left(\frac{\tau}{t}\right)=\frac{1}{t}S_w^{'}\left(\frac{\tau}{t}\right)\delta\tau \tag{4.4}$$

Where the prime denotes differentiation with respect to the argument τ/t. The quantity $\delta\tau$ follows from a perturbation of the integral in **Eq. 4.1.**

$$\delta\tau=\int_{\psi}\delta s(x)dr \tag{4.5}$$

For a total mobility λ_{rt} which does not change significantly, the slowness is a composite response and its variation can be related to changes in reservoir properties as follows,

$$\delta s(x)=\frac{\delta s(x)}{\delta\phi}\delta\phi(x)+\frac{\delta s(x)}{\delta k}\delta k(x) \tag{4.6}$$

Where the partial derivatives are,

$$\begin{aligned}\frac{\partial s(x)}{\partial k}&=\frac{-\phi(x)}{\lambda_{rt}k^2(x)|\nabla P|}=-\frac{s(x)}{k(x)}\\ \frac{\partial s(x)}{\partial \phi}&=\frac{1}{\lambda_{rt}k(x)|\nabla P|}=\frac{s(x)}{\phi(x)}\end{aligned} \tag{4.7}$$

The time of flight sensitivities can be obtained analytically in terms of simple integrals along streamlines. For example, the time of flight sensitivity with respect to permeability will be given by,

$$\frac{\partial \tau}{\partial k(x)} = \int_{\psi} \frac{\partial s(x)}{\partial k(x)} dx = -\int_{\psi} \frac{s(x)}{k(x)} dx \tag{4.8}$$

Where the integrals are evaluated along the streamline trajectory. Just as we did for the production data integration, the quantities in the sensitivity expressions are either contained in the initial reservoir model or are produced by a single simulation run.

4.1.2. Production and Seismic Data Misfit

As we did while integrating production data; after running the forward model and generating adequate streamlines, the next step is the quantification of the data misfit. This will be done at two different levels: (1) a well level using water cut data and (2) a seismic level using the time-lapse datasets. In the GTT approach, at each well an optimal time-shift Δt was defined in order to minimize the production data misfit at the well. This is illustrated in **Fig. 3.3** where the calculated water-cut response is systematically shifted in small time increments towards the observed response and the data misfit is computed for each time increment. On the seismic level, we'll use the saturation maps at different times to further constrain the inversion procedure. This additional information will remove the drawbacks arising from the low resolution of production data and will improve the quality of the reservoir model.

Single Time-lapse Seismic Misfit. The main objective of time-lapse seismic data is to determine the changes occurring in the reservoir as a result of hydrocarbon production or injection of water or gas into the reservoir by comparing repeated datasets. A typical final processing product is saturation maps at the survey times. We could use the difference between the seismically derived and simulated saturations to define our misfit function. **Fig. 4.2** shows a simulated and seismic saturation dataset for a synthetic 9-spot heterogeneous model and its corresponding difference attribute. Note that for this particular example there's a significant difference between the observed saturation map and the one obtained after running the simulator.

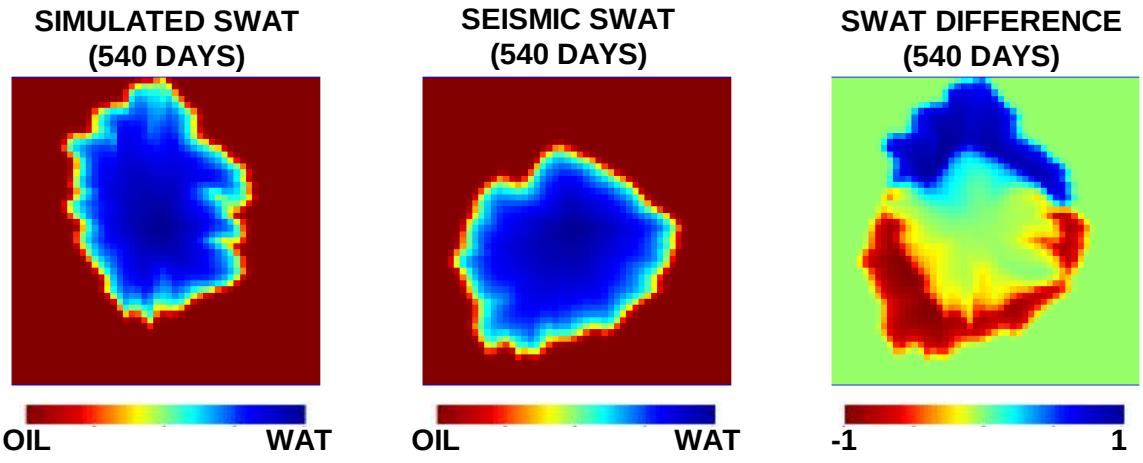

(a) *(b)* *(c)*

Fig. 4.2– Synthetic water saturation maps at specific time (a) derived from reservoir simulation (b) derived from 4D seismic and (c) saturation difference.

Any cell showing a non-zero saturation difference will be considered as a potential observation point to be integrated during the seismic inversion. Please note that for every cell included in the inversion, a stream of sensitivities must be defined. Depending on the performance of the prior geologic model, the number of cells to be integrated can lead to very large sensitivity matrix. This number can be reduced by applying cut-off values to remove small saturation differences and focus in those zones with large differences. **Fig. 4.3** shows several misfit attributes for different cut-off values.

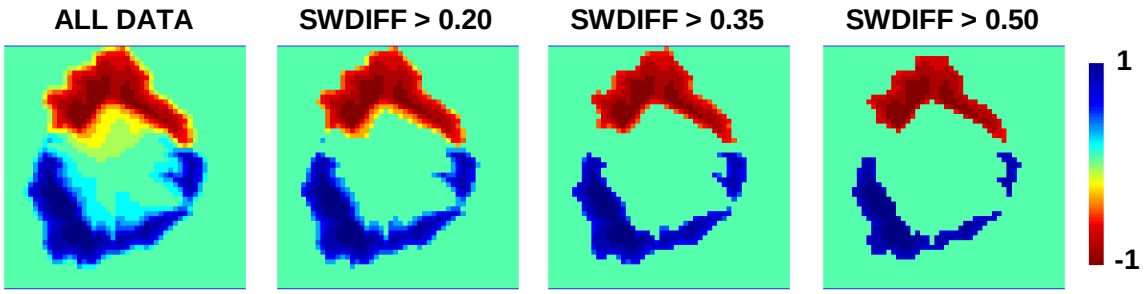

Fig. 4.3– Misfit attributes between seismic and simulated saturation for several cut-offs values. The number of observed points to be integrated can be significantly reduced based on cut-offs applied to misfit attribute.

4.1.3. Time-Lapse Seismic Sensitivity Coefficients

We have already mentioned the unique advantages of streamline-assisted inversion to compute the sensitivity of the simulator output with respect to reservoir parameters such as porosity and permeability. In Chapter III, it was presented how water cut sensitivities via 'generalized travel time' (GTT) were calculated. The sensitivities were derived to minimize the misfit function arising when calculating the GTT. Following the same philosophy, we'll now present seismic sensitivities for the single time-lapse misfit dataset.

Sensitivities to Single Time-lapse Seismic Dataset. The involved calculations will be carried out only considering a specific seismic survey with its equivalent simulated response. After choosing a proper cut-off value to remove small saturation differences (**Fig. 4.3**), we'll only include sensitivities from those cells with a significant deviation from the observed water saturation. Every *i*-streamline sweeping selected *j*-cells will be contributing to the cell sensitivity in the following form,

$$\frac{\partial S_{w,j}}{\partial m} = -\sum_{i=1}^{Nsl} \left(\partial S_{wi,j} / \partial m \right) \tag{4.9}$$

This expression reduces to the sensitivity estimation of the water saturation at each cell, $\partial S_{wi,j} / \partial m$. Remember that in **Eq. 4.3** we defined a perturbation in saturation δS_w with respect to the argument τ / t based on the semi-analytic solution for the saturation history. Applying a chain rule, these sensitivities can be obtained in terms of the sensitivities of the streamline time of flight,

$$\frac{\partial S_{wi,j}}{\partial m} = \frac{1}{t} \frac{\partial S_{wi,j}\left(\frac{\tau}{t}\right)}{\partial \tau} \cdot \frac{\partial \tau}{\partial m} \tag{4.10}$$

The time-of-flight sensitivity $\partial\tau/\partial m$ is again obtained analytically in terms of simple integrals over the paths ψ^t. These sensitivities were already calculated when defining the water cut sensitivities and will be reused here. Note that when there is no significant variation in reservoir pressure during the time interval between the seismic surveys, the trajectories will be virtually identical. Even under significant pressure changes this would be an appropriate approximation considering that we're attempting to integrate dynamic data rather than predicting fluid flow performance. The sensitivity of the water saturation with respect to the time-of-flight, $\partial S_{wi,j}\left(\frac{\tau}{t}\right)/\partial\tau$, can be numerically estimated along the streamline trajectory. Note that the sensitivities are only approximates because the self-similar solution apply under restrictive assumptions of uniform initial saturation distribution. However, our experience indicates that these approximate sensitivities are adequate for inversion purposes.

4.1.4. Production and Seismic Data Joint Integration

In Chapter III we followed a deterministic approach in which the production data integration started from a prior static model already incorporating geologic, well log, and seismic data. If only production water cut data were to be included in the minimization, the following penalized misfit function was used,

$$\left\|\delta d - G\delta R\right\| + \beta_1\left\|\delta R\right\| + \beta_2\left\|L\,\delta R\right\| \tag{4.11}$$

Where $\delta\mathbf{d}$ is the vector of generalized travel-time shift at all wells, i.e. the difference between the observed and simulated production response. **G** is the sensitivity matrix containing the sensitivities of the generalized travel time with respect to reservoir parameters. Also, $\delta\mathbf{R}$ correspond to the change in the reservoir property and **L** is a second spatial difference operator that is a measure of roughness. Finally the weights $\beta 1$ and $\beta 2$ determine the relative strengths of the prior model and the roughness term. The minimum was obtained by an iterative least-square solution of the augmented linear system,

$$\begin{pmatrix} G \\ \beta_1 I \\ \beta_2 L \end{pmatrix} \delta R = \begin{pmatrix} \delta d \\ 0 \\ 0 \end{pmatrix} \tag{4.12}$$

Since we'll introduce a new set of sensitivities, the penalized misfit function is redefined as,

$$\left\| \delta d - G\delta R \right\| + \left\| \delta S_s - S\delta R \right\| + \beta_1 \left\| \delta R \right\| + \beta_2 \left\| L\delta R \right\| \tag{4.13}$$

In this new system, **S** is the sensitivity of the time-lapse seismic response with respect to reservoir parameters. These sensitivities are defined following the single time-lapse difference formulation (**Eq. 4.10**). $\delta\mathbf{S_s}$ represents the corresponding misfit vector (**Fig. 4.3**). This will lead to a new augmented linear system (large but presumably sparse, **Eq. 4.14**) which can be handled with the same least-square minimization algorithm used while integrating production data.

$$\begin{pmatrix} G \\ S \\ \beta_1 I \\ \beta_2 L \end{pmatrix} \delta R = \begin{pmatrix} \delta d \\ \delta S_s \\ 0 \\ 0 \end{pmatrix} \tag{4.14}$$

4.2. Production and Time-Lapse Seismic Data Integration: An Illustration

In this section, we'll illustrate the application of streamline simulation techniques to production and time-lapse seismic data integration with a synthetic model. We'll start by integrating only production water cut data, and comparing the simulated saturation performance with a given reference saturation representing the time-lapse seismic data. We'll then present results for joint inversion when integrating the time-lapse datasets via seismic sensitivities. Our results show a great deal of improvement in the performance of

the reservoir model when information available in saturation maps from spatially closely sampled seismic data is included.

4.2.1. Production Integration: Synthetic Example

The synthetic case involves two-phase flow and includes matching water-cut and water saturation from a heterogeneous 9-spot pattern. The prior permeability model and initial water-cut simulation responses are plotted together with the observed data in **Fig. 4.4**. It can clearly be seen how all wells present significant discrepancies between observed and simulated responses.

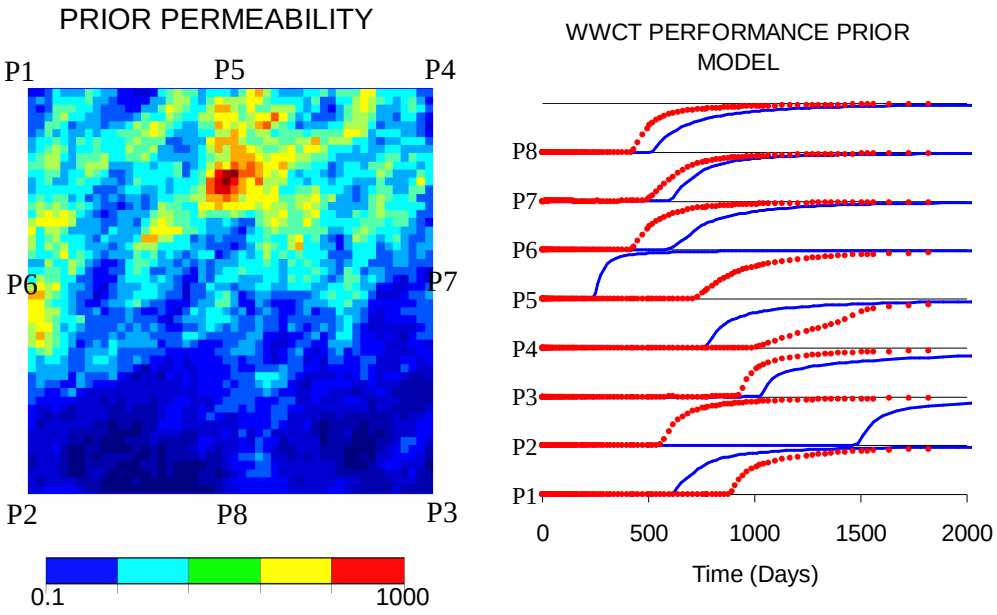

Fig. 4.4– Permeability distribution and water cut match performance for 9-spot synthetic prior model.

The performance of the prior model is also evaluated in terms of the water saturation since observed saturations are assumed to be available. **Fig. 4.5** shows the seismic saturation distribution along streamlines for two different survey times and the corresponding simulated saturation. Note the tremendous disparity at both survey times and how the water fronts are misrepresented by the prior model.

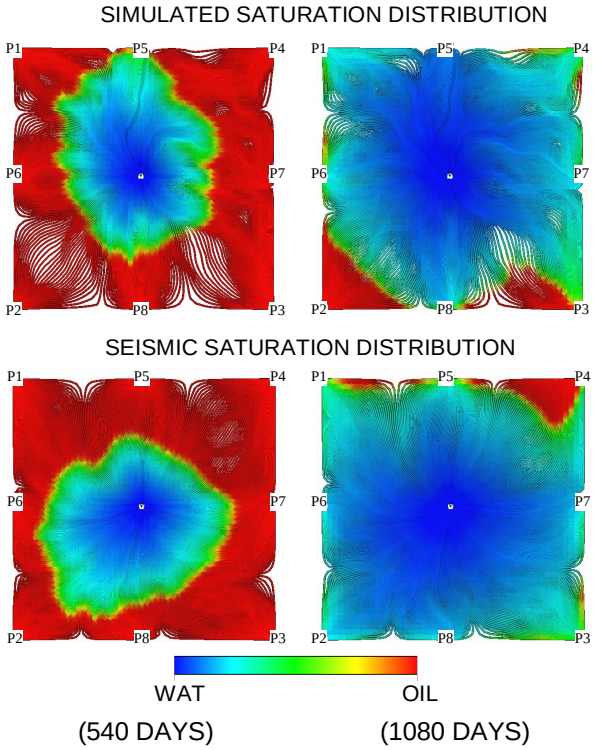

Fig. 4.5– Prior model water saturation response and seismic saturation distribution for two different survey times.

Let's examine what would happen when integrating only production water cut data. **Fig. 4.6** shows the simulated water cut responses before and after applying the GTT inversion. As expected, all wells showed a noteworthy improvement in the water cut history match and in general terms, if time-lapse seismic data is not available, the updated model would satisfy all requirements to move on to prediction. Would this be the case if 4D seismic data is available? Are the displacements fronts properly reproduced when only integrating production? Can we improve and reduce the non-uniqueness of the production history matching process? To answer these questions, let's compare the simulated saturation responses with seismic saturations after integrating production via GTT inversion, as shown in **Fig. 4.7**.

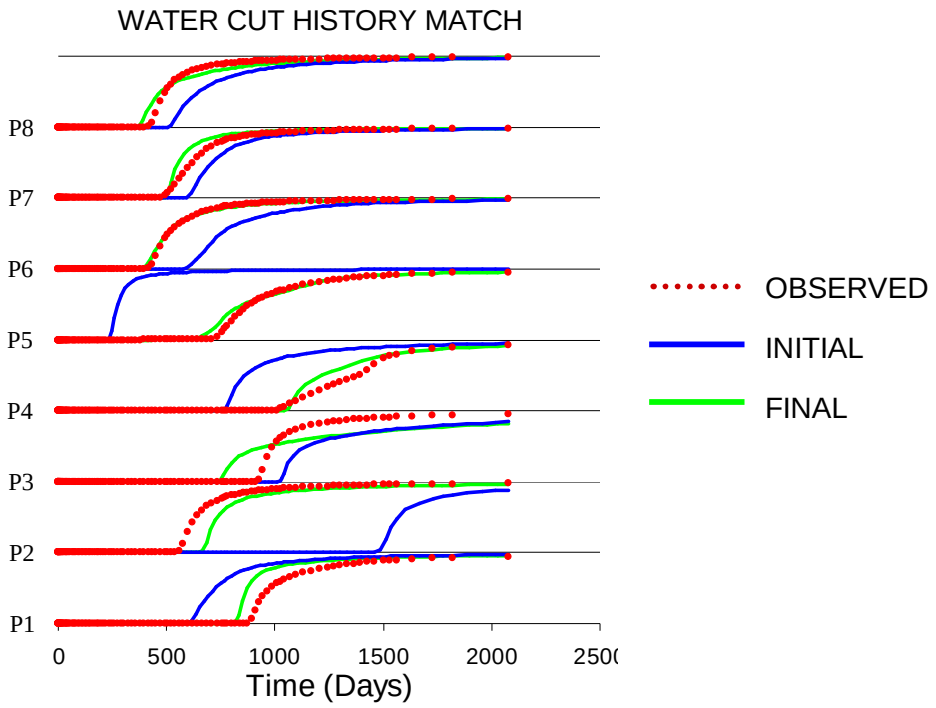

Fig. 4.6 − Water cut history match after running generalized travel time inversion.

The GTT inversion is delaying and accelerating the water fronts based on the observed production data at well locations. Let's consider front displacement for producer **P5**; the prior model (**Fig. 4.4** and **Fig. 4.5**) shows an early water cut and an extensive flooded area for the first survey time. According to observed production and the seismic datasets this well should present the complete opposite performance. After running the GTT inversion a suitable production match was obtained. However, the saturation fronts are not completely appropriate; the GTT inversion is severely limited in the lateral reservoir model resolution, because only production data is considered. A poorer situation occurs at producer **P3**, where the seismic map for the second survey time shows a nicely flooded area in contrast to the scarcely flooded area obtained after integrating production.

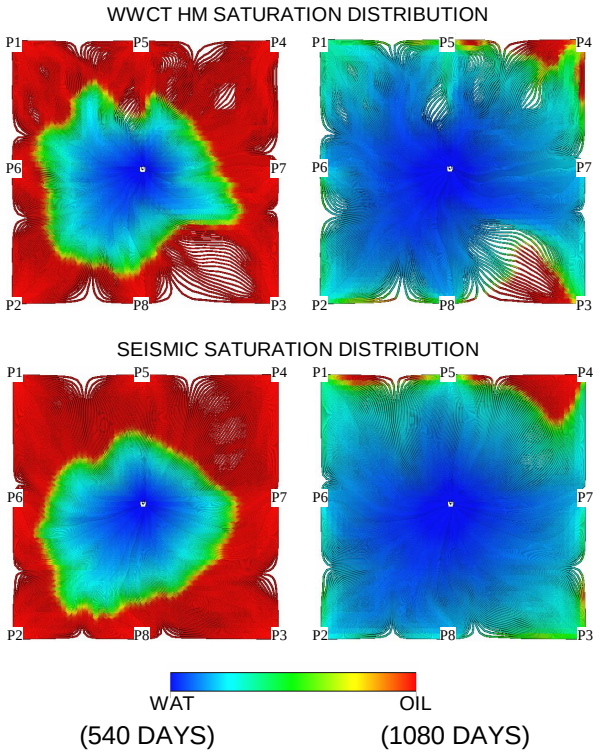

Fig. 4.7– Water saturation response after running generalized travel time inversion. Seismic datasets are provided for comparison purposes.

4.2.2. Production and Single Time-Lapse Seismic Integration

We've seen how integrating production data is not enough to fully reproduce the displacement fronts occurring far away from the cells. Our solution will be to supplement the areally sparse production data with seismic datasets. We'll present results when considering only one seismic dataset at a time; the sensitivities will be based on the derivations following the single time-lapse seismic misfit at the corresponding survey time (as shown in **Eq. 4.10)**. Since only one seismic map is considered in this approach, running additional iterations will be required to fully integrate all seismic datasets.

After running the forward model and generating streamlines, the next step in our joint inversion workflow is establishing the misfit function for both production and seismic data. The production misfit is taken care of via GTT and the seismic misfit is defined by the difference between the time-lapse seismic and simulated saturation. After

defining the misfit, production sensitivities are calculated at each well and seismic sensitivities are calculated for all cells showing sizeable differences in the single time-lapse seismic misfit attribute. **Fig. 4.8** shows a summary of the misfit functions and sensitivities for both production and seismic data for the first survey at 540 days.

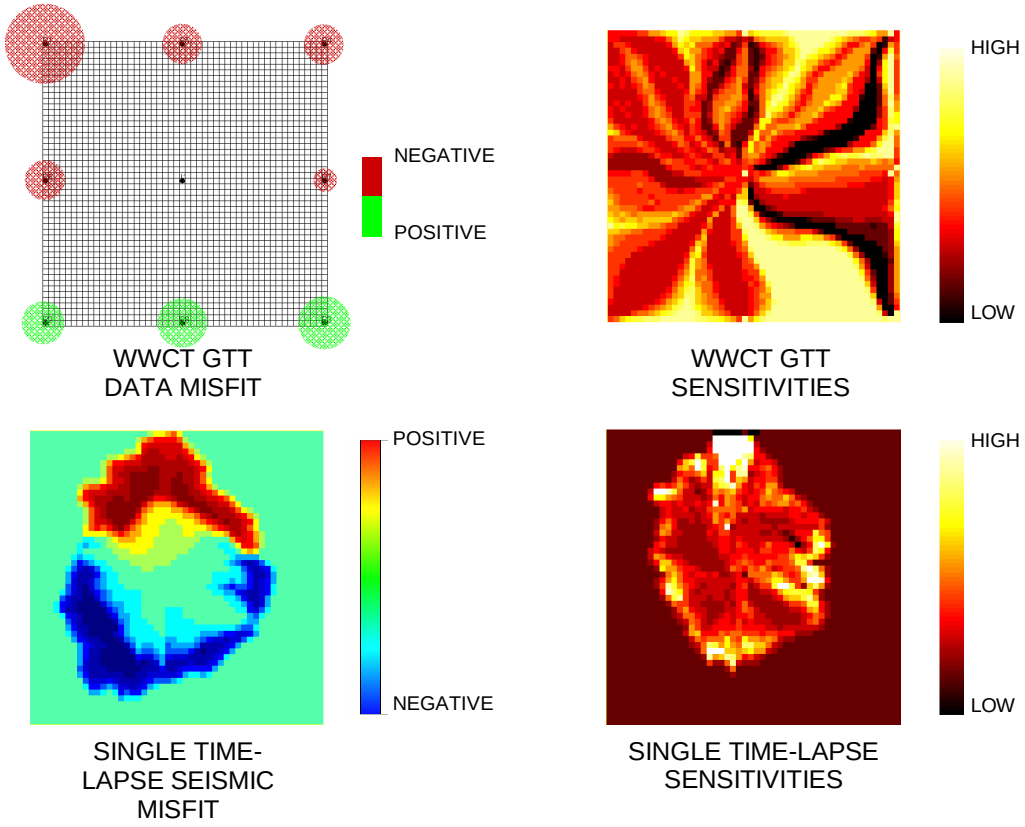

Fig. 4.8–Misfit functions and streamline-based sensitivities for production and seismic data.

For this specific example, we'll first integrate the saturation map at 540 days. The integration is done jointly with the production water-cut data and the model update is done after minimizing the penalized production-seismic misfit function (**Eq. 4.13**). A very successful production (**Fig. 4.9**) and saturation (**Fig. 4.10**) match was obtained after only 7 iterations (9 minutes of computing time in a Dell Dimension XPS). A first impression at the production history match shows that we're not only preserving but also improving its quality when compared to the inversion results after integrating only production data.

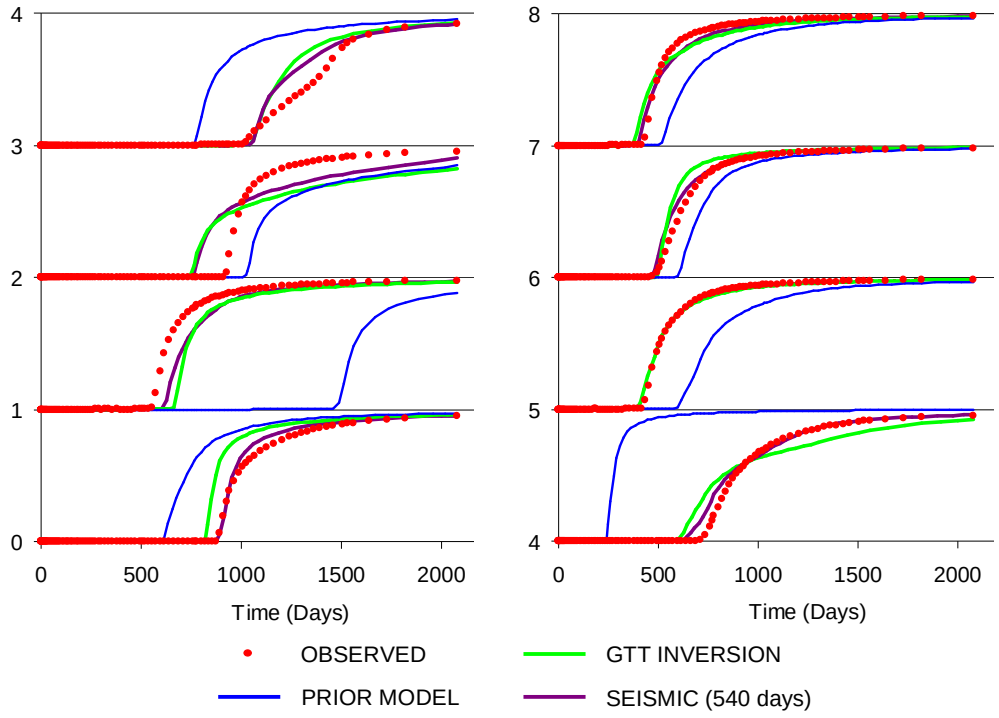

Fig. 4.9– Water cut history match for production and seismic (540 days) joint integration.

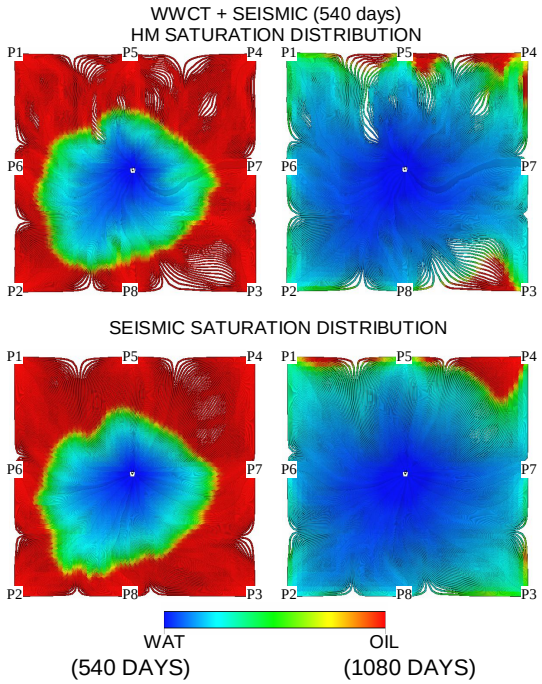

Fig. 4.10– Water saturation response after running GTT and integrating single time-lapse seismic dataset at 540 days.

Let's inspect the results a little bit more while considering producers **P1** and **P3**. For producer **P1** the prior model was providing an early water breakthrough, because of a prematurely flooded area as shown in **Fig. 4.5**. After integrating only production, a significant delay in the breakthrough was achieved but still a noteworthy water cut travel time misfit was present. Regardless of the production delay the displacement front was still a little bit premature when compared to the seismic survey at 540 days (**Fig. 4.7)**. After integrating production and the seismic dataset at 540 days, the water cut match was substantially improved and best of all; the simulated saturation matched almost perfectly the observed saturation (**Fig. 4.10**). Producer **P3** illustrates a different situation; the prior model showed a late water breakthrough as a result of poorly flooded areas and, the simulated response at 1080 days showed a high oil saturation zone far from what is observed on the seismic dataset. After integrating production data, an earlier water breakthrough was achieved, but little was accomplished in obtaining an adequate displacement front. This downside in the overall inversion remained latent even after integrating the seismic data set at 540 days. This is a limitation in our method since we're only integrating a single time-lapse seismic dataset at a time and a second full blown inversion will be required to fully integrate the seismic survey at 1080 days. The starting point would be a new model already integrated with production data and the first time-lapse seismic dataset.

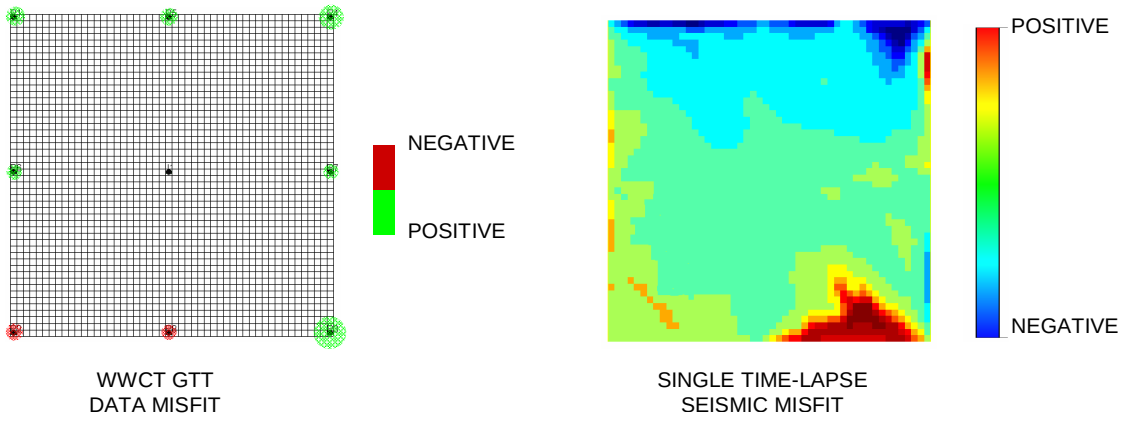

Fig. 4.11−Production and seismic misfit after integrating time-lapse seismic dataset at 1080 days.

Fig. 4.11 shows the production and seismic misfit for the new starting model. The water cut travel time misfit in all wells, excepting producer P3, is around ±30 days. This new seismic misfit function accounts for the undesirable flooded areas surrounding producers **P3** and **P4.** Results for both production water-cut and saturation match are presented in **Fig. 4.12** and **Fig. 4.13**.

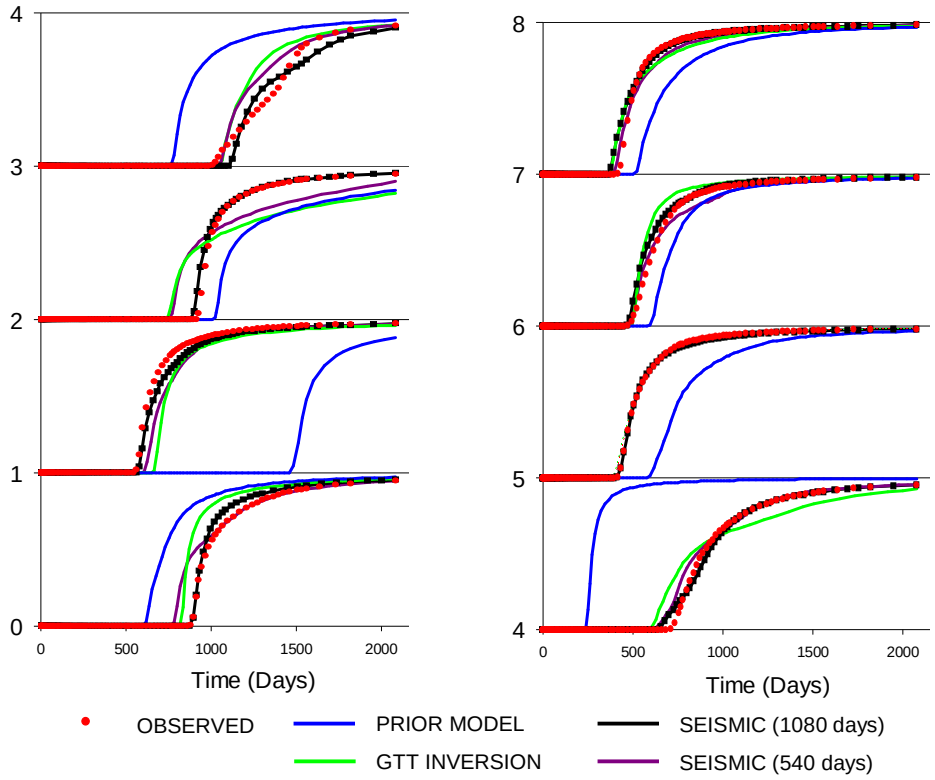

Fig. 4.12– Water cut history match for production and seismic (1080 days) joint integration.

Once again the overall water cut performance was improved and the travel time misfit problems with producer **P3** were effectively removed. This is further verified by comparing the displacement fronts in **Fig. 4.13,** where the simulated saturation response at 1080 days is almost identical to its counterpart seismic dataset. Note that the saturation match for the first seismic dataset was retained and could be further improved by imposing constraints while minimizing the production-seismic misfit function.

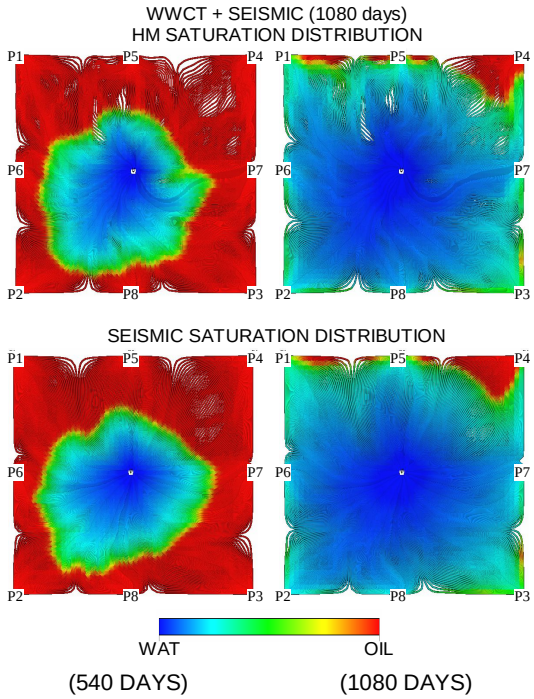

Fig. 4.13– Water saturation response after running GTT and integrating single time-lapse seismic dataset at 1080 days.

4.3. Field-Scale Application

In this section the feasibility of the proposed methodology will be demonstrated for field studies by application to a large-scale 3-D example. As mentioned before, streamlines and time of flight are used to compute the sensitivity of the production and seismic data with respect to reservoir parameters as described in the mathematical formulation section. In this field example, water cut and time-lapse seismic data were matched jointly to update the reservoir permeability model.

4.3.1. Model Description

The three-phase model consists of 5 producers and 2 injectors scattered in a 15x25x11 block centered geometry grid. The initial permeability and porosity are shown in **Figs. 4.14(a)-(b)**. High permeability streaks are localized in the upper layers creating streamline clustering as shown in **Fig. 4.24(c)**. A time of flight threshold of 10,000 days

was applied in order to ease the streamline visualization and understand the prior model displacement front behavior. The prior model water cut performance is presented in **Fig. 4.15**; it can be seen how all wells show poor matches characterized by late breakthrough times.

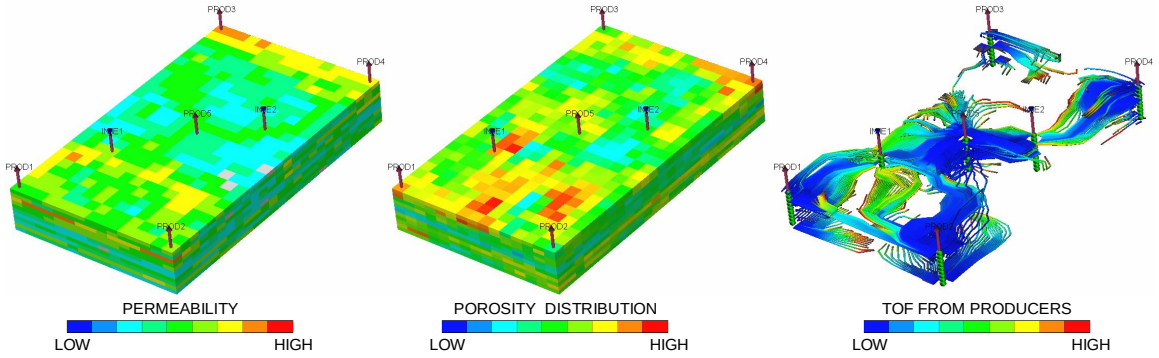

(a) *(b)* *(c)*

Fig. 4.14– (a) Permeability distribution, (b) Porosity distribution and (c) streamline trajectories displaying time of flight from producers for field-scale problem.

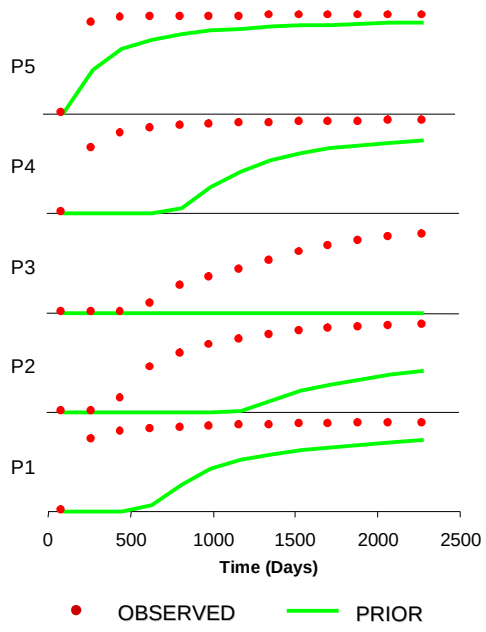

Fig. 4.15–Production water cut performance of prior model.

A time-lapse seismic dataset is available at 480 days and was compared to its equivalent simulated water saturation response (**Fig. 4.16)**.

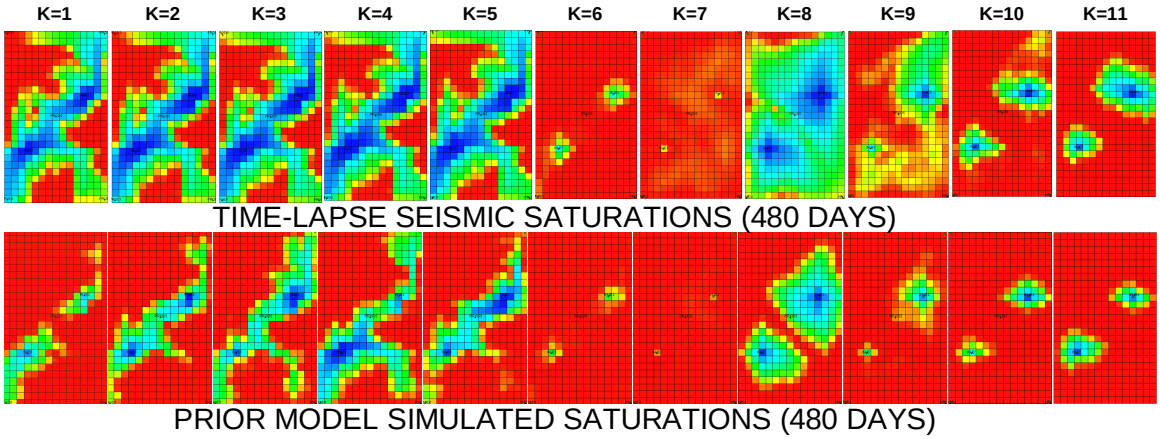

Fig. 4.16– Time-lapse seismic dataset and equivalent simulated water saturation response at 480 days.

The seismic saturations are showing large water volumes breaking through in several layers with completed cells. The simulated water front is barely advancing in all layers and the waterflood sweeping efficiency is hardly represented by the prior model. For example, let's consider producer **P3** where no water cut is reported by simulation and, from the streamline trajectories (**Fig. 4.14(c)),** it'd take more than 10,000 days for this well to see water from the closest injector **I2**. The simulated saturation maps show that not a single layer where this well is completed is seeing water. A similar situation occurs in the rest of the wells where, as a consequence of an inadequate water displacement modeling, late water cuts are observed.

4.3.2. Production Data Integration

In this section results will be presented after integrating only production data via GTT inversion. **Fig. 4.17(a)** shows the water cut history match; as expected the entire production history was successfully integrated and water cuts are fully reproduced by the updated model. **Fig. 4.17(b)** shows the objective function behavior where the original travel time and amplitude misfit was reduced by several orders of magnitude. The

simulated saturations after the GTT inversion are compared with the prior model and time-lapse seismic saturations in **Fig. 4.18**.

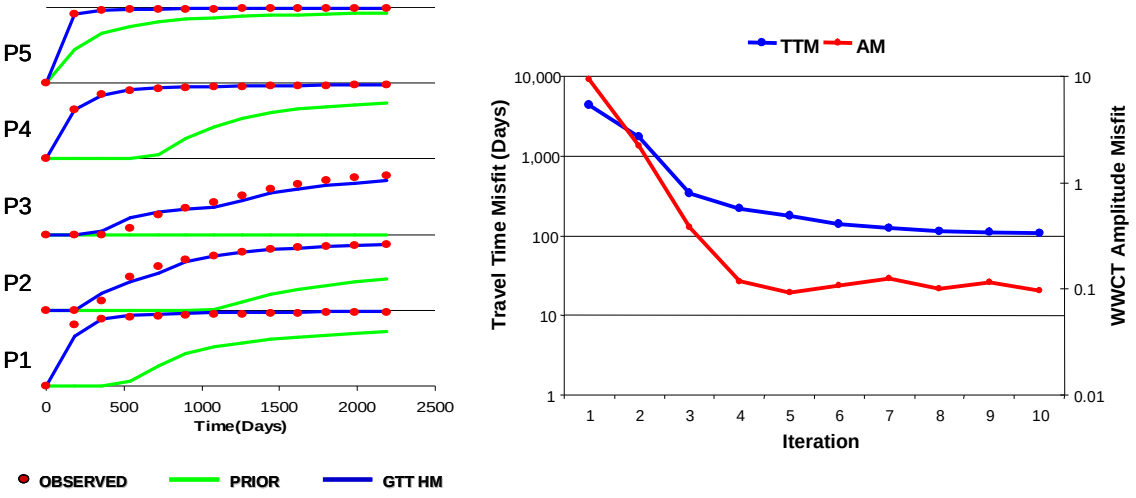

(a) *(b)*

Fig. 4.17– (a) Water cut history match after running GTT inversion and (b) objective function behavior through GTT iterations.

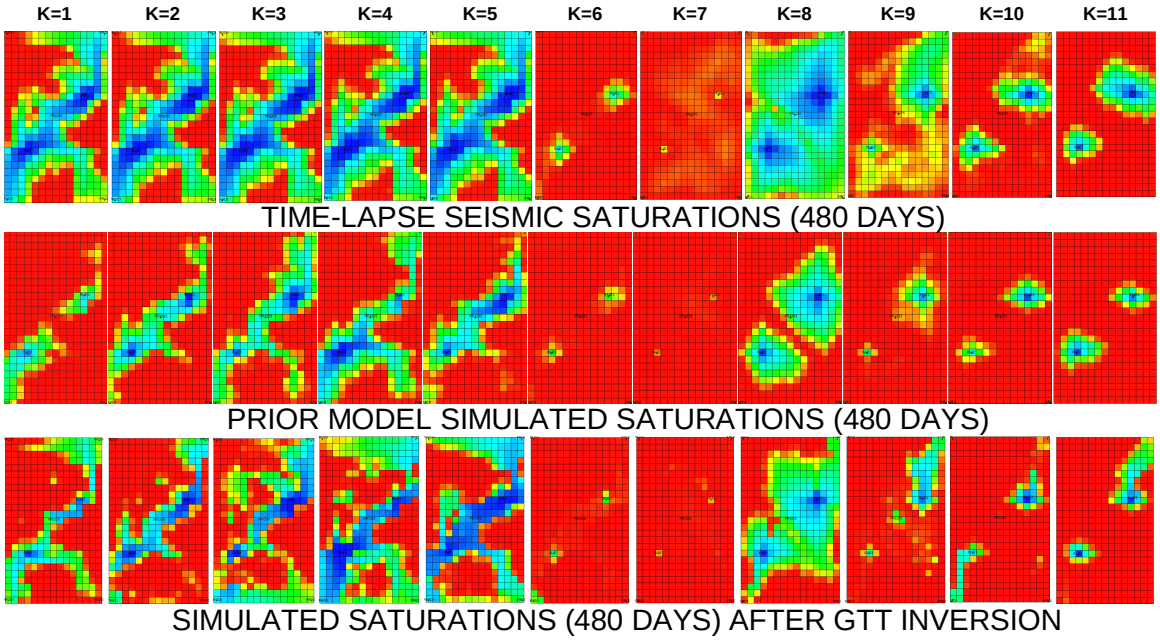

Fig. 4.18–Saturation maps at 480 days for: time-lapse seismic dataset, prior model and, updated model after GTT inversion.

The resemblance to what is observed on the seismic dataset was considerably improved after integrating production data. The breakthrough times were effectively accelerated and the injected water is sweeping the model with a closer similarity to the referenced saturation. However, the model still suffers some downsides in the upper and bottom layers, where the water fronts are not entirely well represented. This is a direct consequence of production data having low spatial resolution and its limited areal coverage in large-scale dynamic data integration problems.

4.3.3. Production and Time-Lapse Seismic Joint Integration

So far we have shown evidence that integrating only production data is severely limited to reproduce the overall fluid displacement development under field-scale conditions. We present an efficient history matching approach that can use information from high-resolution seismic data to supplement the areally sparse production data. For this particular case, acceptable results were obtained after 6 iterations (40 minutes of computing time). The production water cut match is presented in **Fig. 4.19**; note how the GTT inversion results were slightly improved as consequence of additional constraints available via time-lapse seismic integration.

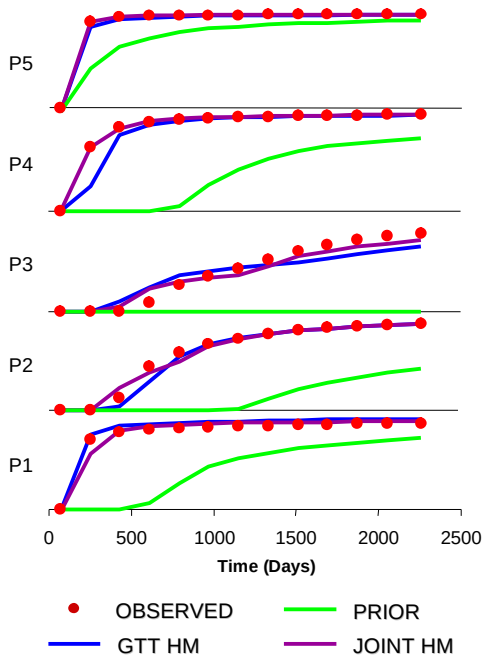

Fig. 4.19−Water cut history match after joint production and seismic inversion.

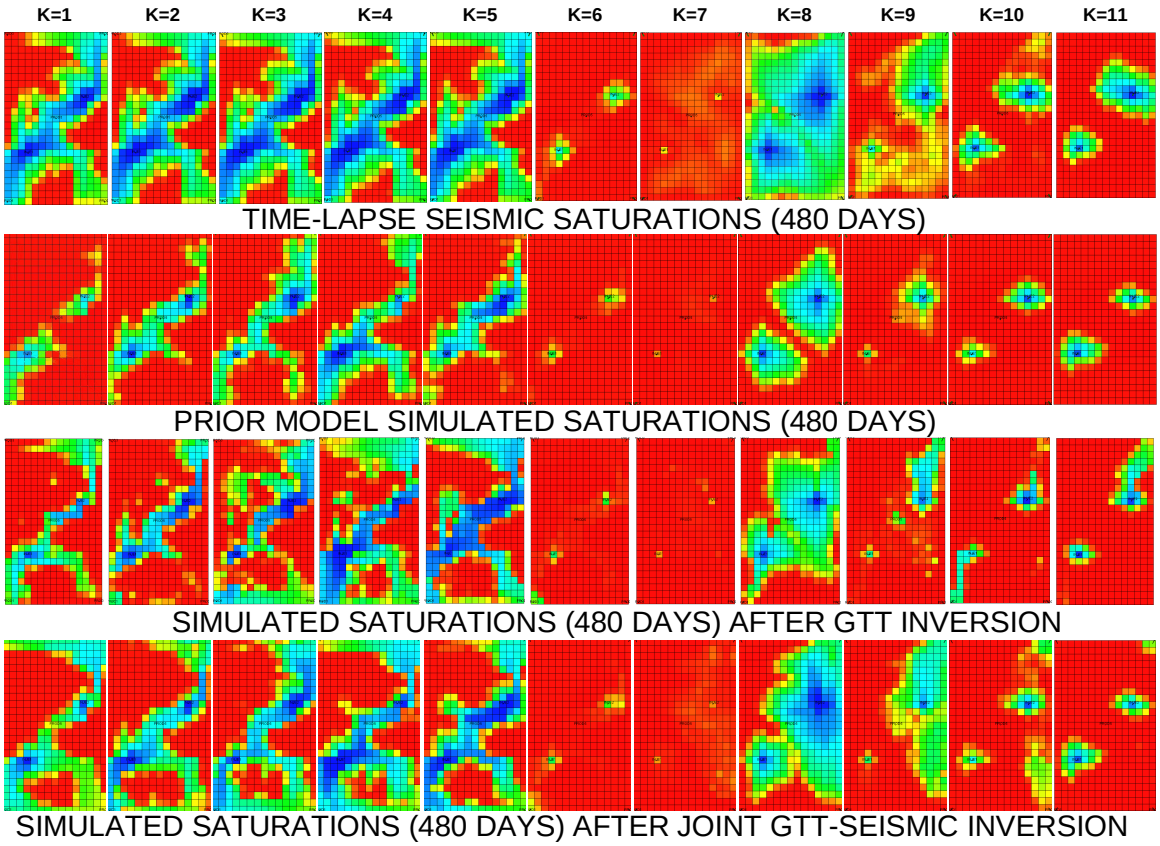

Fig. 4.20 −Saturation maps at 480 days for: time-lapse seismic dataset, prior model, GTT updated model and, updated model via joint production-seismic inversion.

Finally, the simulated saturation response after the joint production-seismic inversion is presented in **Fig. 4.20**. The overall water displacement is now in very close agreement to what is observed on the seismic datasets. After having an updated model honoring water saturation distribution and flooded areas, the final step would be to examine the impact of production and seismic data integration on the permeability distribution. **Fig 4.21** compares the histograms of the initial and final permeability fields; the shape of the distribution has essentially remained unchanged except for the appearance of high permeability values. The occurrence of these high values is because dynamic data integration has resulted in flow channels and preferential flow paths with higher permeabilities, which was a geologic feature unaccounted by the prior model.

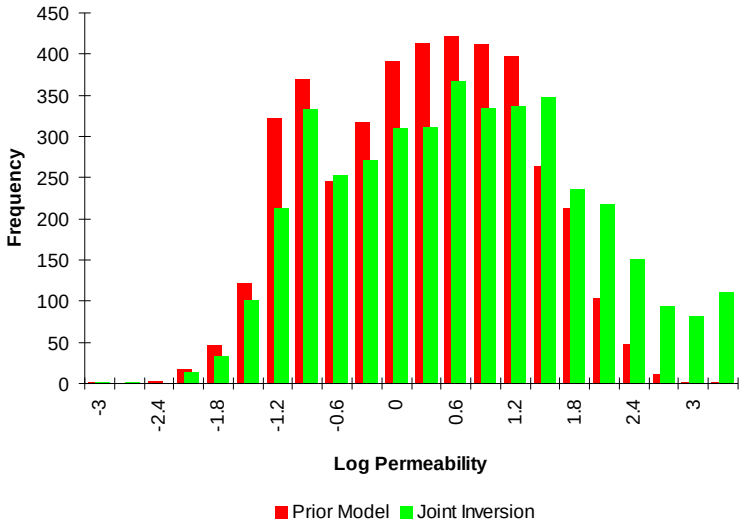

Fig. 4.21 −Permeability histograms before and after joint inversion.

CHAPTER V

CONCLUDING REMARKS AND RECOMMENDATIONS

Reconciling geologic models to dynamic data only considering well-based measurements can lead to unreliable parameter estimates because of limited reservoir areal coverage. We have successfully developed an efficient joint inversion scheme where time-lapse seismic datasets are used to supplement areally sparse production data. Our approach relies on the unique advantages available through streamline-based integration techniques. Specifically we use streamline-derived sensitivities to relate both production and seismic data responses to the model parameters. Our approach is well-suited for high-resolution models as we're able to carry out production-seismic joint integration in hours as opposed to weeks or month usually required by traditional workflows.

5.1. Conclusions

The major findings and concluding remarks of this research are summarized as follows,

Streamline Tracing. The local refinement construction is the simplest extension to three dimensions for faulted reservoir cells which provides consistency with the finite-difference flux calculation. Failure to conserve the underlying flow field will lead to serious discretization errors in streamline trajectories and the subsequent transport solutions. Extensive synthetic and field examples have been shown for a multiple pair of cells juxtaposed across a fault. A full calculation with multiple cell juxtapositions would be built up as a local grid of more than three layers. As the fault geometry gets more complex then the advantages of working with a boundary layer formulation becomes even more obvious; it will allow us to examine each cell face in isolation from other cell

faces and other cells. In two dimensions we can extend the ‘local’ region to entirely replace the faulted cells. This has the advantage of improved accuracy in the transit time calculation, although at the cost of a more highly vertically refined model. However, this construction cannot be implemented to three dimensions as easily as the local boundary layer formulation.

Production Data Integration. We have highlighted the unique features of streamline models that make them particularly well-suited for production data integration into high resolution geologic models. Streamline models can be used for ‘automatic’ history matching and also in conjunction with finite-difference models. The unique information content in streamline trajectories, the time of flight and the streamline-derived sensitivities, allow for targeted changes in the geologic model to match production history. The changes are constrained to the prior model and thus geologic continuity is preserved. The new tracing algorithm was interfaced with the concept of generalized travel time inversion. It was demonstrated how the method can be utilized to quickly identify the discrepancy between geologic models and field production data early in the geologic model development so as to minimize the time and effort needed for detailed history matching using finite-difference models.

Two challenging field applications were used to illustrate the versatility of the inversion scheme. The first one was a very successful application to a giant middle-east field using streamline simulation as forward model. The geologic model derived after conditioning to production responses was used to identify the distribution and orientation of dominant fractures and preferential flow paths in the reservoir. A systematic analysis using statistical moments and facies-based vertical proportions was carried out to examine the geologic realism of the updated permeability model. To our knowledge, this is the first application of inverse modeling for conditioning geologic models with more than a million parameters to field production history.

The second field application aimed to show how the combination of full-physics finite-difference simulation with streamline-based inversion is a powerful technique for

history matching realistic complex reservoirs. The new technique for tracing streamlines in highly non-orthogonal systems with non-neighbor connections presented in Chapter II was interfaced to a widely used commercial simulator. We demonstrated the generalized travel time inversion successfully on a waterflooded complex offshore turbiditic reservoir with a moderate number of wells and about 3 years of waterflooding history.

Seismic Data Integration. Joint history matching of production and seismic data offers tremendous potential for improving static/dynamic reservoir management workflows. Our approach is particularly well-suited for high resolution geologic models and allows us to carry out field-scale integration of 4-D seismic data in hours as opposed to days or months. The joint history matching can be carried out using either finite-difference or streamline models. In our approach, the seismic data are not used directly but in the form of fluid saturation and pressure maps derived either by traditional interpretation or by seismic inversion. These maps provide a separate set of constraints in addition to the production data. An elegant and efficient gradient-based multi-parameter optimization can be performed because the derivatives of both the production data and the fluid saturations/pressures with respect to the permeabilities in the underlying simulation model are calculated analytically as 1-D integrals along streamlines. The sensitivity computations require a single flow simulation leading to substantial savings in computation time.

5.2. Recommendations

Streamline Tracing Recommendations. The tracing algorithm should be extended to handle locally refined grids (LGR). The same concepts and constructions involved in the local boundary layer (LBL) approach are required for flux continuity at the boundary of a LGR within a streamline simulator. In detail, the boundary of a LGR will have the same juxtaposition issues as do faulted cells. As in this treatment, they can be modeled by extending the local grid by an additional cell into the root grid with boundary conditions chosen to ensure flux continuity.

It should also be considered implementing the tracing algorithm within unstructured geometries. The implementation should be focused into breaking the unstructured elements into corner point sub-elements to ease the transition between tracing functionalities. The challenge in this extension will be reconstructing the fluxes inside the unstructured sub-elements. After flux continuity is preserved the same tracing subroutines available in the object-oriented program could be easily extended to handle the unstructured geometries.

Production Data Integration Recommendations. Rigorous production integration should include water/oil ratio, gas/oil ratio and bottomhole pressures. The scope of this work only covered integrating production water cut. However, the software prototype could be easily upgraded to include gas/oil ratio and bottomhole pressure streamline-based sensitivities. New functionality could be interfaced with the already existing platform and a robust application could be available to integrate all types of production data.

The usefulness of the code could also be improved by interfacing it with additional finite-difference and streamline simulators. So far the software has been interfaced and successfully tested with the following FD and SLS simulators: FRONTSIM (Geoquest), ECLIPSE (Geoquest), VIP (Landmark) and MORES (Shell E&P). The application could be easily extended to the next generation of simulators, good candidates will be: NEXUS (Landmark-BP) and INTERSECT (Geoquest-Chevron)

Time-lapse Seismic Integration Recommendations. In general for inverse problems, there are concerns of non-uniqueness and uncertainty associated with permeability estimates based upon production and time-lapse observations. The efficiency of our approach and the semi-analytic expressions for model parameter sensitivities should help in this regard. There is also the issue of the dependence of the solution on the starting model. This question is difficult to address and emphasizes the fact that we should begin with the best possible prior representation derived from static modeling. However, we can again take advantage of the efficiency of the inversion

algorithm to explore the range of possible solutions. Specifically, we can conduct a number of inversions, starting from various plausible initial models and different seismic datasets and conduct a post-processing to join insights into the inherent uncertainty.

The scale of the time-lapse seismic measurements is another issue to consider. In this work we assumed the seismic resolution to be identical to the simulation grid. We recommend considering an optimal upgridding technique to define the grid geometry for coarse sensitivities and subsequent changes that can be used to update the fine resolution model. This multi-scale inversion scheme will act as an additional constraint in the objective function minimization since the inversion will implicitly focus on global trends rather than local changes.

Finally, we provide in Appendix A alternative formulations to carry out the seismic integration. The first one is considering time-lapse seismic difference datasets. An immediate advantage will be reducing the number of forward runs, as opposed to the implemented single time-lapse seismic approach. The second one is defining a ‘connective function’ that relates the seismic and simulated saturations at each streamline trajectory and treats them as signals. It’s strongly recommended to implement them and explore the overall performance and quality of the inversion schemes.

REFERENCES

1. Tarantola, H.: *Inverse Problem Theory: Methods for Data Fitting and Model Parameter Estimation*. Elsevier, Amsterdam, Netherlands (1987).

2. Li, R., Reynolds, A. C., and Oliver, D.S.: "History Matching of Three-Phase Flow Production Data," *SPE Journal* (December 2003) 328-340.

3. Sun N.-Z.: *Inverse Problem in Groundwater Modeling*. Kluwer Academic Publishers, Boston (1994).

4. Yeh, W. W.-G.: "Review of Parameter Identification Procedures in Groundwater Hydrology: The Inverse Problem," *Water Resources Research* (1986) **22**, No. 2, 95.

5. Landa, J.L. and Horne, R.N.: "A Procedure to Integrate Well Test Data, Reservoir Performance History and 4-D Seismic Information into a Reservoir Description," paper SPE 38653 presented at the 1997 SPE Annual Technical Conference and Exhibition, San Antonio, TX, 5-8 October.

6. Landa, J.L.: "Technique to Integrate Production and Static Data in a Self-Consistent Way," paper SPE 71597 presented at the 2001 SPE Annual Technical Conference and Exhibition, New Orleans, 30 September-3 October.

7. Wen, X.-H., Deutsch, C.V. and Cullick, A.S.: "High Resolution Reservoir Models Integrating Multiple-Well Production Data," *SPE Journal* (December 1998) 344-355.

8. Wen, X.-H, Deutsch, C.V. and. Cullick, A.S.: "A Review of Current Approaches to Integrate Flow Production Data in Geological Modeling," Report 10, Stanford Center for Reservoir Forecasting, Stanford, CA (1997).

9. Reynolds, A. C., Li, R., and Oliver, D.S.: "Simultaneous Estimation of Absolute and Relative Permeability by Automatic History Matching of Three-Phase Flow Production Data," *JCPT* (March 2004) **43**, No. 3, 37-45.

10. Bissel, R.C.: "Calculating Optimal Parameter for History Matching," Proc. of the 4th European Conference on the Mathematics of Oil Recovery, Topic E: History Match and Recovery Optimization, Røros, Norway (1994).

11. Oliver D.S., Reynolds, A.C., Bi, and Z., Abacioglu, Y.: "Integration of Production Data into Reservoir Models," *Petroleum Geoscience* (May 2001) 65-73.

12. Bissel, R.C., Killough, J.E., and Sharma, Y.: "Reservoir History Matching Using the Method of Gradients," paper SPE 24265 presented at the 1992 SPE European Petroleum Computer Conference, Stavanger, 25-27 May.

13. Luo, Y. and Schuster, G.T.: "Wave-Equation Traveltime Inversion," *Geophysics* (1991) **56,** No. 5, 645.

14. Kretz, V., Le Ravalec, M. and Roggero, F.: "An Integrated Reservoir Characterization Study Matching Production Data and 4D Seismic," paper SPE 77516, presented at the 2002 SPE Annual Technical Conference and Exhibition, San Antonio, Texas, 29 September-2 October, 2002.

15. Kretz, V., Valles, B. and Sonneland, L.: "Fluid Front History Matching Using 4D Seismic and Streamline Simulation," paper SPE 90136, presented at the 2004 SPE Annual Technical Conference and Exhibition, Houston, Texas, 26-29 September, 2004.

16. Mezghani, M., Fornel, A., Langlais, V. and Lucet, N.: "History Matching and Quantitative Use of 4D Seismic Data for an Improved Reservoir Characterization," paper SPE 90420, presented at the 2004 SPE Annual Technical Conference and Exhibition, Houston, Texas, 26-29 September, 2004.

17. Dong, Y. and Oliver, D.: "Quantitative Use of 4D Seismic Data for Reservoir Description," paper SPE 84571, presented at the 2003 SPE Annual Technical Conference and Exhibition, Denver, Colorado, 5-8 October, 2003.

18. Haverl, M., Aga, M. and Reiso, E.: "Integrated Workflow for Quantitative Use of Time-Lapse Seismic Data in History Matching: A North Sea Field Case," paper SPE 94453, presented at the 2005 SPE Europec/EAGE Annual Technical Conference, Madrid, Spain, 13-16 June, 2005.

19. Kjelstadli, R., Lane, H., Johnson, D., Barkved, O. and Buer, K.: "Quantitative History Match of 4D Seismic Response and Production Data in the Valhall Field," paper SPE 96317, presented at the 2005 SPE Offshore Europe, Aberdeen, Scotland, 6-9 September, 2005.

20. Khazanehdari, J. and Curtis, T.: "Combined Seismic and Production History Matching," paper SPE 97100, presented at the 2005 SPE Annual Technical Conference and Exhibition, Dallas, Texas, 9-12 October, 2005.

21. Stephen, K. and MacBeth, C.: "Reducing Reservoir Prediction Incertainty Using Seismic History Matching," paper SPE 100295, presented at the 2006 SPE Europec/EAGE Annual Conference, Vienna, Austria, 12-15 June, 2006.

22. Vasco, D.W., Yoon, S., and Datta-Gupta, A.: "Integrating Dynamic Data into High-Resolution Reservoir Models Using Streamline-Based Analytic Sensitivity

Coefficients," *SPE Journal* (December 1999) 389.

23. Kulkarni, K. N., Datta-Gupta, A. and Vasco, D. W., "A Streamline Approach to Integrating Transient Pressure Data into High Resolution Reservoir Models," *SPE Journal* (September 2001), **6**(3), pp 273-282.

24. Datta-Gupta, A., Yoon, S.S., Nordaas, K., and Vasco, D.W.: "Streamlines, Ray Tracing and Production Tomography: Generalization to Compressible Flow," *Petroleum Geoscience* (May 2001), 75.

25. Milliken, W.J. and Emanuel, A.: "History Matching Finite Difference Models with 3D Streamlines," paper SPE 49000 presented at the 1998 SPE Annual Technical Conference and Exhibition, New Orleans, 27-30 September.

26. Milliken, W.J., Emanuel, A. and Chakravarty, A.: "Application of 3D Streamline Simulation to Assist History Matching," paper SPE 63155 presented at the 2000 SPE Annual Technical Conference and Exhibition, Dallas, 1-4 October.

27. Baker R.O: "Streamline Technology: Reservoir History Matching and Forecasting: Its Success, Limitations, and Future," Distinguished Author Series, *Journal of Canadian Petroleum Technology* (April 2001) **40**, No. 4, 23-27.

28. Wen, X.-H., Deutsch, C.V. and Cullick, A.S.: "Inversion of Dynamic Production Data for Permeability: Fast Streamline-Based Computation of Sensitivity Coefficients of Fractional Flow Rate," *J. of Hydrology* (2003) **281**, 296-312.

29. Wang, Y. and Kovscek, A.R.: "Streamline Approach for History Matching Production Data," *SPE Journal* (December 2001) 353-363.

30. Agarwal, A. and Blunt, M.J.: "Streamline-Based Method with Full-Physics Forward Simulation for History-Matching Performance Data of a North Sea Field," *SPE Journal* (June 2003) 171-180.

31. Yoon, S., Malallah, A.H., Datta-Gupta, A. and Vasco, D.W..: "A Multiscale Approach to Production Data Integration Using Streamline Models," *SPE Journal* (June 2001) 182-192.

32. Wu, Z. and Datta-Gupta, A.: "Rapid History Matching Using a Generalized Travel Time Inversion Method," *SPE Journal* (June 2002) 113-122.

33. He, Z., Datta-Gupta, A., and Yoon, S.: "Streamline-Based Production Data Integration with Gravity and Changing Field Conditions," *SPE Journal* (December 2002) 423-436.

34. Cheng, H., Datta-Gupta, A., and He, Z.: "A Comparison of Travel-Time and Amplitude Matching for Production Data Integration into Field-Scale Geologic Model," *SPE Journal* (March 2005) 75-90.

35. Cheng, H., Kharghoria, A. and Datta-Gupta, A.: "Fast History Matching of Finite-Difference Models Using Streamline-Derived Sensitivities," *SPERE* (October 2001), 426.

36. Hohl, D., Jimenez, E. and Datta-Gupta, A.: "Field Experiences with History Matching an Offshore Turbiditic Reservoir Using Inverse Modeling," paper SPE 101983 presented at the SPE Annual Technical Conference and Exhibition, San Antonio, Texas, September 24-27, 2006.

37. Iliassov, P.A., Datta-Gupta, A., and Vasco, D.W.: "Field-Scale Characterization of Permeability and Saturation Distribution Using Partitioning Tracer Tests: The Ranger Field, Texas," *SPE Journal* (December 2002) 409-423.

38. Datta-Gupta A. and King M.J., *Streamline Simulation: Theory and Practice*, SPE Textbook Series, Vol. 11, Texas (2007).

39. Datta-Gupta A. and King M.J.: "A Semianalytic Approach to Tracer Flow Modeling in Heterogeneous Permeable Media," *Adv. in Water Resources* (1995), **18,** No. 1, 9.

40. Datta-Gupta, A., "Streamline Simulation: A Technology Update," SPE Distinguished Author Series, *Journal of Petroleum Technology* (December 2000) 68-73.

41. King, M. J. and A. Datta-Gupta, "Streamline Simulation: A Current Perspective," *In Situ* (1998), **22,** No. 1, 91.

42. Bratvedt, F., Gimse, T. and Tegnander, C., "Streamline Computations for Porous Media Flow Including Gravity," *Transport in Porous Media* (1996), **25**, 63.

43. Bratvedt, F., Bratvedt, K., Buchholz, C. F., Holden, L., Holden, H. and Risebro, N. H., "A New Front Tracking Method for Reservoir Simulation," *SPE Reser. Eng*. (1992), **7**, 107.

44. Bratvedt, F., Bratvedt, K., Buchholz, C. F., Gimse, T., Holden, H., Holden, L. and Risebro, N. H., "FRONTLINE and FRONTSIM. Two Full Scale, Two-Phase, Black Oil Reservoir Simulators Based on Front Tracking," *Surv. Math. Ind*. (1993), **3**, 185.

45. Pollock, D.W.: "Semi-analytical Computation of Path Lines for Finite Difference Models," *Ground Water* (November/December 1988) **26**, No. 6, 743.

46. Cordes, C. and Kinzelbach, W.: "Continuous Groundwater Velocity Fields and Path Lines in Linear, Bilinear and Trilinear Finite Elements," *Water Resour. Res.* (1992) **28**, 2903.

47. Alhuthali, A.H., Datta-Gupta, A., Yuen B., and Fontanilla, J.P: "Optimal Rate Control Under Geologic Uncertainty," paper SPE 113628 presented at the 2008 Improved Oil Recovery Symposium, Tulsa, OK, April 2008.

48. Prévost, M., Edwards, M.G., and Blunt, M.J: "Streamline Tracing on Curvilinear Structured and Ustructured Grids," paper SPE 66347 presented at SPE Reservoir Simulation Symposium, Houston, TX, February 2001.

49. Sabir, K.: "Velocity Models, Material Balance and Solution Convergence in Streamline-Based Simulation," M.S. Thesis, Texas A&M University, College Station, TX (December 200)

50. Jimenez, E.: "The Impact of Grid Geometry on Displacement Calculations," M.S. Thesis, Texas A&M University, College Station, TX (August 2004)

51. Jimenez, E., Sabir, K., Datta-Gupta, A. and King, M.: "Spatial Error and Convergence in Streamline Simulation," *SPE Reser. Eng.* (2007), **6**, 221.

52. Bear, J., *Dynamics of Fluids in Porous Media*, American Elsevier, New York (1972).

53. Aziz, K. and Settari, A., *Petroleum Reservoir Simulation*, Applied Science Publishers, Essex, England (1979).

54. Ponting, D.K., "Corner Point Geometry in Reservoir Simulation," Proc. 1st European Conference on the Mathematics of Oil Recovery, Cambridge, United Kingdom, 1989.

55. Press, W.H., Flannery, B.P., Teukolsky, S.A. and Wetterling, W.T.: *Numerical Recipes – The Art of Scientific Computing*, Cambridge University Press, Cambridge (1987).

56. Powell, M.J.D.: "A Fortran Subroutine for Solving System of Nonlinear Algebraic Equations," *Numerical Methods for Nonlinear Algebraic Equations*, Rabinowitz, P. Editor, Gordon and Breach Science Publishers, London (1970).

57. Deutsch, C.V. and Journel, A.G.: *GSLIB: Geostatistical Software Library and User's Guide*. 2nd edition, Oxford University Press, New York (1998).

58. Paige, C.C. and Saunders, M. A.: "LSQR: An Algorithm for Sparse Linear Equations and Sparse Least Squares," ACM Trans. Math. Software (1982) 8, No. 1, 43.

APPENDIX A

ALTERNATIVE TIME-LAPSE SEISMIC SENSITIVITIES

Sensitivities to Time-lapse Difference Dataset. Another typical and more general 4D Seismic processing product is a time-lapse difference dataset (i.e., the seismic data from Survey 1 is subtracted from the data from Survey 2). **Fig. A.1** shows simulated and seismic saturations for two different survey times for the same synthetic 9-spot model used in the single time-lapse seismic approach. The misfit function could be defined as the difference between the time-lapse difference dataset and its equivalent simulation difference dataset; this misfit function will be in closer agreement to the characteristic time-lapse seismic deliverable.

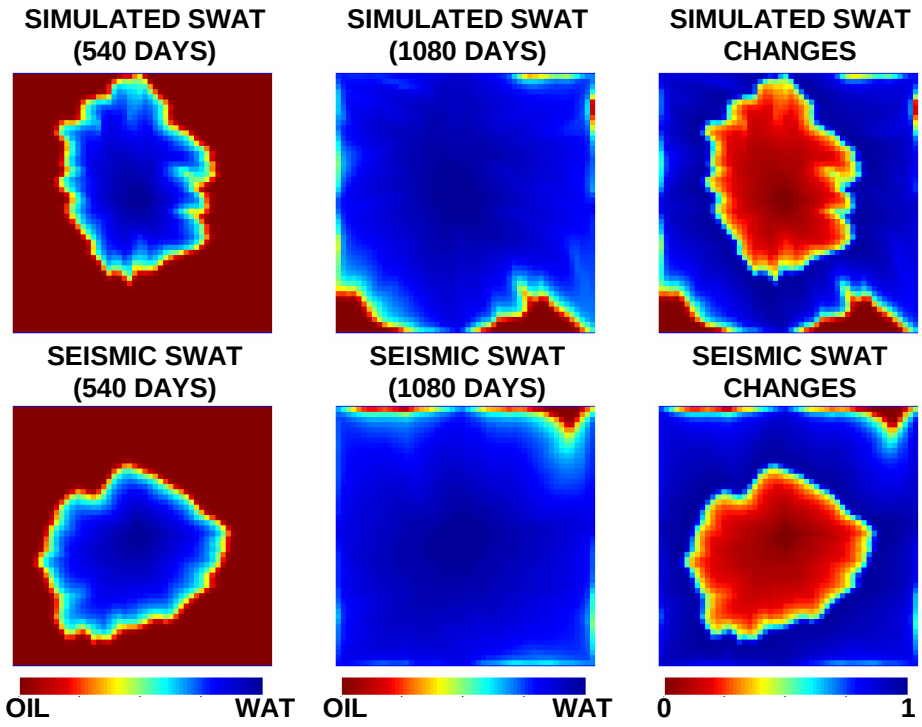

Fig. A.1– Simulated and observed water saturation maps at different seismic acquisition times. Right pictures show saturation changes for both simulated and observed data.

Similar to what we did previously with the saturation differences, the number of observed points to be integrated can be reduced by removing small saturation differences after applying cut-off values. **Fig. A.2** shows several misfit attributes with different cut-off values that eventually will reduce the size of the sensitivity system. Note that in this misfit definition we're including additional information from supplementary seismic surveys. This will reduce the number of inversion iterations to fully integrate all seismic data.

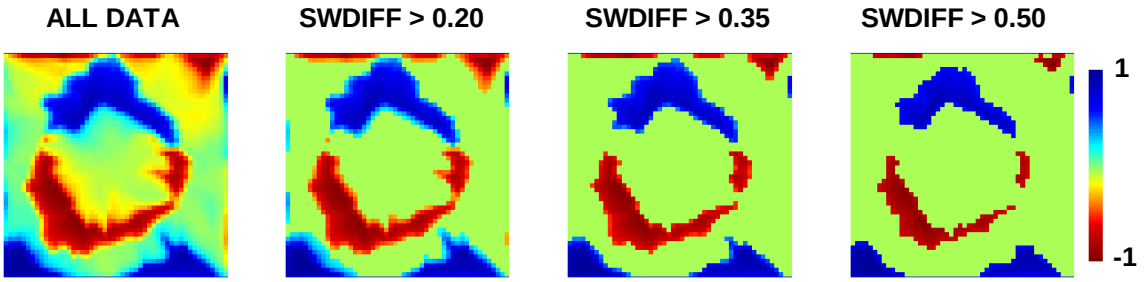

Fig. A.2– Difference between seismic and simulated saturation changes for several cut-offs.

Again, our objective is to obtain a linear expression to form the basis for an iterative inversion that relates perturbations in reservoir properties to perturbations in time-lapse seismic responses. The changes in the seismic responses in our reservoir model can be considered as function of the saturation, pressure, and porosity in each cell[30]. For any cell of the reservoir model let us write the seismic response as $S_S\left(S_w\left(\frac{\tau}{t}\right),P,\phi\right)$. For time-lapse seismic data, we need to consider the state of the reservoir at two distinct times t_0 and t_1. In our derivation we neglect pressure changes and only concentrate in saturation and porosity changes. In this order of ideas when forming the difference $S_S\left(S_w\left(\frac{\tau}{t}\right),P,\phi\right)^1 - S_S\left(S_w\left(\frac{\tau}{t}\right),P,\phi\right)^0$ the porosity difference will vanish for reservoirs with negligible compaction and the pressure difference won't be considered. Thus, any the time-lapse seismic perturbation can be directly related to saturation perturbations as,

$$\begin{aligned}\partial\Delta S_s &= \partial S_S\left(S_w\left(\tfrac{\tau}{t}\right),P,\phi\right)^1 - \partial S_S\left(S_w\left(\tfrac{\tau}{t}\right),P,\phi\right)^0 \\ \partial\Delta S_s &\approx \partial S_w\left(\tfrac{\tau}{t}\right)^1 - \partial S_w\left(\tfrac{\tau}{t}\right)^0\end{aligned} \tag{A.1}$$

We're now in position to define the sensitivity of the time-lapse seismic perturbation with respect to reservoir parameters *m* as follows,

$$\frac{\partial\Delta S_s}{\partial m} = \left.\frac{\partial S_w\left(\tfrac{\tau}{t}\right)}{\partial m}\right|^1 - \left.\frac{\partial S_w\left(\tfrac{\tau}{t}\right)}{\partial m}\right|^0 \tag{A.2}$$

This expression will again reduce to the sensitivity estimation of the water saturation at each cell, $\partial S_w\left(\tfrac{\tau}{t}\right)/\partial m$. This sensitivity was previously derived considering the semi-analytic solution for the saturation history and the time of flight sensitivity (**Eq. 4.10**),

$$\frac{\partial\Delta S_s}{\partial m} = \left.\frac{1}{t_1}\frac{\partial S_{wi,j}\left(\tfrac{\tau}{t}\right)}{\partial\tau}\cdot\frac{\partial\tau}{\partial m}\right|^1 - \left.\frac{1}{t_0}\frac{\partial S_{wi,j}\left(\tfrac{\tau}{t}\right)}{\partial\tau}\cdot\frac{\partial\tau}{\partial m}\right|^0 \tag{A.3}$$

Again the sensitivities are trajectory-based, computed as line integrals over the paths ψ^1 and ψ^0. Note that when there is no significant variation in reservoir pressure during the time interval between the seismic surveys, the trajectories will be virtually identical. Even under significant pressure changes this would be an appropriate approximation considering that we're attempting to integrate dynamic data rather than predicting fluid flow performance.

Sensitivities to Connective Function. The starting point is defining the misfit between simulated and seismically derived saturation in terms of the following correlation function as suggested by Luo and Schuster[13]

$$f(\tau,\Delta\tau)=\int d\tau\,\frac{S_w(\tau+\Delta\tau)_o}{A_o}S_w(\tau)_c \tag{A.4}$$

Where $\boldsymbol{A}$ is the maximum amplitude of water saturation and $\boldsymbol{\Delta\tau}$ is the shift time between simulated and seismically derived saturation defined along the trajectory of each streamline. We're doing the shift in space rather than time as we're using the time of flight as a spatial coordinate. We seek a $\boldsymbol{\Delta\tau}$ that shifts the simulated water saturation so that it best matches the seismically derived water saturation. Since the saturation profile is expected to be highly non-monotonic, this will in a way match the saturation fronts in an average sense.

The criterion for the "best" match is defined as the residual $\boldsymbol{\Delta\tau}$ that maximizes the previous correlation function, that is,

$$f(\tau,\Delta\tau)=\max\left\{f(\tau,\Delta\tau)\middle|\tau\in[-T,T]\right\} \tag{A.5}$$

Where $\boldsymbol{T}$ is the estimated maximum $\boldsymbol{\Delta\tau}$ difference between the simulated and seismically derived water front. Therefore, the derivative (Leibniz Integral Rule) of $f(\tau,\Delta\tau)$ with respect to $\boldsymbol{\tau}$ should be zero at $\boldsymbol{\Delta\tau}$ unless the maximum is at an endpoint $\boldsymbol{T}$ or $\boldsymbol{-T}$

$$\begin{aligned}\dot{f}_{\Delta\tau}&=\left[\frac{\partial f(\tau,\Delta\tau)}{\partial\tau}\right]_{\tau=\Delta\tau}\\&=\frac{1}{A}\int d\tau\,\frac{\partial S_w(\tau+\Delta\tau)_o}{\partial\tau}S_w(\tau)_c=0\end{aligned} \tag{A.6}$$

Using **Eq. A.6** and the rule for the derivative of an implicit function, we get

$$\frac{\partial \Delta\tau}{\partial k(x)} = -\frac{\dfrac{\partial\left(\dot{f}_{\Delta\tau}\right)}{\partial k(x)}}{\dfrac{\partial\left(\dot{f}_{\Delta\tau}\right)}{\partial \Delta\tau}} \tag{A.7}$$

Taking the derivatives of $\dot{f}_{\Delta\tau}$ with respect to $k(x)$ and $\Delta\tau$ we have

$$\begin{aligned}\frac{\partial\left(\dot{f}_{\Delta\tau}\right)}{\partial k(x)} &= \frac{1}{A}\int d\tau \frac{\partial S_w(\tau+\Delta\tau)_o}{\partial \tau}\frac{\partial S_w(\tau)_c}{\partial k(x)} \\ &= \frac{1}{A}\int d\tau \frac{\partial S_w(\tau+\Delta\tau)_o}{\partial \tau}\frac{\partial S_w(\tau)_c}{\partial \tau}\frac{\partial \tau}{\partial k(x)}\end{aligned} \tag{A.8}$$

And

$$\frac{\partial\left(\dot{f}_{\Delta\tau}\right)}{\partial \Delta\tau} = \frac{\int d\tau \cdot E}{A} \tag{A.9}$$

Where

$$\begin{aligned}E &= \frac{\partial S_w(\tau+\Delta\tau)_o}{\partial \tau}\frac{\partial S_w(\tau)_c}{\partial \Delta\tau}\frac{\partial \Delta\tau}{\partial \tau} + S_w(\tau)_c \frac{\partial\left[\dfrac{\partial S_w(\tau+\Delta\tau)_o}{\partial \tau}\right]}{\partial \Delta\tau}\frac{\partial \Delta\tau}{\partial \tau} \\ &= \frac{\partial S_w(\tau+\Delta\tau)_o}{\partial \tau}\frac{\partial S_w(\tau)_c}{\partial \tau} + S_w(\tau)_c \frac{\partial^2 S_w(\tau+\Delta\tau)_o}{\partial \tau^2}\end{aligned} \tag{A.10}$$

Note that in the previous equation we have set $\frac{\partial \Delta\tau}{\partial \tau} = 1$. If we now substitute **Eqs. A.8** through **A.10** into **Eq. A.7** the following expression will be obtained,

$$\frac{\partial \Delta\tau}{\partial k(x)} = -\frac{\int d\tau \frac{\partial S_w(\tau+\Delta\tau)_o}{\partial \tau} \frac{\partial S_w(\tau)_c}{\partial \tau} \frac{\partial \tau}{\partial k(x)}}{\int d\tau \cdot \left[\frac{\partial S_w(\tau+\Delta\tau)_o}{\partial \tau} \frac{\partial S_w(\tau)_c}{\partial \tau} + S_w(\tau)_c \frac{\partial^2 S_w(\tau+\Delta\tau)_o}{\partial \tau^2} \right]} \quad \text{(A.11)}$$

This will be the sensitivity of the travel time misfit between seismic and simulated saturation with respect to permeability. About the terms in **Eq. A.11**

$\frac{\partial S_w(\tau+\Delta\tau)_o}{\partial \tau}$ Calculated numerically from seismically derived saturations.

$\frac{\partial S_w(\tau)_c}{\partial \tau}$ Calculated numerically from numerical saturations.

$\frac{\partial \tau}{\partial k(x)}$ Sensitivities of time of flight already available from production integration.

$S_w(\tau)_c$ Obtained from simulator at each streamline segment

$\frac{\partial^2 S_w(\tau+\Delta\tau)_o}{\partial \tau^2}$ Obtained numerically from seismically derived saturations

VITA

Eduardo Antonio Jimenez Arismendi
Petroleum Eng. Dept.
3116 TAMU
College Station, TX USA, 77843
Ph: (979)676-3574
jimaris@yahoo.com

PROFILE

Petroleum engineer with seven years of experience in integrated reservoir modeling. Currently, involved in research concerning stochastic reservoir characterization and streamline simulation. Special interest in the development and application of high-resolution numerical schemes for reservoir simulation, gridding techniques, dynamic data integration, software design and development.

EDUCATION

Doctor of Philosophy. Petroleum Engineering. Texas A&M University. May 2008

Master of Science. Petroleum Engineering. Texas A&M University. August 2004

Bachelor of Science. Petroleum Engineering. Universidad Industrial de Santander. March 2000

EXPERIENCE

Texas A&M University. Research Assistant. 2002-2007

American Geoexploration-Colombia. Reservoir Engineer. 2000-2002